Calibration, Alignment and Long-Term Performance of the CMS Silicon Tracking Detector

Dissertation

zur Erlangung des Doktorgrades

des Department Physik

der Universität Hamburg

vorgelegt von

Erik Butz

aus Göttingen

Hamburg

2009

Gutachter der Dissertation:	Prof. Dr. Peter Schleper Prof. Dr. Joachim Mnich
Gutachter der Disputation:	Prof. Dr. Robert Klanner JProf. Dr. Johannes Haller
Datum der Disputation:	24. Februar 2009
Vorsitzender des Prüfungsausschusses:	Prof. Dr. Dieter Horns
Vorsitzender des Promotionsausschusses:	Prof. Dr. Robert Klanner
Dekan der MIN-Fakultät:	Prof. Dr. Heinrich Graener

Kurzfassung

Mit einer Gesamt-Siliziumfläche von mehr als 200 m^2 ist der Silizium-Spurdetektor des CMS-Experiments am LHC Beschleuniger der größte Spurdetektor dieser Art, der je gebaut wurde. Die mehr als 15000 Einzelmodule müssen sehr hohen Anforderungen in Hinblick auf ihr Rauschverhalten, das elektronische Übersprechen, sowie die genaue Kenntnis ihrer Position innerhalb des Spurdetektors erfüllen. Über die vorraussichtliche Betriebszeit werden die Module außerdem hohen Strahlungsdosen ausgesetzt sein, welche diverse Eigenschaften der Module verändern werden. Diverse der oben genannten Aspekte sind Gegestand dieser Arbeit.

Zunächst werden Ergebnisse von Teststrahl-Messungen an Einzel-Modulen des Spurdetektors gezeigt. Die Module wurden unterschiedlichen Strahlungsdosen ausgesetzt, bis hin zur zu erwartenden Gesamtdosis während der Betriebsdauer des Spurdetektors für diese Module. An diesen bestrahlten Modulen wird das Langzeit-Verhalten der Module untersucht. Es wird das Signal-zu-Rausch-Verhältnis, das elektronische Übersprechen und das Ladungssammel-Verhalten untersucht. Das Signal-zu-Rausch-Verhältnis liegt oberhalb der Spezifikationen und zeigt das erwartete Verhalten bei Variation der Betriebsparameter. Das Übersprechen ändert sich kaum mit zunehmender Bestrahlung. Die Ortsauflösung wird untersucht als Funktion der Strahlenergie, des Einschusswinkels und der Position auf dem Sensor. Der Einfluss der Bestrahlung auf die Ortsauflösung ist gering. Desweiteren werden verschiedene Cluster-Algorithmen untersucht und die bestmögliche Ortsauflösung unter verschiedenen Bedingungen ermittelt. Eine Verbesserung der Ortsauflösung im Vergleich zur Standardrekonstruktion kann, unabhängig von der Bestrahlung, erreicht werden.

Im nächsten Schritt wird das Verhalten von größeren Strukturen anhand zweier Sektoren der Endkappen des Spurdetektors im sogenannten „Tracker Slice-Test“ untersucht, bei dem etwa 12.5% des gesamten Spurdetektors ausgelesen wurden. Hierbei liegt der Schwerpunkt auf der Inbetriebnahme und der Untersuchung der zugehörigen Betriebsparameter. Besondere Beachtung gilt dem Rauschverhalten des Systems. Es wird untersucht als Funktion der Temperatur und verschiedener Stromversorgungskonfigurationen. Das Rauschverhalten erweist sich als stabil und zeigt das zu erwartende Verhalten. Die Änderung bei verschiedenen Stromversorgungskonfigurationen liegen im Bereich von 2%. Defekte verschiedener Natur werden gezeigt, identifiziert und überwacht. Der Anteil persistenter Defekte an der Anzahl der Kanäle in den Endkappen-Sektoren liegt bei ca. 0.7%.

Schließlich wird für den gesamten Spurdetektor die präzise Ausrichtung (Alignierung) der mehr als 15000 Module des Trackers betrachtet. Eine präzise Ausrichtung der Module ist Vorraussetzung für die Auflösung verschiedener primärer und sekundärer Vertizes sowie der genauen Impulsmessung. In dieser Arbeit liegt der Fokus auf der Beurteilung der Qualität eines Alignierungsvorgangs. Anhand von Daten kosmischer Myonen werden mögliche sensitive Variablen motiviert und getestet. Hieran wird das Funktionsprinzip des Validierungsprozesses überprüft.

Abstract

With an active area of more than 200 m^2, the CMS silicon strip detector is the largest silicon tracker ever built. It consists of more than 15,000 individual silicon modules which have to meet very high standards in terms of noise behavior and electronic crosstalk, as well as their exact positioning within the tracker. Furthermore, the modules will be exposed to a harsh radiation environment over the lifetime of the tracker. This thesis deals with several of the above-mentioned aspects.

In the first part, individual modules are investigated using a testbeam. Some of the modules were irradiated up to an integrated dose which corresponds to the expected one over the life time of the tracker. These modules are investigated with respect to their signal-to-noise behavior, and their cross-talk. Several operational parameters are varied, such as the temperature and the bias voltage. It is shown that the modules behave as expected. The signal-to-noise ratio is well above the specifications and the cross-talk increases only very moderately with irradiation. Furthermore, the spatial resolution of the modules is investigated. Different cluster algorithms are utilized and compared. It is shown that the spatial resolution is not much affected by irradiation and that the spatial resolution can be improved with respect to the current standard reconstruction.

In the second part, larger structures of the silicon tracker are studied during the so-called "tracker slice-test". Two sectors from one of the tracker end caps are investigated. Special emphasis is given to the commissioning of the system and the monitoring of the various commissioning parameters. Furthermore, the noise of the system is investigated as a function of the ambient temperature and different powering schemes. It is shown that the noise of the system behaves as expected. The noise is stable within 2% for different powering schemes. Also possible failures of components are investigated and persistent defects are identified and monitored. The total amount of localized and non-localized defects is found to be about 0.7% for the two end cap sectors.

Lastly, the alignment of the detector is a subject of interest, as the exact alignment of all components of the tracker with respect to each other will be of prime importance for any analysis using the tracker. The separation of primary and secondary vertices as well as the momentum resolution depend largely on a very good alignment of the detector. In this thesis, the validation of an alignment result is investigated. Several quantities which could be used to judge the quality of an alignment are discussed. A first application of the validation is shown on cosmic muon data, taken with the whole silicon tracker after the integration into the experiment.

Contents

Introduction

There is a theory which states that if ever anyone discovers exactly what the Universe is for and why it is here, it will instantly disappear and be replaced by something even more bizarre and inexplicable.

There is another theory which states that this has already happened.
Douglas Adams, *The Restaurant at the End of the Universe*

Challenges in Particle Physics

With the operation of the Large Hadron Collider (LHC) close to Geneva, the quest for fundamental answers to open question of modern particle physics enters a new era. Being the first collider to reach deep into the tera-electronvolt energy scale, it is widely believed that the LHC will be able to provide answers to several of the open questions which have puzzled physicists for several decades:

- What is the origin of (particle) mass?
- What is the nature of dark matter?
- Are there more than three spatial dimensions?
- Can the forces of nature be unified conceptually into a single force?

These and other questions were the motivations to build the LHC.

The Standard Model of Particle Physics

The standard model of particle physics [1–7] is a framework of gauge theories which describe the fundamental particles and their interactions. The standard model is based on the gauge group $SU(3)_{\text{color}} \times SU(2)_L \times U(1)_Y$ of the strong and the electroweak interaction. The particles of the standard model are divided into fermions and bosons, depending on their spin. The fundamental fermions are divided into quarks and leptons and they come in three so-called families or generations. The first generation with the electron and the electron-neutrino in the lepton, and the up- and down-quark in the quark sector, makes up the ordinary matter in the universe. The interactions between the leptons and quarks are mediated by fundamental bosons which are associated with the different interactions. The most well-known gauge-boson is the photon which mediates the electromagnetic interaction.

The standard model is very successful in describing a large amount of precision data [8]. The only missing element of the standard model is the Higgs boson which so far has escaped detection [9, 10]. The Higgs mechanism or Higgs-Brout-Englert-Guralnik-Hagen-Kibble

mechanism [11–13] within the standard model is mediated by a single scalar doublet field which generates the masses of the intermediate gauge bosons and the fermions. Even though it has been remarkably successful, it is widely believed that the Standard Model is only an effective low-energy theory and that an extension will be needed beyond energies of about 1 TeV. There are several problems within the Standard Model which guide the way to new physics. The Standard Model does not incorporate gravity and thus is not a theory which describes all forces of nature. Cosmological data [14, 15] hint at the existence of some unknown form of dark matter. This contribution could be explained by the existence of a heavy neutral stable particle which interacts only by gravity or some other very weak interaction with ordinary matter. No candidate of such a particle can be found in the Standard Model. The group structure of the Standard model is $SU(3) \times SU(2) \times U(1)$. Yet there is no evidence for a Grand Unified Theory (GUT) which provides a unification of the three groups in some larger group like $SU(5)$ or $SU(10)$ which would lead to a unification of all couplings to a single coupling at some scale (Λ_{GUT}).

Another problem in the Standard Model is that there are large loop corrections to the Higgs boson mass which are quadratically divergent and ultimately would have to be cancelled by contributions from physics at the Planck scale. Under normal circumstances this would lead to a Higgs boson mass which would be close to the GUT-scale at $\mathcal{O}(10^{16}$ GeV). To get a Higgs boson mass which is close to the electroweak scale at about 10^2 GeV an enormous degree of fine-tuning $\mathcal{O}(10^{-30})$ of the Standard Model parameters is necessary. This is known as the *fine-tuning* problem of the Standard Model. Furthermore it is not known why the GUT-scale and the electroweak scale are separated by more than ten orders of magnitude. This is known as the *hierarchy problem*.

Another problem of the Standard Model — though this problem is also common to several of its extension — is the lack of any explanation for the nature of dark energy (see e.g. [16]), which constitutes up to 75% of the energy content in the universe.

Extensions to the Standard Model

Several extensions to the standard model have been suggested over the years, which deal with the above problems.

Supersymmetry

Supersymmetry [17] is considered by many physicists as the most promising extension of the standard model. It postulates a relation between fermions and bosons and predicts the existence of a supersymmetric partner to each standard model particle (so-called *sparticles*). This partner has the same quantum numbers apart from the spin, which differs by half a unit. The loop contributions of the partner-particles are such that they cancel the contributions of their standard model partners which lead to a divergence of the Higgs boson mass, thereby providing a solution to the fine-tuning problem. At the same time this mechanism could provide a solution to the hierarchy problem by bringing the Higgs-boson mass and hence the scale of the electroweak symmetry breaking to the known low scale.

In most supersymmetric models a new conserved quantum number is postulated, the so-called *R-parity*. This provides baryon and lepton number conservation and is defined such that all standard model particles have R-parity $+1$, whereas all supersymmetric partners have R-parity -1. If this is indeed the case, the lightest supersymmetric particle is stable

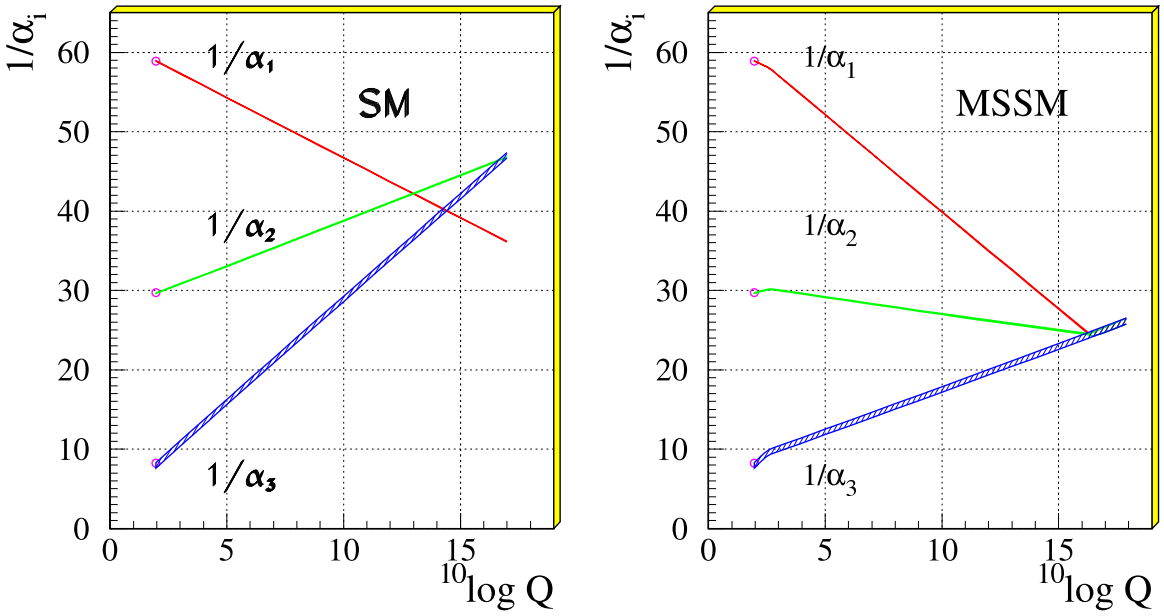

Figure : Running of couplings in the Standard Model and the MSSM.

and a natural candidate to explain dark matter. Since no supersymmetric particles have been observed up to date, it can be deduced that supersymmetry — should it be realized in nature — has to be spontaneously broken, since the masses of the sparticles have to be much higher than the ones of their partners. Most current supersymmetric models differ in the mechanism by which they introduce the breaking of supersymmetry (e.g. gauge-mediated supersymmetry breaking (GMSB)).

In the Minimally Supersymmetric Extension of the Standard Model (MSSM), no mechanism for the breaking of supersymmetry is specified. This introduces a large number of new parameters [$\mathcal{O}(100)$] which have to be put into the theory "by hand". This number of parameters is largely reduced in models which assume a specific mechanism for the breaking of supersymmetry. In the MSSM, the neutralino[1] χ^0 is a natural candidate for dark matter since it is stable (as the lightest particle in an R-parity conserving model), heavy and electrically neutral. The particle spectrum of the MSSM could provide an alteration of the running of the different coupling constants and could lead to a unification of the coupling at the GUT-scale as it is indicated in the figure above.

Extra Dimensions

Extra dimension as extensions of the standard model postulate the existence of additional spatial dimensions which, since they are not visible in everyday life, must be very small (compactified). These higher dimensions are used as an explanation for the difference between the Planck- and the electroweak scale; gravity is allowed to propagate freely in the

[1] The neutralino is the superpartner of the photon, the Z^0 and the neutral Higgs-bosons. Since the neutralino states have the same quantum numbers, they can mix and form four mass eigenstates χ_i^0 $(i = 1, \ldots, 4)$, the lightest being the particle mentioned above.

complete higher-dimensional space, whereas standard model particles are confined to the normal three space dimensions. Depending on the exact modeling of the extra dimensions (see e.g. [18]), experimental signatures can range from the observation of so-called *Kaluza-Klein towers* of states, *monojets* or *mini black-holes*. Models with extra dimensions are furthermore viewed as a possible connection to string theory which also requires a higher dimensionality of space-time.

Strong Dynamics

In models with strong dynamics, a completely different approach is chosen to solve the problems of the standard model. In most of these models it is assumed that the Higgs-mechanism is not mediated by a fundamental scalar field, but by some unknown strong force which is similar to QCD, which is why the first versions of these theories acquired the name *Technicolor models* [19, 20]. Today, simple QCD-like models are severely challenged by experiment (see e.g. [21]). Furthermore they do not offer a mechanism for the fermion masses. More elaborate models such as Extended Technicolor [22, 23] or Walking Technicolor [24] could still provide an explanation of the dynamics at the TeV-scale. Extended Technicolor also aims at a dynamical explanation of flavor, which is not given in most of the other extensions of the standard model. The role of the Higgs boson in Technicolor models is taken by so-called *technipions* which act as Goldstone bosons for the breaking of the electroweak symmetry. Experimentally these models could exhibit themselves by resonantly produced states e.g. in WW scattering.

Challenges for Inner Tracking Detectors at the LHC

The LHC is a proton-proton collider which was built at CERN in the tunnel formerly occupied by the Large Electron-Positron Collider (LEP). It has a circumference of 27 km and is designed to reach a center-of-mass energy of 14 TeV. In fall 2008, the first protons were circulated around the LHC ring and physics data taking is scheduled to start in the summer of 2009. In order to explore the physics beyond the standard model, the LHC is designed to achieve an unprecedented luminosity for a hadron collider of $10^{34}\mathrm{cm}^{-1}\mathrm{s}^{-1}$. At nominal luminosity the LHC ring will be filled with almost 3000 proton bunches in each of the two proton beams. Each bunch will contain more than 10^{11} protons. The bunch spacing will be 25 ns which corresponds to a collision rate of 40 MHz.

Central tracking detectors with high resolution are of vital importance for the physics analyses. The central tracker has to provide a very accurate determination of both primary and secondary vertices. This reduces the problem posed by pile-up events and enhances the sensitivity in many interesting physics channels that rely on the analysis of decays of long-lived heavy particles such as b-quark mesons or τ-leptons is greatly enhanced. Due to the high luminosity of the LHC, the tracking detectors face several challenges.

Occupancy

In each bunch crossing, up to 20 inelastic interactions can occur in addition to the hard scattering. It can be estimated that this may lead to a charged track multiplicity of up to 1000 charged tracks per bunch crossing. This is illustrated in the figure below, which shows

the decay of a Higgs boson to two electrons and two muons at luminosities of $10^{32}\text{cm}^{-1}\text{s}^{-1}$ and $10^{34}\text{cm}^{-1}\text{s}^{-1}$. In order to be able to solve this huge task for pattern recognition, the LHC detectors will have to be sufficiently granular to be able to resolve possible ambiguities. Furthermore, latency in the detector read-out has to be considered, i.e. the detector read out has to be sufficiently fast such that consecutive interactions can be disentangled in the readout chain.

Resolution

At the energies which will be reached at the LHC, measuring the curvature and hence the momentum of a particle created in a collision is a difficult task. Even with the strongest magnetic fields employed in the LHC detectors, the curvature of a particle at an energy of 1 TeV, which is well within the kinematic range, is only of the order of few mm over several meters. Several requirements for the tracking systems have been formulated [25]:

- A dimuon mass resolution of 1% up to energies of 100 GeV.
- The charge of particles should be determined unambiguously up to energies of 1 TeV.
- The material introduced in the inner tracking layers has to be minimized in order to reduce photon conversion, bremsstrahlung and secondary inelastic interactions which deteriorates measurements of other detector parts, especially the electromagnetic calorimeters.

Radiation

In addition to the problem posed for the pattern recognition indicated above, the radiation doses imposed on the detector parts form a major challenge at the LHC. The innermost tracking layers will suffer from integrated radiation doses close to 1 MGy. These macroscopic doses have large impact on the performance and the lifetime of the components. In principal the radiation dose is expected to fall off with the distance the interaction point squared, but effects such as rescattering of particles come into play, posing radiation requirements also on detector parts farther away from the interaction region.

All large experiments at the CERN LHC have adopted silicon technology to cope with the challenges mentioned above.

This thesis deals with several aspects of the operation and long-term performance of the micro-strip tracker of the CMS experiment. As a prelude to the operation, single modules from the tracker were investigated which were irradiated to fluences as expected over the lifetime of the tracking system. For this, testbeam data were taken in an electron testbeam. The performance of the modules was investigated with respect to their signal-to-noise ratio, spatial resolution as well as charge sharing and cross-talk.

As a next step, the performance of larger structures is investigated during the course of the so-called slice or sector test in which 12.5% of the complete tracking system were connected, commissioned and read out. Here, special emphasis is put on the noise performance of the system and to possible defects and their evolution as a function of various operational parameters. Measurements were performed at different ambient temperatures and using different powering schemes.

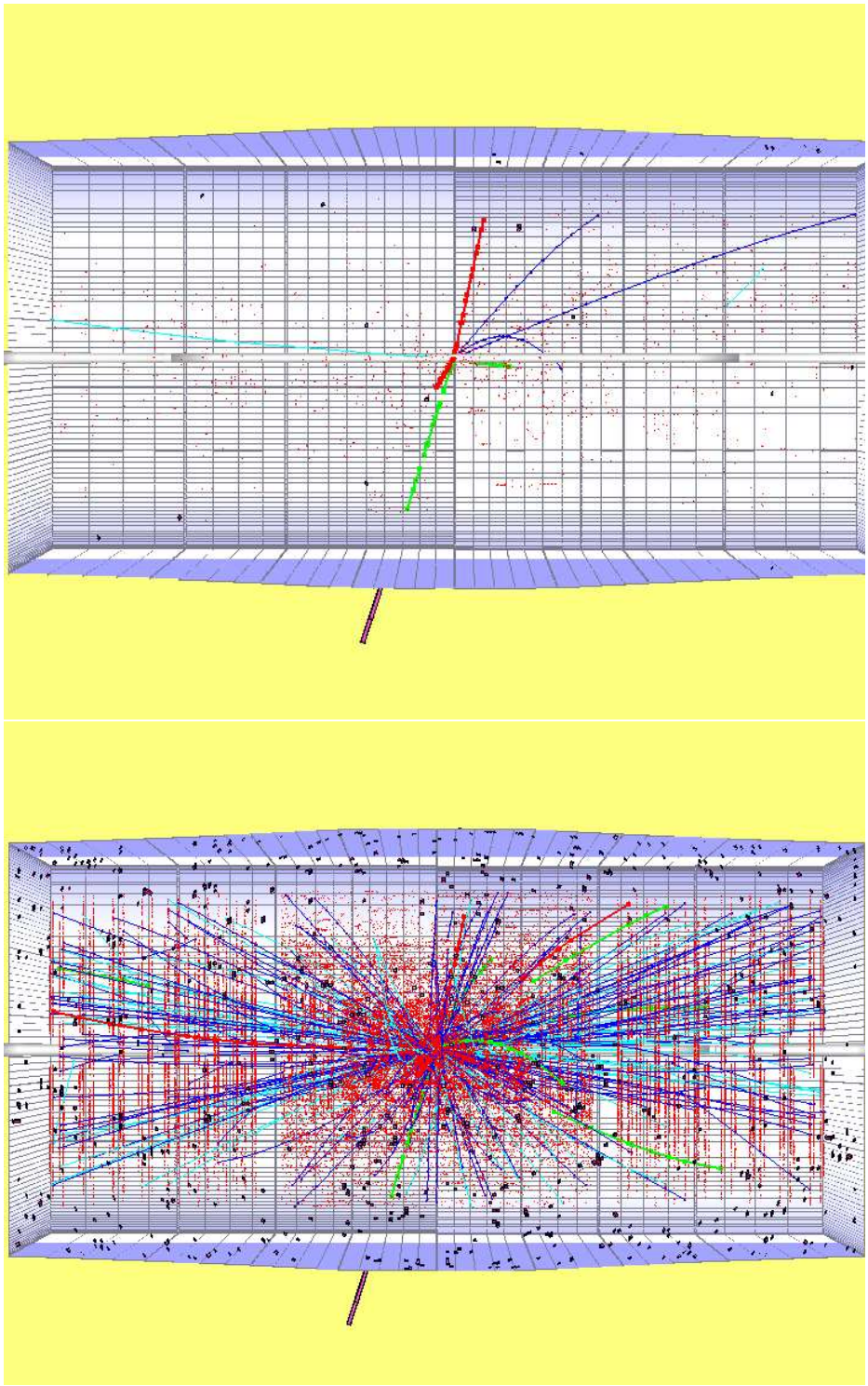

Figure : Simulated Higgs decay into two muons and two electrons at luminosities of $10^{32}\text{cm}^{-1}\text{s}^{-1}$ with no pile-up (top) and $10^{34}\text{cm}^{-1}\text{s}^{-1}$ with 20 pile-up events overlaid (bottom).

Lastly, the alignment of the tracker — which will be of prime importance for the precision of any analysis using tracks — is subject of investigation. Particularly the validation of the alignment process is considered, i.e. the judgement of the quality of an alignment result compared to idealized conditions and other alignment results. The working principle is shown using cosmic muon data taken with fully assembled and commissioned CMS tracking system.

This thesis is structured as follows: An introduction to silicon detectors and radiation damage is given in Chapter 1. The design of the LHC accelerator is outlined in Chapter 2. Chapter 3 is devoted to a description of the CMS detector, with special emphasis on the tracking system since it is central to this thesis. In Chapter 4, the results from the analysis of testbeam data taken with irradiated modules of the CMS silicon strip tracker will be presented. Next, results from the Slice Test will be presented in Chapter 5. Finally, preliminary results from the process of alignment validation will be given in Chapter 6. A summary and outlook will be given in Chapter 7.

1 Theory of Semiconductor Detectors

Semiconductor detectors today are widely used in high energy physics experiments. They are used close to the beam line and provide precise measurements of primary and secondary vertices and robust input for track seeding and reconstruction. With this it is possible to tag individual jets which contain heavy quarks or τ-leptons which are often interesting signatures in searches for new physics.

In this chapter, an overview of the theory of semiconductor detectors is given. First, semiconductors and the principle of *doping* are outlined. Then the advantages of silicon as a detector material are discussed. After this, the effects of radiation on silicon detectors are described and models for the description of these are shown.

1.1 Semiconductors

In solids, the energy levels of the electrons form bands which govern the electrical properties of the material. For semiconductors (as for insulators) there is a region in the distribution of the energy bands where no states are allowed. This region is called *band gap*, the energy levels above are called *conduction band*, those below *valence band*. The occupation probability of levels with a given energy E in the conduction band is governed by the *Fermi-Dirac statistics*:

$$F(E) = \frac{1}{1 + \exp\left[\frac{E - E_F}{k_B T}\right]} \tag{1.1}$$

where E_F is the Fermi energy, k_B is Boltzmann's constant and T is the temperature of the system. At 0 K, the occupation probability is zero in the conduction band and the material becomes a perfect insulator. If the highest point in the valence band is directly below the lowest point in the conduction band, represented in momentum space, the semiconductor has a so-called *direct band gap*. In this case electrons from the conduction band can directly recombine with unoccupied levels in the valence band (so-called *holes*) while conserving momentum. An example of a direct band gap is shown in figure 1.1a. In case of an *indirect band gap*, transitions cannot occur directly from the valence to conduction band, because additional momentum is needed. Momentum conservation is achieved by the excitation of vibrational modes (phonons) in the lattice. This situation is illustrated in figure 1.1b. Due to this separation, more energy is needed for the excitation of an electron than is required by the size of the band gap.

The resistivities of semiconductors vary over several orders of magnitude. They lie between those of conductors and insulators. The resistivity ρ of a material depends on quantities as the temperature and impurities in the material. It can be calculated from the mobility μ_i of charge carriers of type i and their abundance per unit volume n_i as:

$$\rho = \frac{1}{\mu_e n_e + \mu_h n_h} \tag{1.2}$$

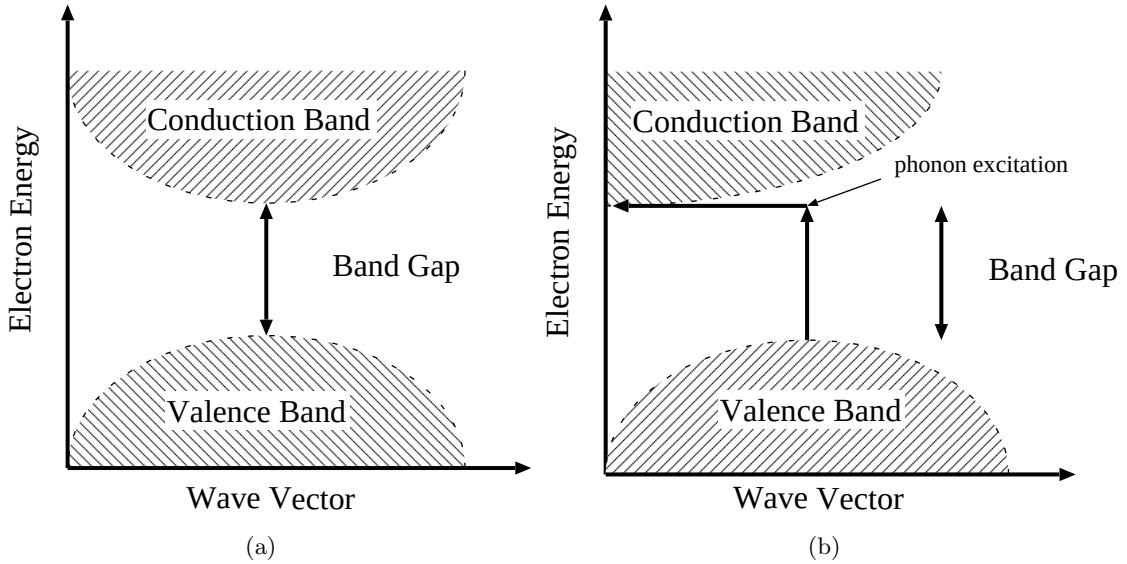

Figure 1.1: Schematic view of a direct (a) and indirect (b) band gap in semiconductors.

Here e stands for electrons in the valence band which move freely in the material, whereas h denotes holes. The latter can also drift in the material and can therefore be viewed as quasi-particles which have charge $+e$. The mobility itself is defined as

$$\mu_i = \frac{v_i}{E} \tag{1.3}$$

where E is the electric field strength and v_i the drift velocity in the material. For intrinsic silicon (see below), the mobilities for electrons and holes are $\mu_e = 1450$ cm^2/Vs and $\mu_h = 450$ cm^2/Vs, respectively. At very high fields, the drift velocity saturates which in term leads to a reduction of the mobility. This is related to a large increase in the probability for the excitation of phonon states, once the charge carriers exceed the energy of these phonon states.

Semiconductors which are not altered by impurities in the material are called *intrinsic semiconductors*. In intrinsic materials with no large impurities, the number of electrons in the conduction band and holes in the valence band is equal and the occupation probability and their density per unit volume is given by

$$n_e = N_c \exp \frac{E_c - E_F}{k_B T} \tag{1.4}$$

$$n_h = N_v \exp \frac{E_F - E_v}{k_B T} \tag{1.5}$$

where N_c and N_v are the densities of states near the edge of the conduction and valence band, respectively, and E_c (E_v) is the lower (upper) energy bound of the conduction (valence) band. From this it follows that

$$n_i^2 = n_e n_h = N_c N_v \exp \frac{E_g}{k_B T}. \tag{1.6}$$

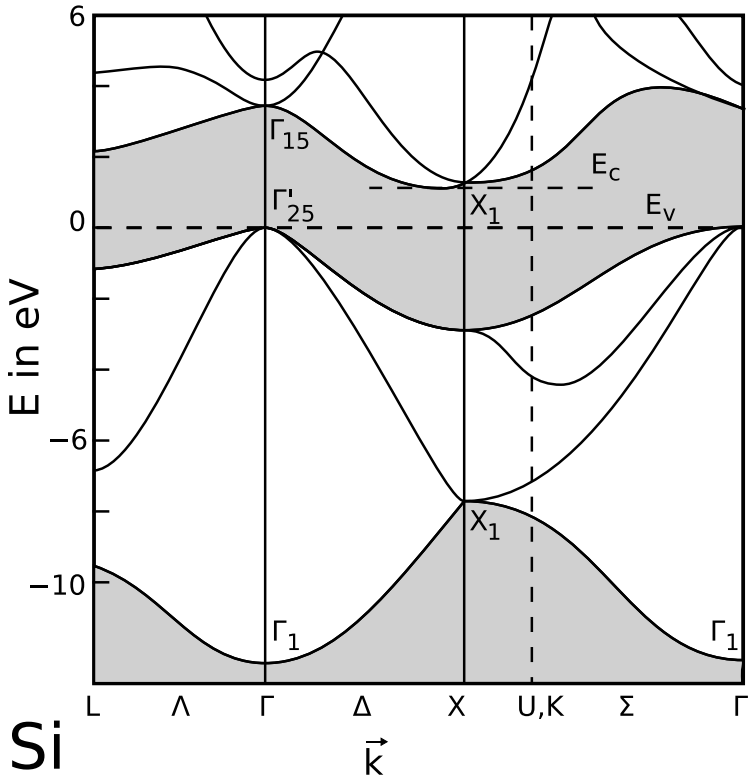

Figure 1.2: Band structure of intrinsic silicon at room temperature. For more details see [27].

where $E_g = E_c - E_v$ is the band gap energy. n_i is referred to as *intrinsic charge carrier density* which depends solely on the size of the band gap and on the temperature of the system. For intrinsic silicon at room temperature it has a value of $1.45 \times 10^{10}\text{cm}^{-3}$.

1.1.1 Advantages of Silicon as Detector Material

Silicon is the most commonly used material for large-scale semiconductor detectors. It has several advantages compared to other semiconductors: It has a relatively small band gap[1] of $E_g = 1.11$ eV and also the energy needed for the creation of an electron-hole pair is comparably small with 3.6 eV. Furthermore, silicon has a high specific energy loss of 390 $\frac{\text{eV}}{\mu\text{m}}$ for a minimum-ionizing particle (MIP), which corresponds to 108 $\frac{\text{e−h pairs}}{\mu\text{m}}$. High signal levels can therefore be achieved at moderate detector thicknesses. The full band structure of silicon is displayed in figure 1.2. It is displayed for the various principal axes $\langle 100 \rangle$, $\langle 110 \rangle$, and $\langle 111 \rangle$, denoted with Δ, Σ and Λ. Forbidden energy zones are marked in grey. The resistivity of intrinsic silicon at room temperature is 235 kΩcm. A huge advantage of silicon as detector material is its wide use in micro-electronic engineering, which leads to a large reduction in cost compared to other detector materials.

[1] This can be compared to 0.66 eV for Ge or 5.47 eV for Diamond.

1.1.2 Doping

In order to alter electric properties such as the resistance of a semiconductor, foreign atoms are introduced into the lattice structure. These create energy levels in the band gap. If these energy levels can readily emit additional electrons in the conduction band, they are called *donors*. If on the other hand they can accept electrons, thereby removing them from the conduction band, they are called *acceptors*. The number of donors (acceptors) is denoted as N_D (N_A). Materials in which the number of acceptors is larger than the number of donors ($N_A > N_D$) are called p-type. In the opposite case, $N_D > N_A$, the material is called n-type. Since the doping of the material is often governed by a combination of additional donors and acceptors, the quantity

$$N_{\text{eff}} = |N_A - N_D| \tag{1.7}$$

which is called *effective doping*, is considered. In case of light to moderate dopant concentrations a semiconductor is called *external*. At very high dopant concentrations one speaks of *degenerate* semiconductors. In this case the resistance is changed so much that the material behaves mostly like a conductor. Degenerate semiconductors are denoted with[2] p^+ or n^+. For silicon and other elements from the forth group of the elements, doping materials which are used are e.g. phosphorus, which is from the fifth group of the elements, for n-doping and boron from the third group for p-doped materials.

In n-type materials, electrons are called *majority charge carriers* because their number exceeds the number of holes and hence there are mainly unpaired electrons which contribute to a charge flow. In this case the holes are called *minority charge carriers*. This situation is reversed in p-type materials.

1.1.3 The *pn* Junction

When a p-type and an n-type material are brought in contact, a so-called pn-junction is created. In an electric circuit the pn-junction behaves as a diode. Due to the difference in the charge carrier concentrations in the two materials, electrons and holes will cross the junction. The zone in which the electrons and holes recombine is void of free charge carriers once the junction reaches its equilibrium state. This zone is called *depletion zone* or *depletion region*; its width is governed by the difference in the dopant concentrations. Due to the drift of majority charge carriers towards the junction, a net charge is left over in the region adjacent to the junction. This leads to the build-up of a difference in potential which is governed by the difference in the effective dopant concentrations in the two regions. This *built-in voltage* or built-in potential can be calculated as:

$$V_{\text{bi}} = \frac{e}{2\varepsilon\varepsilon_0}\left(N_D x_n^2 + N_A x_p^2\right) \tag{1.8}$$

where x_n and x_p are the extensions into the n and p-doped region, respectively, and e is the electron charge. The width of the depletion zone changes if a bias voltage is applied to the electrodes. Two cases can be distinguished:

Forward Bias

If a pn-junction is operated in forward bias, the anode is connected to the p-type material

[2] Conversely at very low dopant concentrations, materials are denoted as p^- and n^-.

while the cathode is connected to the *n*-side. In this situation, the majority charge carriers of both types drift towards the depletion region, thereby decreasing its size. Once the depletion region becomes small enough, majority carriers cross the barrier and recombine with their counterparts. This increases the charge flow towards the junction.

Reverse Bias

In the case of a *reverse bias* the anode is connected to the n region and the cathode to the p region. In this case, majority carriers move away from the depletion zone, thereby increasing its size. This continues until the depletion zone extends across the whole diode. The voltage at which the depletion zone extends over the whole diode is called *full depletion voltage* or simply *depletion voltage*.

1.1.4 Charge Generation and Signal Formation

The mean energy loss by ionization in silicon detectors (and generally in matter) of relativistic particles is governed by the *Bethe-Bloch equation* [21]

$$-\left\langle \frac{dE}{dx} \right\rangle = 4\pi N_A r_e^2 m_e c^2 z^2 \frac{Z}{A}\frac{1}{\beta}\left[\frac{1}{2}\ln\frac{2m_e c^2\beta^2\gamma^2 T_{\max}}{I^2} - \beta^2 - \frac{\delta(\beta\gamma)}{2}\right] \tag{1.9}$$

where m_e is the electron mass and r_e the classic electron radius, N_A is Avagardo's number[3], z is the charge of the incident particle in units of the electron charge e, Z and A are the charge and mass number of the target atoms, respectively, I is the mean excitation energy of the material in eV, and β and γ have their usual definition from relativity. $T_{\max}$ is the maximum energy which can be transfered to an electron in a single collision. The mean energy loss as function of the incident particle momentum is displayed in figure 1.3. In reality, the energy-loss for a given collision will fluctuate around a mean value which is given by the Bethe-Bloch equation. For thick detectors, the fluctuation is essentially Gaussian. For thin detectors, the energy loss can be described by the Landau function or a convolution of a Landau with a Gaussian. The Landau distribution [28] describes the asymmetric distribution of energy loss with a long tail to higher values. This is due the small number of collision in this regime where each collision has a probability to transfer comparably large amounts of energy to an electron in the material. These so-called *δ-rays* or *knock-on electrons* can travel in the material and release additional energy in secondary ionization.

1.1.5 Leakage Current/Noise

In a silicon diode under reverse bias, a current flow can be observed even in the absence of ionization in the detector. This effect is called *leakage current* (I_{leak}) or *dark current*. It originates from thermal creation of charge carriers in the detector which are collected before they can recombine. The leakage current has a strong dependence on the temperature, which can be parameterized as

$$I_{\text{leak}}(T) \propto \exp\left(-\frac{E_0}{kT}\right) \tag{1.10}$$

The leakage current also increases due to irradiation (see below).

[3] For numerical values of these and other constants cf. Appendix A.

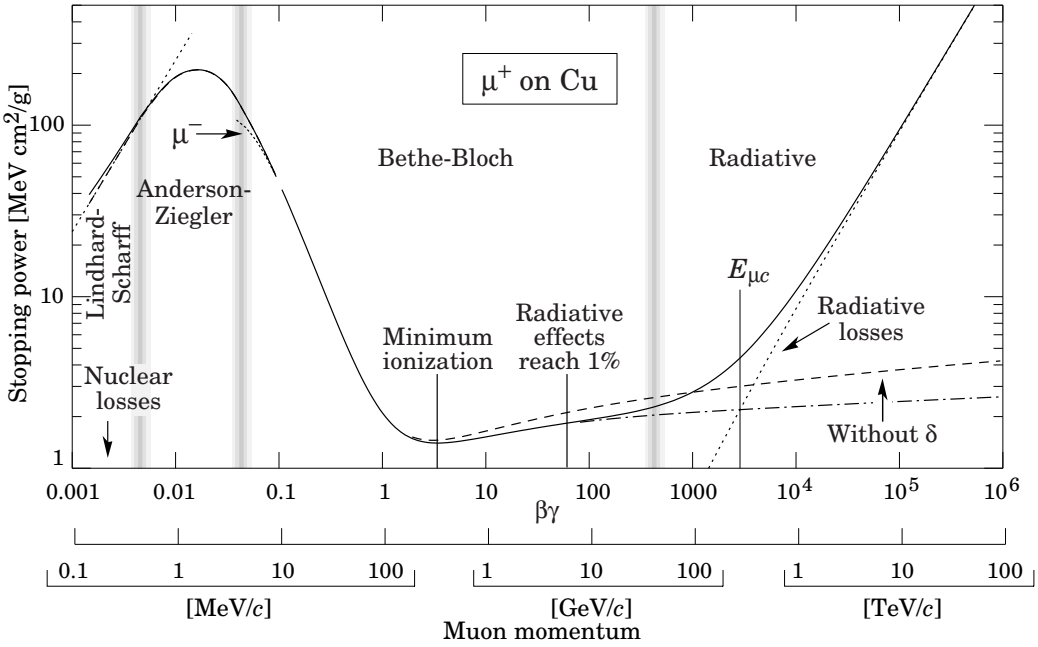

Figure 1.3: Mean energy loss for positive muons in copper as a function of the muon momentum. From [21].

1.2 Position Sensitive Semiconductor Detectors

In the most simple picture, a silicon detector is just a semiconductor *pn*-junction under reverse bias. The depleted silicon volume acts as a solid state ionization chamber. In order to obtain information about the position of a traversing particle, one side of the diode is realized as micro strip or pixel. Different options are available for the realization of the *pn*-junction. Often p^+ implants in an *n*-type bulk are chosen, but also other options as n^+-in-*n* silicon with a single *p*-type layer at the backside of the detector are possible (cf. section 3.2). The readout can be performed either in DC or AC mode. In DC mode, the strips are directly connected to the amplifier in the readout. In AC mode, the coupling is performed via a capacitor. Furthermore, the readout chain has to be grounded via a resistor. These two situations are schematically displayed in figure 1.4. In DC-coupled detectors the whole leakage current is collected by the amplifier. Since the leakage current increases with irradiation (see below), DC-coupling is disfavored in detectors which are exposed to a demanding radiation environment since large leakage currents make the design of suitable readout electronics very difficult. Instead the AC-coupled readout via a capacitor is chosen. To reduce the amount of material, mostly built-in electronics are used. This can be realized in the following way: the readout strip is formed from a highly doped p^+ material (cf. section 1.1.2). This is covered with an insulating layer of SiO_2. An aluminum layer is placed on top which can be easily connected to the readout electronics. This structure constitutes the capacitor C_c depicted in figure 1.4b. The resistor that is used for the connection to the ground potential can be realized e.g. by a poly-silicon structure. A guard ring is placed around the active detector region to isolate it from the sensor edge where high fields are present.

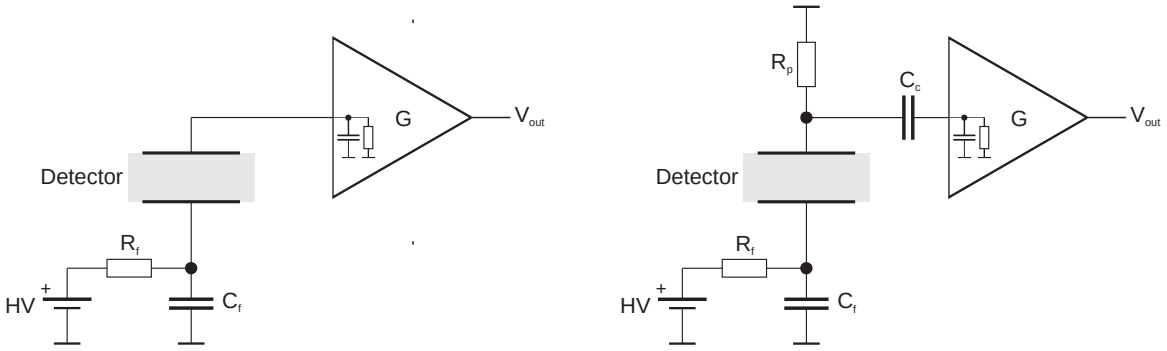

(a) (b)

Figure 1.4: Circuit diagram for a DC coupled detector (a) and an AC-coupled detector (b). In both cases, the backplane bias voltage is filtered by an RC network. From [29].

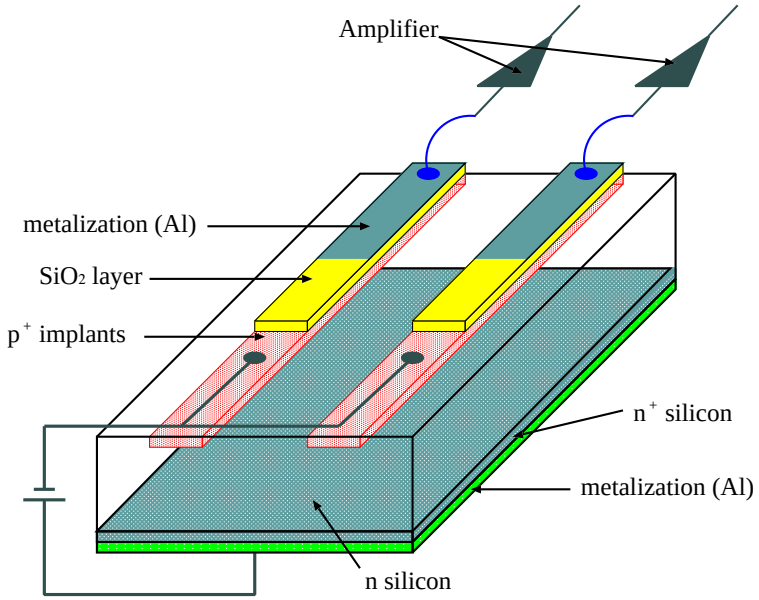

Figure 1.5: Schematic view of a segmented silicon diode.

A schematic cross-section of a silicon diode with an n-type bulk and p^+ implants is shown in figure 1.5. When a charged particle crosses the detector, it creates electron-hole pairs on its path. The electrons and holes drift in the electric field created by the voltage applied to the detector. Furthermore, the generated charge cloud spreads out due to diffusion. This spread is governed by the diffusion coefficient which depends on the temperature of the system as well as the mobility and charge of the charge carrier. Due to the different initial positions in the detector volume, the particles reach the electrodes at different times, which creates a time-dependent signal. In addition, the moving charges induce a signal on the

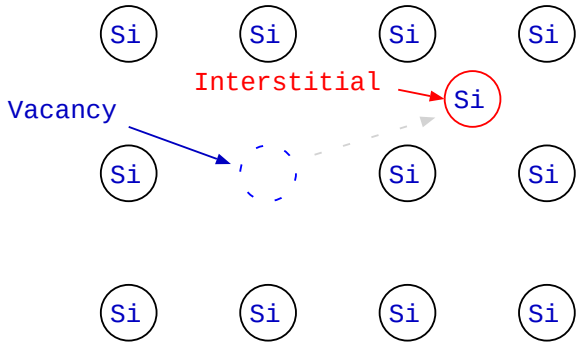

Figure 1.6: Schematic illustration of the creation of a vacancy and an interstitial by a hadronic interaction.

strips before reaching them. The position of the particle crossing can then be deduced from the amount of charge collected on the individual strips. Different clustering algorithms can be employed in different situations, which will be described in more detail in section 4.3.7.

1.3 Radiation Damage

As silicon detectors are often used in close proximity to the beam-line, they have to withstand large radiation doses, especially when operated at hadron colliders as the LHC. This is the most severe problem expected for the operation of silicon detectors and will limit the lifetime of the detectors to few years.

1.3.1 Classification of Defects

Radiation damage in silicon can be grouped into two major groups: surface and bulk damage, depending on the part of the detector in which they occur.

Surface damage refers to damage induced in the SiO_2 layer. It is mostly caused by ionizing energy loss in the layer. It leads to a gradual buildup of positive charge in this layer. This is due to the fact that electron-hole pairs generated in this region do not behave in the same way as in the bulk material. While electrons are highly mobile and are captured quickly, holes have a very low mobility and thus are captured in the layer. The charge buildup changes the capacitance of the detector and increases the surface current which adds to the leakage current.

Bulk damage (on the other hand) refers to changes in the silicon bulk. It is mostly caused by the non-ionizing energy loss (NIEL). Hadronic interactions displace silicon atoms (*primary knock-on atom*) from their nominal positions. The unoccupied lattice position is referred to as *vacancy*, the displaced atom, which most often will afterwards be placed at a non-lattice position is called *interstitial*. This situation is illustrated in figure 1.6. Single vacancies and interstitials are examples of *point defects*. Primary knock-on atoms can also displace other atoms to create whole *cluster defects*. The creation probability for cluster defects depends

on the particle type and the energy. The NIEL hypothesis states that this effect can be normalized to the effect of neutrons with an energy of 1 MeV.

1.3.2 Electrical properties of defects

Defects cause different changes in the properties of the material depending on their position in the band structure. Defects which are located near the center of the band gap can act as generation or recombination centers. This can lead to an increased leakage current by the creation of electrons and holes. Similarly, such defects can also trap electrons and holes and re-emit them at later times. This leads to a reduced charge collection efficiency. Defects which have a non-zero charge state at the operation temperature of the detector change the charge state of the whole material, i.e. they change the effective doping of the material. This change in the effective doping will result in a *type inversion* of the material after sufficiently large irradiation doses.

Another important aspect of radiation damage is an increase in the leakage current of a material. This increase depends linearly on the fluence Φ

$$\Delta I_{\text{leak}} \propto \alpha V_{\text{bias}} \Phi \tag{1.11}$$

where $\alpha = 10^{-17}\text{A/cm}$ for detectors after long-term annealing (see below).

1.3.3 The 'Hamburg Model'

The Hamburg model [30] describes the time evolution of the effective doping in semiconductors after irradiation. The change in the effective doping takes place during the so-called annealing process, which describes the reaction of defects within the detector material. Defects can drift in the material and react with lattice atoms or other defects. A simple example of this is the reaction of an interstitial with a vacancy. The reaction of defects is very much dependent on the ambient temperature. The annealing process almost completely stops at temperatures below -10°C. Above this temperature, the change in effective doping can be characterized by three distinct contributions, cf. figure 1.7.

Short-term annealing

The first contribution is a short term effect in the annealing of irradiated detector materials. After the warm-up the change in the effective doping is reduced compared to the state directly after irradiation. In case of type-inverted materials, this leads to a reduction of the depletion voltage. For materials before type inversion, the depletion voltage is increased. In both cases, the process can be regarded as beneficial for detector operation. It is therefore also referred to as *beneficial annealing*. Beneficial annealing happens mostly at room temperature or above.

Stable damage

The second contribution to the change in effective doping due to irradiation is the so-called *stable damage*. It does not change with the annealing time and gives a lower bound for the change in the effective doping due to annealing. The stable damage contribution increases linear with the fluence on the detectors and is the most important contribution to the change in the effective doping due to radiation damage.

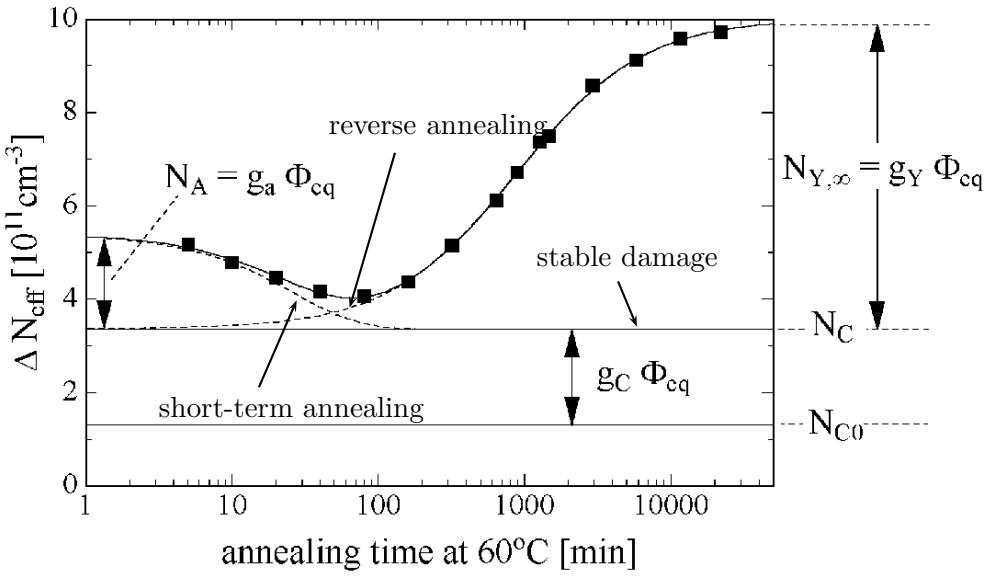

Figure 1.7: Evolution of the effective doping concentration for a 25 kΩcm material after a fluence of 1.4×10^{13} MeV neutron equivalent/cm^2 (from [30]). The three components of short term annealing, stable damage and reverse annealing are shown separately.

Reverse Annealing

The third part is the *reverse annealing* of a material. This is a process with considerable longer time scales as the short-term annealing and has the opposite effect. After longer periods at room temperature, the change in effective doping will instead increase, soon reaching levels higher than those directly after irradiation. This leads to unwanted changes in the operation parameters such as the depletion voltage. To avoid reverse annealing, maintenance periods with a warm-up of the detector to room temperature will be kept as short as possible once the detectors received larger amounts of radiation. Thus, the effects of short-term annealing should be maximized while keeping the contribution from reverse annealing small. The evolution of the effective doping for a 25 kΩcm detector material after an irradiation of 1.4×10^{13} MeV neutron equivalent/cm^2 as function of the annealing time is shown in figure 1.7. The contributions from the different annealing mechanism are indicated in the figure.

2 The Large Hadron Collider

The Large Hadron Collider (LHC) is a proton-proton collider storage ring which is housed in a tunnel formerly housing the Large Electron-Positron Collider (LEP) near Geneva, Switzerland, between Lake Geneva and the Jura mountains. It has a design center-of-mass energy of 14 TeV and a design peak luminosity of $10^{34}\text{cm}^{-1}\text{s}^{-1}$. The bunch spacing at nominal luminosity will be 25 ns, resulting in a collision frequency of 40 MHz. In figure 2.1 an aerial view of the LHC in the Geneva region displayed. The tunnel has a circumference of 27 km and is located at a depth between 80–100 m below the surface of the Swiss-French border region.

2.1 The LHC Accelerator Complex

The LHC will collide protons on protons, hence only one pre-accelerator chain is needed for both beams. The protons are first accelerated in the Linac2 and the Proton Synchrotron Booster, reaching an energy of 1.4 GeV at the end of these two steps. They are then transfered into the Proton Synchroton (PS). The PS, which has been in operation at CERN since 1959, was upgraded in order to meet the requirements for LHC. It was equipped with a 40 MHz RF system to be able to produce the 25 ns bunch structure foreseen for the LHC. In the PS, the energy is raised to 25 GeV, which is sufficient for the injection in the Super Proton Synchrotron (SPS). There the protons are further accelerated to 450 GeV, the injection energy into the LHC. The injection is performed via two transfer lines of about 2.5 km length; T18 for the clockwise beam and T78 for the anti-clockwise beam (where the numbering corresponds to the LHC sector numbering scheme). Part of the T78 transfer line from the SPS is shared between LHC and the CNGS[1].

The structure of the pre-accelerator chain, as well as requirements from the LHC itself, give constraints for the bunch structure in the LHC. A total of 72 bunches with a time distance of 25 ns are injected into the SPS at a time. Several of these bunch trains are inserted in the SPS with a spacing which is dictated by the rise time of the kicker magnets which deflect the beams coming from the transfer lines to the LHC orbit. Additional gaps are introduced during the insertion in the LHC, again due to the rise time of the insertion kicker magnets. Most important for the protection of the machine and the experiments is the abort gap with a total of 119 missing bunches which corresponds to 3 μs. This is sufficient to enable the extraction of the beams in case of a major problem. The foreseen bunch structure in the LHC at nominal luminosity and the intermediate steps are displayed in figure 2.2.

[1] **C**ERN **N**eutrinos to **G**rand **S**asso, which provides neutrinos beams for OPERA and other neutrino experiments.

Figure 2.1: Aerial view of the LHC ring in the Geneva region

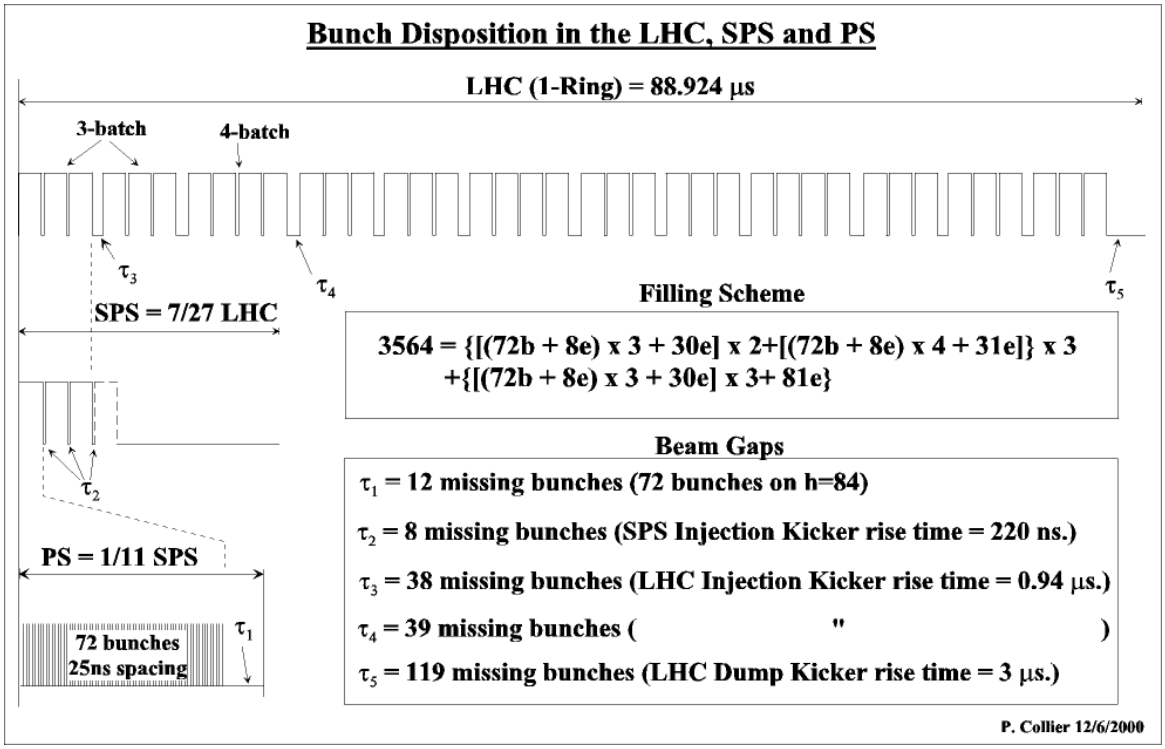

Figure 2.2: Bunch structure in the PS, SPS and one LHC ring. From [31].

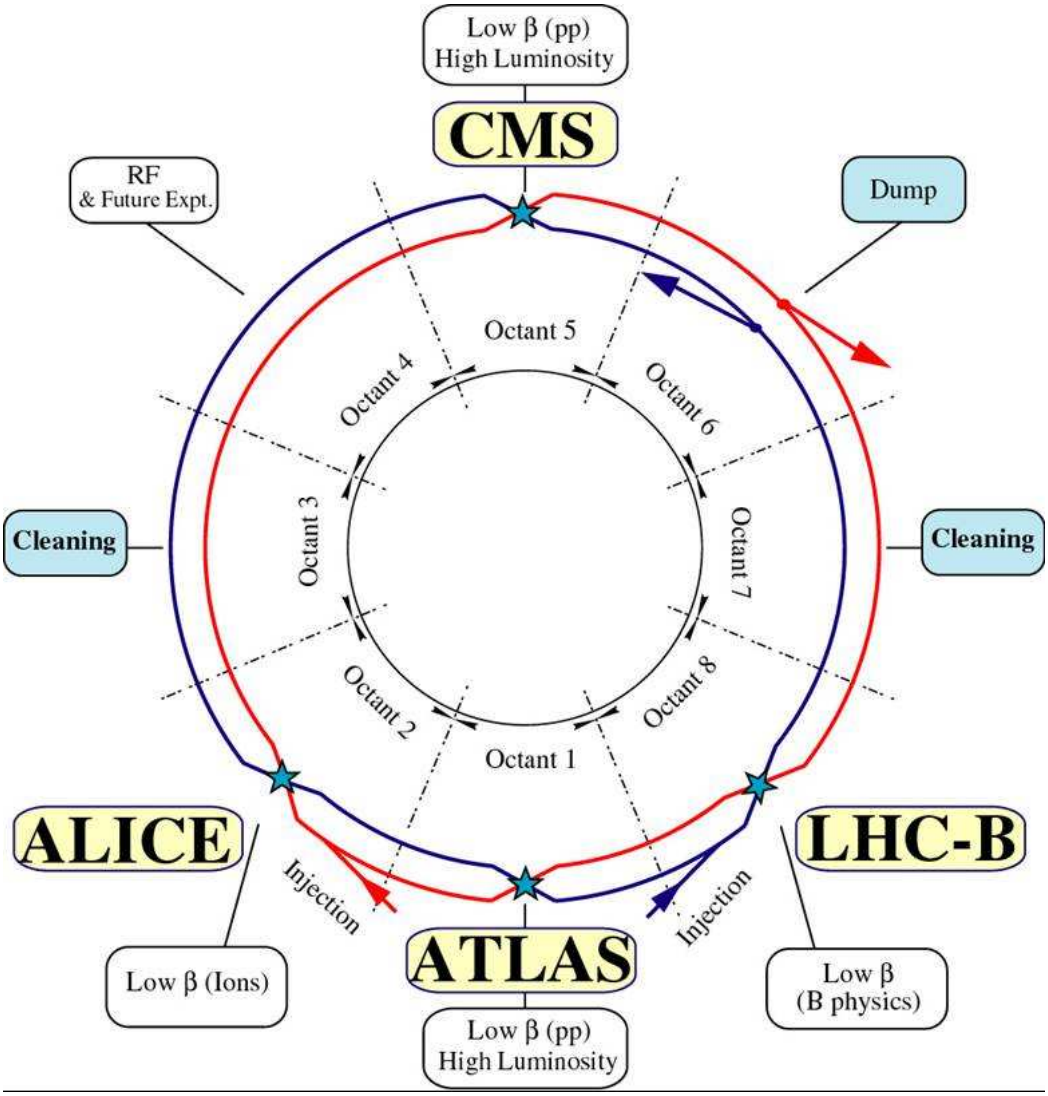

Figure 2.3: Schematic layout of the LHC main ring.

2.2 The LHC Main Ring

In table 2.1 the main parameters of the LHC accelerator are summarized. A total of 1232 superconducting dipole magnets are placed around the ring. They are operated at a temperature of 1.9 K and provide a magnetic field of up to 8.33 T at a current of 11700 A. The LHC uses a 2-in-1 magnet design where the two dipole magnets and the beam pipes for the two proton beams are integrated into the same magnetic yoke. Super-fluid Helium II at a temperature of 1.9 K is used for the cooling. The LHC consists of eight separate sectors which are cooled independently. The layout of the LHC main ring is displayed in figure 2.3. The acceleration is done using an RF system with a frequency of 400 MHz and an accelerating gradient of 5.5 MV/m at 7 TeV. The LHC has a total of 3564 buckets[2]

[2]A bucket is a possible bunch position

Table 2.1: Parameters of the LHC accelerator for nominal luminosity of $10^{34}\text{cm}^{-1}\text{s}^{-1}$.

Parameter	Unit	Value
Circumference	m	26658
Single Beam Energy [injection]	GeV	450
Single Beam Energy [collision]	GeV	7000
Magnetic Dipole Field [injection]	T	0.54
Magnetic Dipole Field [collision]	T	8.33
Beam Current	A	0.58
Protons per Bunch		1.15×10^{11}
Bunch Spacing	ns	24.95
Bunch Length	ns	1.06
Bunch Length	cm	7.5
Number of Buckets		3564
Number of Bunches		2808
Stored Energy per Beam	MJ	362

of which 2808 are filled at the nominal luminosity of $10^{34}\text{cm}^{-1}\text{s}^{-1}$. A single bunch contains slightly more than 10^{11} protons. Because of the beam structure of the LHC, the effective crossing frequency is 31.6 MHz which is equal to the number of bunches (2808) times the revolution frequency of 11245 s^{-1}. Together with the inelastic proton-proton cross section of about 60 mb, this gives rise to about $6{\times}10^8$ inelastic collisions per second or about 20 per bunch crossing, again at nominal luminosity.

A total of four interaction regions are located around the ring. They house the four experiments ALICE, ATLAS, CMS and LHC*b*. The LHC provides proton-proton collisions for all four experiments: ALICE, ATLAS, CMS, LHC*b* while collisions are only provided for ALICE, ATLAS and CMS, if heavy ions are accelerated. Because of the high number of bunches, a crossing angle of 285 μrad is foreseen to minimize beam-beam interactions in the high-luminosity interaction regions at P1 and P5 (ATLAS and CMS). More details on the LHC heavy-ion program can be found e.g. in [31, ch.13].

3 The Compact Muon Solenoid

This chapter is devoted to a description of the Compact Muon Solenoid (CMS) detector. The CMS detector is built to meet several requirements: excellent performance for the detection and measurement of muons, an excellent electromagnetic calorimeter to measure the energies of electrons and photons with high precision, a central tracking system for accurate momentum measurement for charged particles and a hermetic hadronic calorimeter to detect all energy from collisions. After a brief introduction, the main components of CMS, the tracking detectors, the electromagnetic and hadronic calorimeters, the muon system and the solenoid magnet will be described.

3.1 Introduction

The Compact Muon Solenoid (CMS) [32] is one of two multipurpose detectors at the LHC. It is located in an underground cavern at a depth of about 100 m near the village of Cessy, France. Its name comes from three distinct features, which are central to the performance of the detector:

- its relatively compact size (especially when compared to ATLAS),
- its ability to reconstruct muons up to very high momenta with high precision,
- the solenoid magnet which generates a magnetic field of up to 4 T, providing an excellent environment for the determination of momenta with the central tracking detectors.

As every multi-purpose high energy detector, CMS provides a highly hermetic coverage of the solid angle. It has an onion-like structure with components placed at radial distances ranging from 4 cm to almost 8 m from the beam.

In figure 3.1, a cut-away view of the CMS detector is shown with the most important components labeled. One of the central aspects of the CMS design is the choice of an all-silicon central tracker. Another important feature is the fact that the calorimeter system is placed inside the huge solenoid coil. This improves the accuracy of calorimetric measurements due to the reduced amount of material in front of them.

The assembly of the CMS detector took place in two stages. First, as many components as possible were assembled and tested on the surface. Several operating procedures were established and cosmic muon data was taken with all subdetectors during the so-called *Magnet Test and Cosmic Challenge (MTCC)* [33]. Instead of the final tracker, a prototype test structure with few silicon modules took part in this test [34]. After the end of the MTCC, commissioning of the individual subdetectors continued. The heavy elements of CMS were then lowered into the cavern between November 2006 and January 2008.

The CMS coordinate system has the origin at the nominal collision point in the detector. The z-axis points along the beam-line with the positive direction towards the

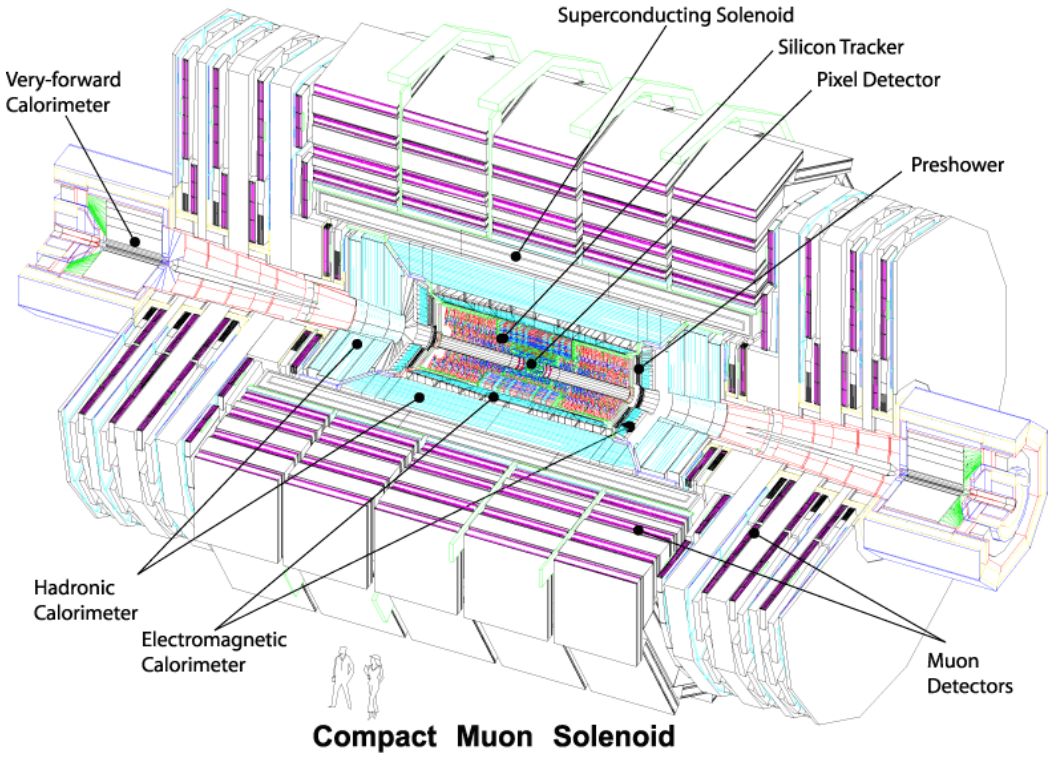

Figure 3.1: Cut-away view of the CMS detector.

Jura mountains. The y axis points upward and the x axis towards the center of the LHC ring. The azimuthal angle is denoted ϕ and the polar angle θ. The pseudorapidity is defined as $\eta = -\ln \tan \frac{\theta}{2}$.

3.2 Tracking Detectors

The CMS all-silicon tracker [35, 36] lies at the heart of the detector. It is divided into a pixel tracker as the innermost part, followed by the strip tracker. Both devices have similar coverage in polar and azimuthal angle and provide measurements with high spatial resolution. The pixel layers (discs) provide precise measurements in both x ($r\phi$) and y (r). Due to the high granularity, the mean occupancy in the pixel tracker is expected to be $\mathcal{O}(10^{-4}/\mathrm{cm}^2)$ at nominal luminosity. Together with the high spatial resolution this should enable an excellent performance for track seeding and reconstruction of primary and secondary vertices. At larger radii, the occupancy drops and hence micro-strip sensors can be used. The spacing and the length of the strips are increased for detectors at larger radii. The expected fluences of fast hadrons, the integrated dose and the charged particle flux are displayed in table 3.1 for an integrated luminosity of 500 fb^{-1}. The flux of charged hadrons is a good approximation for the fluence in 1 MeV neutron equivalent/cm^2. A schematic view of the whole CMS tracking system with the pixel tracker and the subcomponents of the strip tracker is shown in figure 3.2. Different design aspects of the tracker subsystems will be described in the following sections.

Table 3.1: Expected fluence of fast hadrons, integrated dose and charged particle flux at different radii within the CMS tracking system for an integrated luminosity of 500 fb^{-1}.

Radius (cm)	Fluence of fast hadrons (10^{14}/cm^2)	Dose (kGy)	Charged particle flux (cm^{-2}s^{-1})
4	32	840	10^8
11	4.6	190	
22	1.6	70	6×10^6
75	0.3	7	
115	0.2	1.8	3×10^5

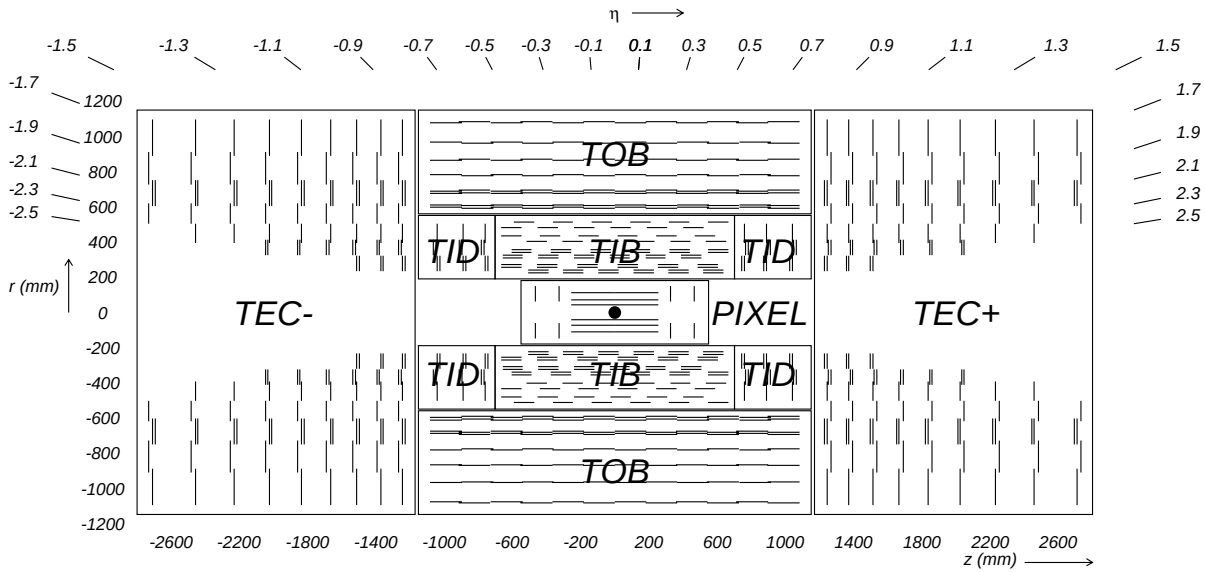

Figure 3.2: Schematic view of the CMS inner tracker with the individual subdetectors labeled. Double modules which provide 2D measurements are shown as double lines.

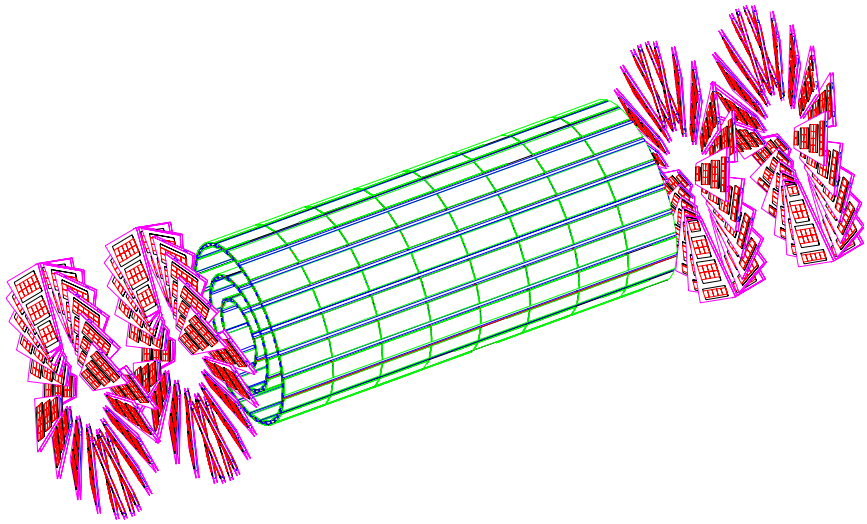

Figure 3.3: Illustration of the pixel detector in the CMS tracker.

3.2.1 Pixel Tracker

The pixel tracker is the inner-most part of the CMS tracking system closest to the interaction point. It is designed to provide a supreme resolution for primary and secondary vertices and to contribute three 2-dimensional measurements to the tracking for a robust track seeding and resolving of ambiguities. The pixel detector uses a zero-suppressed readout scheme with analog pulse height read-out [37]. The layout of the pixel tracker is shown in figure 3.3. It consists of two sub-parts, the pixel barrel (PXB) and two pixel endcaps (PXE).

Pixel Barrel

The pixel barrel consists of three layers of silicon pixel modules which are located at radii of 4.4, 7.3 and 10.2 cm from the beam pipe. It has an overall length of 53 cm. The silicon modules are mounted on so-called blades which are made of carbon fiber. The blades have a thickness of only 240 μm and are used for support and for the distribution of the cooling to the modules. The blades are glued to cooling tubes which also constitute the main support structure for the PXB system. The whole barrel is split along the y-axis into two half-barrels to enable installation and access without disturbing the beam-pipe. Furthermore the PXB system is split electrically into a part at positive and negative z. The cables for the individual half cylinders are routed to the PXB from both sides of the interaction region using two supply tubes. The modules of the PXB cover an area of 0.78 m^2 and have a total of 48 million readout channels. Due to the large magnetic field from the CMS solenoid, the Lorentz-drift spreads out the charge generated in the pixel sensors. This effect can be used for the improvement of the spatial resolution, due to the analog read-out of the data from the sensors.

Pixel Endcaps

In the two pixel endcaps, two discs with silicon sensors are placed on either side of the interaction region at $|z|$=35.5 cm and $|z|$=46.5 cm. They extend the coverage of the pixel tracking system to the region $|\eta|$ <2.5, consistent with the coverage of the strip tracking system. At the largest pseudorapidities, the two disc measurements can be combined with a single measurement from the innermost layer of the PXB. Similar to the barrel part, also the pixel endcaps consist of two mechanically independent half-cylinders to allow installation around the beam pipe. Each of the half-cylinders contains two half-discs. On these, so-called *panels* are mounted which form the lowest-level mechanical structure. The panels are made of beryllium and have a thickness of 500 μm. The panels of the PXE are mounted in a turbine-like structure at an angle of 20° with respect to the plane normal to the beam direction. This enables charge-sharing among neighboring pixels which leads to an improved spatial resolution. The silicon modules are mounted on the panels in groups from 1×2 to 2×5 plaquettes, where a plaquette is a single silicon sensor together with its read out chips and its interconnect. The pixel endcaps have an active area of 0.28 m^2 with a total of 18 million readout channels.

Pixel Sensors/Modules

The sensors of the pixel detector are based on an n-on-n structure, i.e. high-doped n^+-type implants are embedded into an n-type bulk material. The pn-junction is realized at the backside of the detector. The read-out is connected on the n^+-side, which is kept on ground potential at all times. The individual pixels have a size of 100×150 μm^2. Due to charge sharing, this results in a single hit resolution of 15-20 μm [37]. The barrel sensors use radiation-hard DOFZ[1] material and a $\langle 111 \rangle$ crystal orientation [38]. The active material has a thickness of 285 μm and a resistivity of about 3.7 kΩcm. The sensors for the pixel barrel were produced from 4" wafers and use p-stop for the inter-pixel isolation. Due to the choice of n-in-n detectors, operation of the detectors is still possible in partial depletion. It is expected that the innermost layer of the pixel tracker will stay operational for at least two years at nominal luminosity [37].

3.2.2 Strip Tracker

The silicon strip tracker (SST) of the CMS experiment [36] is the largest silicon tracker ever built. With an active area of over 200 m^2, the SST provides a very good spatial resolution for charged particle tracks in the pseudorapidity range -2.5 < η < 2.5. It extends radially from about 22 cm to 120 cm from the beam line. The strip tracker is divided into mechanically independent subdetectors (see figure 3.2), the tracker inner barrel (*TIB)*, the tracker inner discs (*TID)*, the tracker outer barrel (*TOB)* which surrounds both TIB and TID and the two large tracker end caps (*TEC)* which complement the tracking system on either side of the TOB. The strips in the strip tracker are aligned parallel to the z-axis in the barrel part and parallel to r in the endcaps. In addition, in two layers of both TIB and TOB and two (three) rings in the TID (TEC), special stereo modules are combined with the standard modules to provide a 2D measurement. In these modules, the strips are rotated by an angle of 100 mrad with respect to the nominal direction. The choice of the stereo angle is a

[1] Diffusion oxygenated float zone.

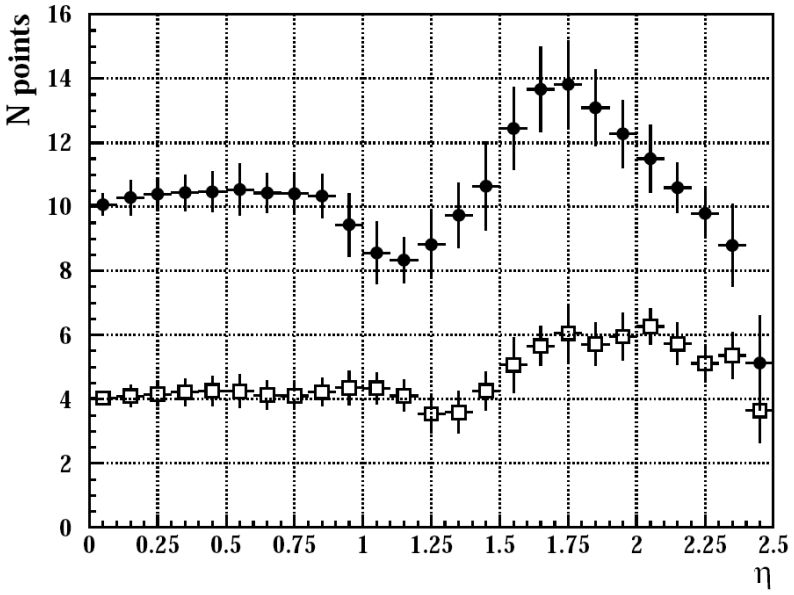

Figure 3.4: Number of measurement points in the CMS strip tracker as function of pseudorapidity. Filled circles show the total number of measurements while open circles show the number of stereo measurements [37].

compromise between resolution and combinatorics, since with a small stereo angle, not all combinations of strips have to be taken into account in the 2D clustering. The resolution which can be achieved along the otherwise insensitive coordinate is about 230 μm in the TIB and 530 μm in the TOB. The CMS strip tracker provides up to 14 measurements for track reconstruction, depending on pseudorapidity. Up to 6 of these can provide 2D information. The number of possible tracking points as a function of η is displayed in figure 3.4.

Tracker Inner Barrel/Inner Disc

The tracker inner barrel and tracker inner disc are the strip subdetectors that are closest to the interaction region. The modules are grouped in four layers in the inner barrel and two times three discs in the inner discs. The first two layers of the TIB and the inner two rings of the TID contain stereo modules for 2D measurements. The layers of the TIB are placed at radii of 25.5, 33.9, 41.85 and 49.8 cm from the beam line. The TIB extends to $|z| < 70$ cm around the interaction region. The two times three TID discs are located between $|z| = 80$ and $|z| = 90$ cm with modules at radii between 20 and 50 cm. Together, TIB and TID cover the whole pseudorapidity interval $|\eta| < 2.5$. The modules in the TIB have a strip pitch of 80 μm for the inner two layers and 120 μm for the outer two layers. In the TID, the modules have a strip pitch varying from 80.5 to 158 μm, due to the wedge shaped structure of the modules. The TIB is split into two half barrels at $z = 0$ (TIB$\pm$). Each of the four TIB layers is split into an upper and lower half-shell along z. The smallest mechanical structure of the TIB is a string, which contains three modules (six in case of stereo layers). These are

then mounted on the half-shells for each layer. The half-shells of the individual layers are combined into half-cylinders which are finally combined into the TIB± structures.

Tracker Outer Barrel

The tracker outer barrel has a single support structure without any subdivision. The fundamental assembly units of the TOB, so-called *rods* are inserted at predefined positions from both sides of the support structure. A rod contains 6 modules (12 in case of stereo layers) plus the necessary cooling and readout infrastructure. A total of 688 rods are used. Inside the support structure the rods are arranged to form a structure of six layers which consist of 48 to 72 rods. The layers are placed at radii of 60.8, 69.2, 70.8, 86.8, 96.5 and 108.0 cm. The first two layers contain rods with stereo modules for 2-dimensional measurements. The rods are arranged to overlap in ϕ and z to provide hermetic coverage. The strip pitch is 122 μm for the stereo layers and 183 μm for the other layers. The TOB has a total length of 2.36 m including cabling. The inner diameter is 55.5, the outer 116 cm. The TOB contributes to track measurement up to a pseudorapidity of about $|\eta| < 1.3$.

Tracker Endcaps

The two tracker endcaps complete the silicon tracker on both sides of the interaction region, providing coverage up to the full pseudorapidity range $|\eta| < 2.5$. They are located at a distance of 1.24 m from the interaction point and extend along z for more than 1.5 m up to $|z| \approx 2.8$ m. The radial extension goes from 22.0 cm up to 113.5 cm, where the first is equivalent to the first layer of the inner barrel (inner disc), while the latter corresponds to the outermost layer of the outer barrel. The two TECs are organized in 9 discs in which the silicon modules are organized in rings of equal radius. The discs contain between 4 and 7 rings of silicon modules depending on their position in z. The first three discs contain 7 rings, in discs 4 to 6 the ring closest to the beam pipe is not present, discs 7 and 8 also have the second closest ring removed and the last disc (9) only contains the outermost four rings. This can be done without affecting the coverage in pseudorapidity. Each of the nine discs is divided into 8 sectors in ϕ. Each of these consists of two independent wedge shaped structures, so-called *petals*. The two petals have a different arrangement of silicon modules to provide optimal coverage in ϕ. The two petal types are referred to as *front* and *back petal*. To enable a good coverage along r, the modules are mounted on the petal from the front and the backside alternating from ring to ring. In each disc (if present) the rings 1 and 2 and the ring 5 contain stereo modules.

Strip Sensors/Modules

The sensors for the CMS silicon strip tracker were produced using standard 6" wafer technology. Float zone material is used for the silicon bulk. A $\langle 100 \rangle$ crystal orientation is chosen in order to minimize the effects of surface damage [39]. Two different thicknesses are used. For the sensors of the inner barrel, the inner discs and the first four rings of the two TECs, *thin sensors* with a thickness of 320 μm are used. For the sensors of the outer barrel and the rings five to seven of the TECs, sensors with a thickness of 500 μm are used (so called *thick sensors*). Two thick sensors are wire-bonded in the respective modules. The increased strip length can be afforded since occupancy drops at larger radii. Furthermore it reduces

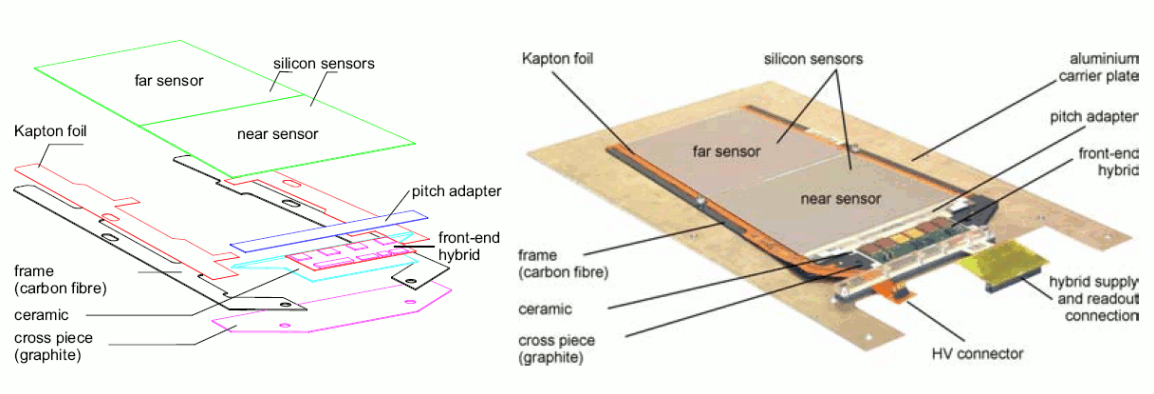

Figure 3.5: Exploded view of a module from the CMS strip tracker. From [37].

cost and power consumption. This comes at the cost of a higher noise, which is however compensated by the larger thickness and corresponding higher signal level due to larger ionization losses of the traversing particle. The increased strip length also compensates the reduced capacitance due to the increased thickness. The resistivities of the sensors are 1.5 - 3.25 kΩcm for the thin sensors and 4 - 8 kΩcm for the thick sensors. The strip tracker uses p^+ implants in an n-bulk material. An n^+ layer is placed at the backside to ensure a good ohmic contact which is complemented by an aluminum cover. The p^+ implants are covered by a SiO_2 layer which is followed by an aluminum cover providing an AC coupling of the strip to the readout. The sensors are produced by two vendors: Hamamatsu Photonics and ST Microelectronic. A total of 24,244 silicon sensors with an active area of almost 200 m^2 are used in the silicon strip tracker. The individual sensors are mounted on a frame of carbon fiber or graphite for support. In case of sensors in the outer part of the tracker (TOB and TEC ring 5–7), two sensors are mounted on the same frame and are connected using wire-bonds. Each sensor is equipped with 4 or 6 APV readout chips (cf. section 3.2.6). In addition the support structure houses a kapton wire which is connected to the back plane of the module and provides the bias voltage of up to 500 V to the silicon bulk. The wire is also equipped with thermal probes to measure the temperature of the silicon. Additional components which are mounted on the support structure are a pitch adapter which adjusts the pitch of the detector to the one of the APV readout chip, and a front-end hybrid. This carries the APV chips, the APV multiplexer. A blown-up view of a silicon module is shown in Figure 3.5. A total of 15 different sensor geometries are produced to provide best possible coverage in both η and ϕ. Due to other differences in certain module positions, a total of 29 different module designs are used in the strip tracker.

3.2.3 Tracker Support Tube and Thermal Shield

The whole central tracking system of CMS is housed in a special *tracker support tube (TST)*. The TST is made of two layers of carbon fiber on the in- and the outside with a Nomex core[2]. The dimensions of the TST are 5.30 m and 2.38 m in length and diameter, respectively. The TST has to fulfill two main purposes: Mechanical support of the tracker elements

[2]Nomex is a trade name for a meta-aramid.

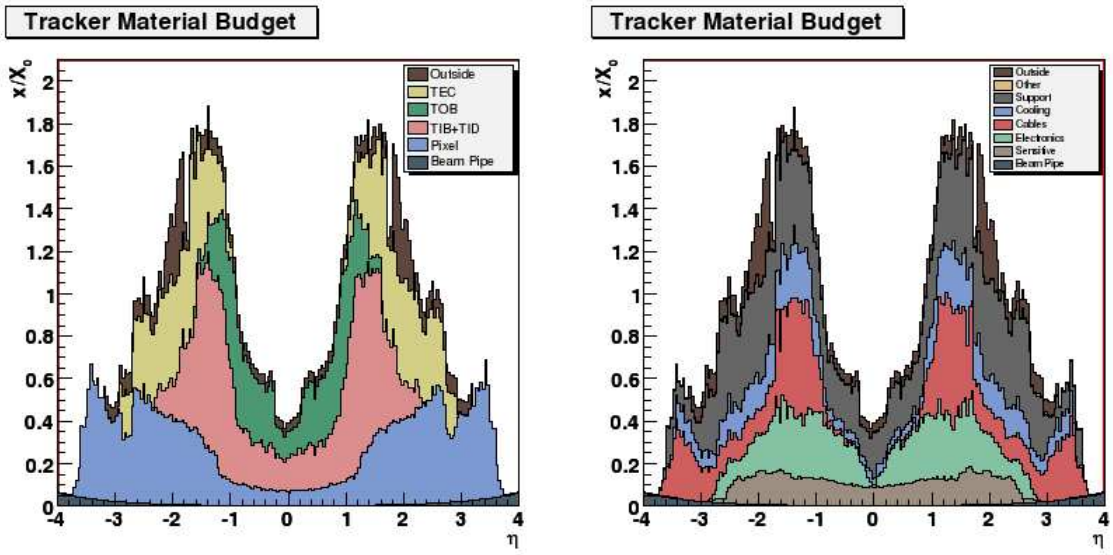

Figure 3.6: Material budget of the CMS tracking system as function of η (From [37]).

and thermal shielding of the tracking system towards the calorimeters. The mechanical support of the tracker is provided by two carbon fiber rails which support the TOB and TEC inside the TST. The thermal shielding of the system is necessary to compensate the large temperature gradient from -10°C inside the tracker volume to +18°C which is the nominal operating temperature of the ECAL. Due to the large temperature sensitivity of the ECAL crystals, the temperature has to be stable within fraction of degrees. The outside of the TST is heated by several resistive circuits. The cooling on the inside is performed in analogy to the tracker cooling with cooling fluid being circulated in an aluminum plate.

3.2.4 Material Budget

Due to the large number of silicon modules in combination with support structures, power cables, cooling and readout electronics, the material budget of the tracker varies by large amounts as a function of η. The distribution of the material for the different subdetectors on the one hand, and divided according to the type of material (active silicon, cooling, support etc.) on the other, is shown in figure 3.6. One can see that at central pseudorapidities ($|\eta| \lesssim 0.4$) the material budget adds up to only about 0.4 radiation lengths while at pseudorapidities between $|\eta| \approx 1.2$ and $|\eta| = 1.8$ the material budget increases up to 1.8 radiation lengths. This is in part due to the geometrical increase proportional to $1/\sin\theta$. In addition several cable routings from the inner detectors which have contribute to the material budget in front of the other subdetectors.

3.2.5 Cooling

The cooling system for the CMS tracker is conceived to provide a cooling power of 60 kW which is expected to be dissipated inside the tracking volume with a large safety margin. The input temperature of the cooling fluid can be as low as -35°C with a flow of 77 m^3 per

hour. The system will be operated at a pressure of 8 bar. To inhibit any condensation of moisture in the system, the humidity has to be kept very low to keep the dew point well below the operating temperature. For this, the tracker volume is flushed with nitrogen with a flow of about 25 m^3 per hour.

3.2.6 Tracker Control and Data Acquisition

The CMS tracker uses an analog readout system. With this, charge sharing can be used to improve the spatial resolution with respect to a binary readout where no information about the signal height is available. The signal from the silicon sensors is read out by the APV25 readout chip (see below). There the signal is pre-amplified, shaped and then stored to await the decision from the first level trigger (for details cf. section 3.6). If a first level trigger accept is sent, the signal is read out from the pipeline and transfered to a multiplexing unit that combines signals from two APV chips. The signal is then transformed into an optical signal and transfered over about 100 m out of the experimental cavern to the Front End Driver (FED). Here, the signal is further processed. The dynamical range of the readout system is designed to be about 3 MIPs.

For the controlling and monitoring of the tracker, about 300 *control rings* are used. These begin and end at the Front End Controllers (FEC) which distribute the clock and trigger signals. The distribution is made via a digital-optical link. Inside the detector volume, the optical signals are converted by Digital-Opto Hybrids (DOH) to electrical signals which are relayed to the individual front end chips. The timing delay for individual modules can be adjusted by a phase lock loop (PLL) module with an adjustable delay line. The same optical line is used for the transmission of the monitored values of leakage current, the power supply voltages and the temperatures of the APV chip and the front end hybrid, which are monitored by so-called *detector control unit* (DCU) chips.

The individual components of the data acquisition system will be described in the following.

APV25 Readout Chip

The APV25 readout chip (APV) [40] is based on 0.25 μm CMOS technology. It reads the signal of 128 detector channels. The APV is equipped with a low-noise pre-amplifier and a CR-RC shaper. The shaping time is 50 ns. The resulting signal is sampled at a rate of 40 MHz and stored as an analog signal in a pipeline with 192 consecutive elements[3] which corresponds to 4.8 μs. The APV provides two different readout modes which will be described in more detail below. It needs two supply voltages of 1.25 and 2.5 V. The total power consumption of the APV is about 300 mW which corresponds to about 2.3 mW per channel.

Analog Opto Hybrid/Laser Driver

The data from the APV is transmitted out of the experimental cavern using an optical link system. For this, the signal of two APV chips is taken by a custom built chip, the so called *APVMUX* and is multiplexed onto a single optical input line. The signal is then converted to an optical signal on the *analog-opto hybrid* (*AOH)*, which is connected to an optical

[3] This gave the APV its name, which is derived from **A**nalog **P**ipeline **V**oltage

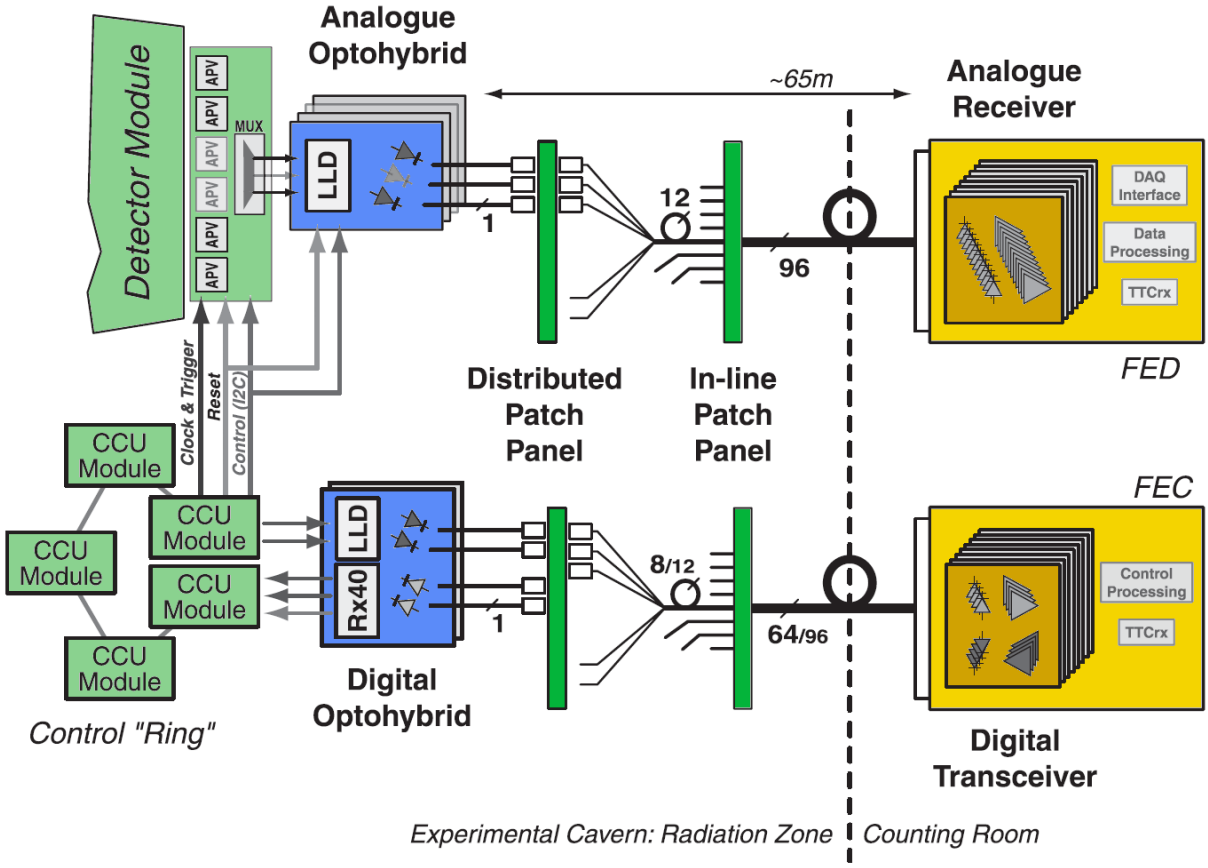

Figure 3.7: The analog readout optical link.

driver. The so-called *linear laser driver (LLD)* modulates the amplitude of an InGaAsP edge-emitting device which is used for the transmission of the signal. InGaAs photo diodes are used at the reception side. The laser system is equipped with a switchable gain at the transmitter side which can be used to adjust the overall gain of the optical system. The overall gain factor of the optical link is optimized around a value of 0.8, which is dictated by the APV sensitivity of about 100 mV/MIP and the ADC resolution of the front end driver (250 mV/8 bit) which results in an optimal gain of 0.8, if a signal of 3 MIPs should be transmitted [41]. A complete view of the optical link system is displayed in figure 3.7.

Front End Driver

The front end driver unit (FED) receives the signal of 96 optical fibers which corresponds to 192 APV chips or 24,567 channels. The FED takes the raw signal and performs several steps: Pedestal subtraction, common mode determination and zero suppression. During different stages in the commissioning, one or more of the above steps can be skipped to gain a deeper understanding of the data coming from the detector. In normal data taking, the data is digitized with a 10 bit ADC. The precision of the data transfered to the data

acquisition is 8 bit. In commissioning mode (cf. chapter 5), the data can be read out with 10 bit precision.

Readout Modes

The APV provides two different readout modes, the *peak mode* and the *deconvolution mode*. These are conceived to cope with different running scenarios. During the low to medium luminosities phase, when the occupancy of the tracker is moderate, the peak mode is chosen because it provides the better signal-to-noise performance. At nominal luminosity, the deconvolution mode is chosen. It provides better timing resolution, thus enabling a good separation of signals from adjacent bunch crossings.

In peak mode, a single point from the APV CR-RC shaper is read out. The exact sampling position can be adjusted in 1 ns steps. The CR-RC shaper has a time constant of $T_p = 50$ ns. The time evolution can be parameterized as:

$$p(t) = Q_c \frac{t}{T_p} \exp\left(-\frac{t}{T_p}\right), \tag{3.1}$$

where Q_c is the collected charge. The output reaches a maximum after the time T_p; this constant is also known as *peaking time*.

To reduce the tail of the CR-RC shaper signal, a second read out mode is foreseen. In this deconvolution mode, the signal from the shaper is sampled at three positions with 25 ns separation. The output signal is reconstructed from three samples from the pipeline at 0, -1 and -2 bunch crossings:

$$d_k = w_3 p_{k-2} + w_2 p_{k-1} + w_1 p_k \tag{3.2}$$

with the coefficients w_i given by:

$$\begin{aligned} w_1 &= A\frac{\exp(x-1)}{x} \\ w_2 &= A\frac{-2\exp(-1)}{x} \\ w_3 &= A\frac{\exp(-x-1)}{x} \end{aligned} \tag{3.3}$$

where x is the ratio of the shaping time T_p and the sampling time T which is equal to the bunch crossing frequency of 25 ns, and A is a normalization constant. For this situation the above w_i take the values of

$$w_1 = 1.21306 \qquad w_2 = -1.47152 \quad w_3 = 0.44626. \tag{3.4}$$

The two signal shapes for peak and deconvolution are displayed in figure 3.8. One can see that in deconvolution mode the signal is essentially zero after 50 ns, which should enable a good separation even at the highest occupancies. The deconvolution comes at the cost of an about 50% higher noise compared to peak mode (e.g. [37]).

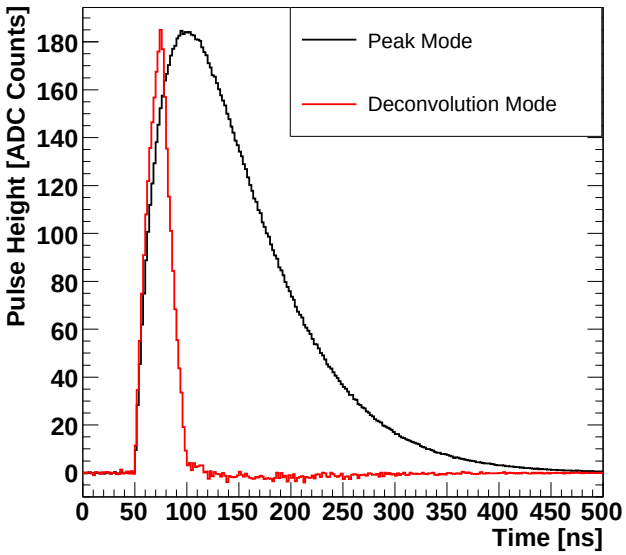

Figure 3.8: Signal shapes for peak (black) and deconvolution (red) readout mode.

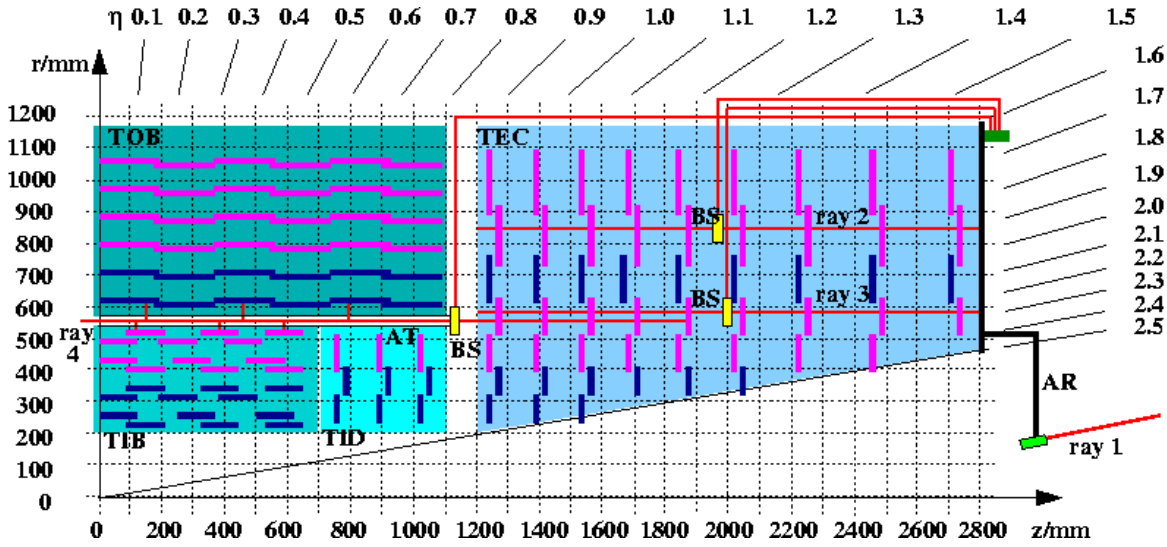

Figure 3.9: Overview of the CMS laser alignment system.

3.2.7 Laser Alignment System

The laser alignment system (LAS) of the strip tracker is used to provide a relative position measurement of the larger structures of the system. Via a system of 40 laser beams, TIB, TOB and the two TECs are aligned with respect to each other and, in case of the TECs, also internally. In an eightfold ϕ-symmetry, two beams penetrate the back petals of all nine TEC discs in ring 4 and 6, respectively. For this, a hole is etched in the aluminum back plane of the respective modules. With this beams, movements of the discs with respect to each other can be determined. Additional beams are transmitted via beam splitters to hit modules in TIB, TOB and both TECs at the same time, which provides information about movements of the subsystems. An overview of the LAS with the different rays indicated is shown in figure 3.9. The ultimate precision of the laser alignment has been estimated to be below 40 μm [42].

3.3 Calorimeters

CMS has an electromagnetic and a hadronic calorimeter, which employ different techniques both in conception and technology. The calorimeters of CMS are located inside the solenoid magnet. This has the advantage that no additional material is introduced in front of the calorimeters which reduces multiple scattering, absorption and other disturbing effects on particles leaving the tracking system. It also decreases the extrapolation distance from the tracking system to the calorimeters. The disadvantage is the limited amount of space available for the calorimeters. This can be seen especially on the CMS hadronic calorimeter which employs a tail catcher outside the solenoid to determine leakage from the calorimeters into the non-instrumented solenoid.

3.3.1 Electromagnetic Calorimeter

The CMS electromagnetic calorimeter (ECAL) constitutes the first part of the CMS calorimetry system. It is hermetic in the polar angle ϕ and covers the pseudorapidity region $|\eta| < 3.0$. It is a homogeneous calorimeter, i.e. the same material is used both as absorber and scintillator. The ECAL is divided into a barrel (EB) and two endcaps (EE). In addition, a preshower detector is placed in front of the endcaps. The calorimeter uses lead tungstate crystals ($PbWO_4$) for the creation and detection of electromagnetic showers. For the light collection, two different systems are employed: Avalanche photo diodes in the barrel region and vacuum photo triodes in the endcaps.

The energy resolution of calorimeters can be parameterized as

$$\left(\frac{\sigma_E}{E}\right)^2 = \left(\frac{S}{\sqrt{E}}\right)^2 + \left(\frac{N}{E}\right)^2 + C^2 \tag{3.5}$$

where there are three contributions: A stochastic term (S) which among others characterizes event-to-event fluctuations in the lateral shower extension and photo-statistics, a noise term N which comprises all noise contributions from the system like electronics noise, digitization noise and possible pileup noise, and a constant term C which takes into account leakage from the back of the crystals, possible non-uniformities in the light collection and inter-calibration errors among neighboring crystals. The energy dependence of the energy resolution is shown

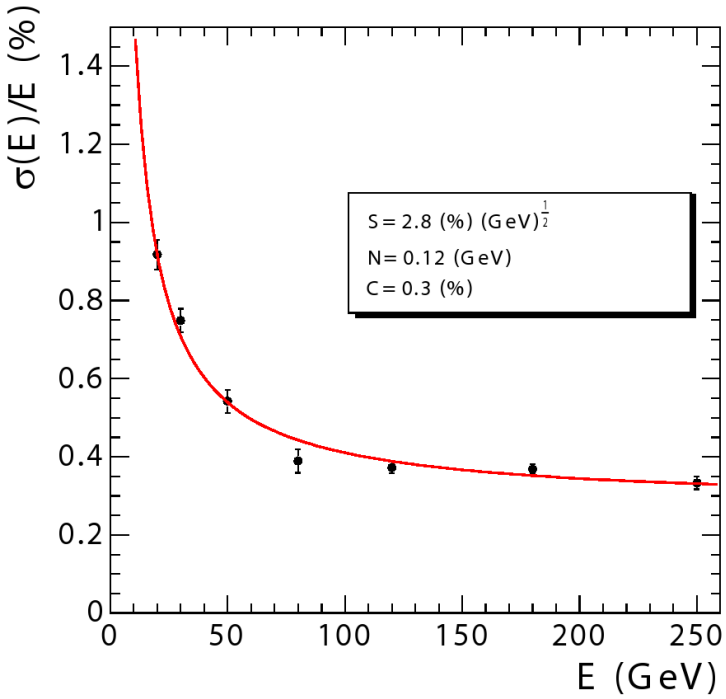

Figure 3.10: Energy resolution of the CMS electromagnetic calorimeter as function of the incident particle energy. The coefficients of the parameterization are indicated in the figure.

in figure 3.10 where the numerical values of the terms are also given. The performance of the ECAL is designed to enable e.g. the detection of high energy photons from rare decays of the Higgs boson into two photons. A transverse view of a quarter of the CMS ECAL is shown in figure 3.11.

$PbWO_4$ Crystals

Lead tungstate crystals have a number of advantages which make them a good choice for an absorber material, the most important ones being

- a very high density of 8.28 g/cm^3,
- a short radiation length of 0.89 cm and
- a small Molière radius of 2.2 cm.

Due to the small radiation length, the calorimeter can be compact in radius: The radial length in the barrel region of 230 mm for the crystal corresponds to 25.8 radiation lengths, which guarantees a very good confinement of electromagnetic showers in the ECAL. The small Molière radius allows the construction of a very granular calorimeter since also the lateral shower profile is very compact. This leads to little leakage among neighboring towers even for very compact crystal sizes. Drawbacks of lead tungstate are

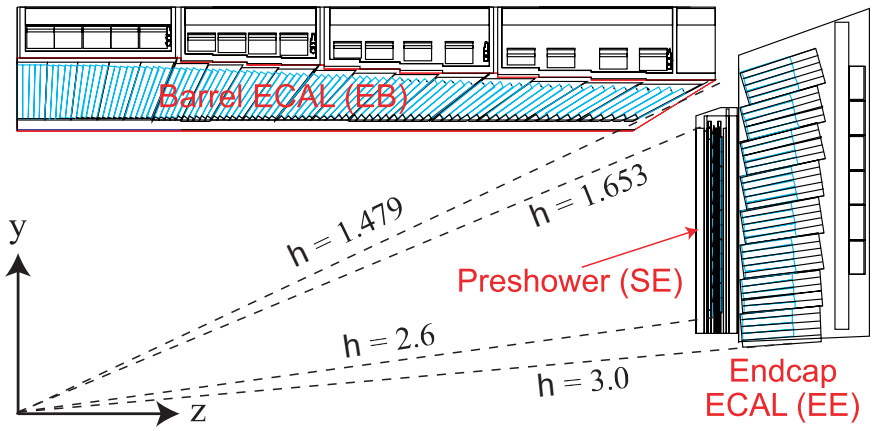

Figure 3.11: Transverse view of one quarter of the CMS EM calorimeter.

- large temperature dependence of the generated signal and
- relatively low light yield.

The employed photo detectors also have a temperature dependence. The combined dependence of the signal from the crystals and the diodes has been determined to be $-(3.8 \pm 0.4)\frac{\%}{°C}$ of which $-2.1\frac{\%}{°C}$ come from the crystals alone. This means that the temperature of the calorimeter has to be kept constant within a fraction of a degree to ensure a good and stable energy resolution. The foreseen operation temperature is 18±0.05°C. Furthermore, the light yield of lead tungstate is relatively low, at 4.5 photoelectrons per MeV which are detected by the photo detectors. Due to this low yield, it has to be ensured that the properties of the crystal do not deteriorate too much over the projected lifetime of the calorimeter.

ECAL Barrel

The EB consists of 61,200 $PbWO_4$ crystals which have a cross section of 2.2×2.2 cm^2 facing the beam[4]. It covers the pseudorapidity interval $|\eta| < 1.479$. The EB starts from a radius of 1.29 meters with a crystal length of 23 cm. The depth at $\eta = 0$ is 25.8 radiation lengths. The ECAL barrel is organized into 36 so-called *super-modules*, 18 in both the $+z$ and the $-z$ halves. Each super-module covers an azimuthal angle of 20°. Each super-module is made up of 1,700 $PbWO_4$ crystals. For triggering, the crystals are organized in groups of 5×5 crystals which are used as input for the trigger primitive generator (cf. section 3.6).

ECAL Endcaps

The two ECAL endcaps of CMS cover the pseudorapidity region $1.479 < |\eta| < 3.0$. Each endcap consists of two large substructures, so called *Dees*[5]. This design enables installation and maintenance of the components without the need to disassemble large structure or to

[4]This corresponds to an $\eta - \phi$ region of 0.0174×0.0174.
[5]The name comes from the resemblance of the structures to the letter **D**.

break the vacuum of the beam pipe. The two endcaps consist of 7,324 crystals each. These are organized into *super-crystals* of 5×5 crystals.

Preshower Detector

A two layer pre-shower detector will be placed in front of the ECAL endcaps. It covers the pseudorapidity region $1.653 < |\eta| < 2.6$ and has a length along z of 20 cm. Its goal is to enable a good identification of π^0 mesons on the one hand, and a separation of electrons and photons on the other hand. The preshower detector uses two layers of lead as radiator material, each followed by a layer of silicon modules. The strip sensors (so-called micro modules) have an active area of 61×61 mm^2 and have 32 strips each. In total the preshower detector comprises 4,300 micromodules which corresponds to a total of 137,000 readout channels. The preshower detectors are foreseen for installation in the 2008/09 shutdown phase.

3.3.2 Hadronic Calorimeter

The CMS hadronic calorimeter surrounding the ECAL consists of three separate parts, the HCAL Barrel (HB), the two HCAL Endcaps (HE) and the two HCAL forward units (HF). The calorimeter covers the pseudorapidity region $|\eta| < 5.0$, with the individual parts covering:

- HB: $|\eta| < 1.3$
- HE: $1.3 < |\eta| < 3.0$
- HF: $3.0 < |\eta| < 5.0$

For the barrel and the endcap region, the calorimeter uses brass as an absorber material interleaved with scintillator. In the forward region iron is used as absorber, while quartz fibers are used for the scintillation. The performance of the different parts of the hadronic calorimeters is summarized in figure 3.12, where the relative energy resolution is shown for the HCAL barrel, HCAL endcap and HCAL forward systems as function of the incident particle energy.

HCAL Barrel

The barrel part of the hadronic calorimeter extends from a radius of 1.77 m, which corresponds to the outer radius of the ECAL barrel up to a radius of 2.95 m, the outer limit being imposed by the inner diameter of the solenoid magnet. It is divided into 36 azimuthal wedges and 16 sectors in η which results in a coverage of $\Delta\eta \times \Delta\phi$ =0.087×0.087 for the individual towers. The HB has an absorber thickness of 5.82 hadronic interaction lengths, λ_I, at $\eta = 0$ which increases as $1/\sin\theta$ up to 10.6 λ_I at the end of the barrel at $|\eta| = 1.3$. Since this is not sufficient to fully contain hadronic showers, additional layers are placed directly outside the solenoid magnet in front of the muon system (the so-called *HCAL outer*). In the central wheel of the return yoke (YB0), two scintillation layers are placed at radii of $R = 3.82$ m and 4.07 m. In the other wheels in the barrel part (YB$\pm$1, $\pm$2) one layer of scintillator is placed. Together with the electromagnetic calorimeter which adds another 1.1 λ_I, the minimal absorber length for hadronic showers is increased to 11.8 λ_I.

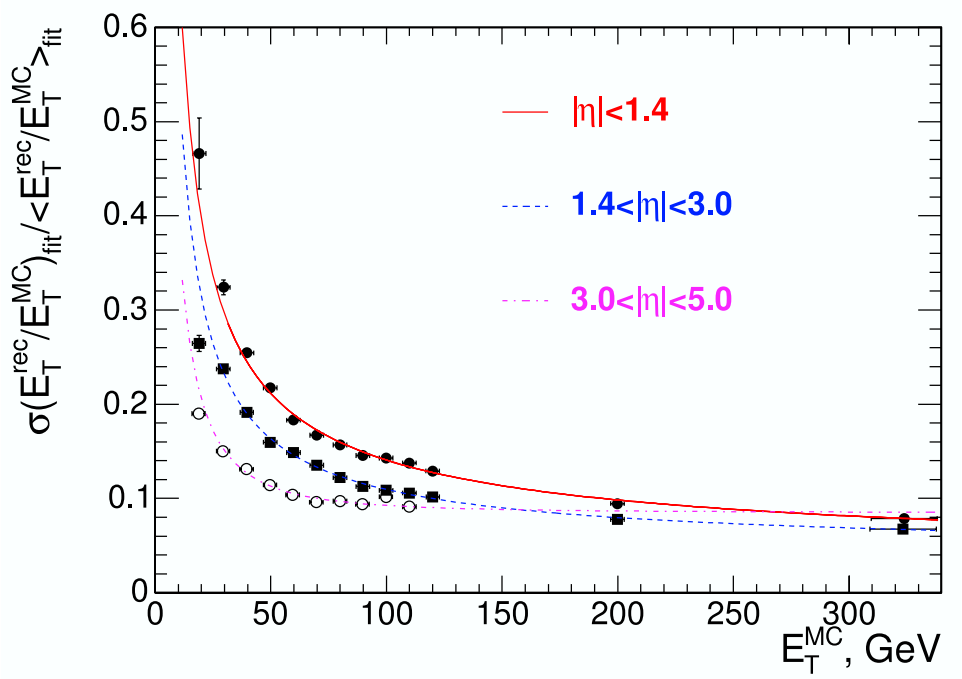

Figure 3.12: Relative transverse energy resolution for the HCAL barrel (red, solid), the HCAL endcaps (blue, dashed) and the HCAL forward (pink, dash-dotted) as function of the transverse energy. From [37].

For all but the two towers closest to the endcaps on either side, the calorimeter towers have a sixteen-fold longitudinal segmentation along R and are each connected to a single readout.

HCAL Endcaps

The two HCAL endcaps which are attached to the first endcap wheel of the return yoke cover the pseudorapidity region $1.3 < |\eta| < 3.0$. Together with the ECAL endcaps, the absorber thickness of the endcaps is about 10 λ_I. The calorimeters are divided into 12–17 longitudinal segments along z, depending on their position in η. Nine towers have two separate readouts to cope with the higher rates compared to the HCAL barrel. The three towers closest to the beam pipe have three separate readouts. The granularity of the endcaps is $\Delta\eta \times \Delta\phi = 0.087 \times 0.087$ for $|\eta| < 1.6$ and $\Delta\eta \times \Delta\phi = 0.17 \times 0.17$ for $|\eta| > 1.6$.

A longitudinal view of the tower geometry and readout segmentation in the HCAL barrel, endcap and HCAL outer is depicted in figure 3.13.

HCAL Forward

The forward part of the hadronic calorimeter consists of two separate units which are placed at $|z| = 11.2$ m from the interaction point. They cover the pseudorapidity $3.0 < |\eta| < 5.0$. To be able to withstand the extraordinarily high radiation doses of 10 MGy after ten years of running, the calorimeter uses steel absorbers with quartz-fibers as scintillator material. The

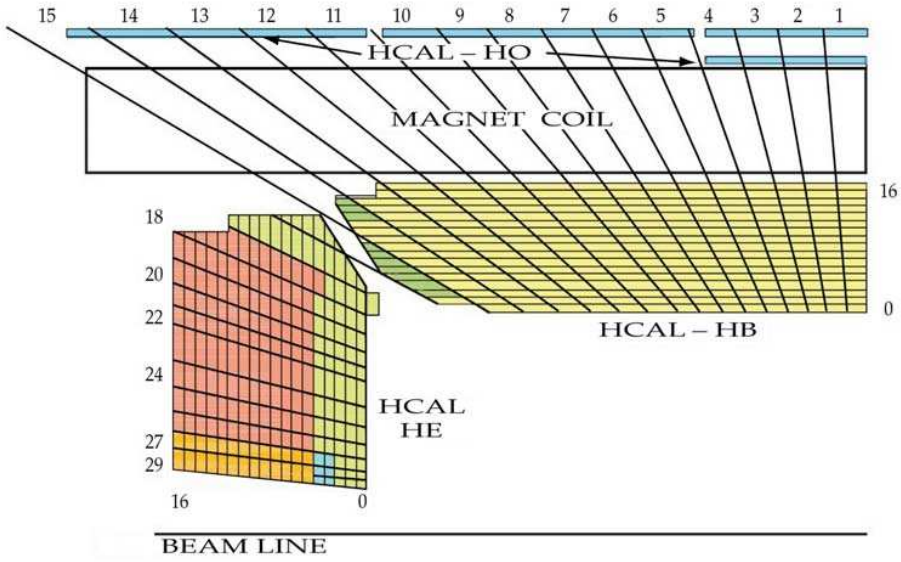

Figure 3.13: The HCAL tower segmentation in the rz plane for one-fourth of the HB, HO, and HE detectors. The shading represents the optical grouping of scintillator layers into different longitudinal readouts. From [37].

fibers are expected to lose about 50% of their transmitivity over the projected 10 years of running. To enable a separation between electromagnetic and pure hadronic showers, 50% of the fibers start with an offset of 22 cm from the front of the calorimeter, thereby enabling an effective longitudinal sampling. The calorimeters have a segmentation of $\Delta\eta \sim 0.175$ and $\Delta\phi = 10°$.

3.3.3 Forward Detectors

In addition to the calorimetry systems described above CMS is equipped with two more systems to increase the hermiticity. The CASTOR[6] calorimeters are placed at a distance of 14.38 m from the interaction point close to the beam pipe. It is a quartz-tungsten sampling calorimeter using similar technology as the HCAL forward detectors. It covers the pseudorapidity region $5.2 < |\eta| < 6.6$ thereby enabling measurements of energy flow also at very small scattering angles. The Zero Degree Calorimeter (ZDC) is part of the protection system of the LHC magnets against remnants of proton collisions. It is placed at 140 m from the interaction region in the LHC tunnels and covers the pseudorapidity region $|\eta| \geq 8.3$.

3.3.4 CMS Luminosity System

The CMS luminosity measurement relies on several independent methods for the determination of the instantaneous and integrated luminosity.

[6] **C**entauro **A**nd **ST**range **O**bject **R**esearch

Online

There are two systems which are foreseen to contribute to the *online luminosity measurement*: The HCAL forward and the Pixel Luminosity Telescope (PLT). The HCAL forward has been described above. Two methods will be used to determine the instantaneous luminosity with the HF:

zero-counting: The number of channels which do not have a signal for a given event gives a good estimate of the number of simultaneous collisions in an event and thereby for the luminosity.

$\overline{\mathbf{E_T}}$: The mean transverse energy per tower is correlated with the luminosity giving a second, independent measurement of the luminosity.

The PLT consists of eight independent telescope structures with three layers each. The layers are made of diamond sensors which are read out with a standard readout chip from the CMS pixel detector. The PLT is used to determine the bunch-to-bunch relative luminosity and the position of the interaction point centroid. The luminosity is estimated by counting the number of particles which cross the telescope during a bunch crossing. For this, a threefold coincidence is required among the planes of each telescope. Together with a precise absolute measurement of the total cross section, the information from the PLT can also be used for a determination of the integrated luminosity.

Offline

Two different approaches are foreseen as offline handles on the luminosity. The Totem experiment [37, ch.7] will measure the total proton-proton cross section during the low luminosity phase of the LHC. The measurement relies on the optical theorem and hence is independent of the luminosity itself. The knowledge about the total cross section enables the determination of the luminosity via other means, e.g. the PLT measurement described above. At higher luminosity the production and decay of W and Z bosons will be used as *standard candle* processes. These can provide a measurement of the luminosity in the order of a few percent. For this, uncertainties on the proton PDFs and the understanding of the detector have to be under control.

3.4 Solenoid Magnet

The superconducting solenoid magnet [43] is the central piece of CMS. It has dimensions of $13{\times}6$ m^2 and is designed to generate a 4 T magnetic field parallel to the beam line. The operating magnetic field will be 3.8 T. Despite its large dimensions, the coil is 'thin' in the sense that the ratio $\Delta R/R$ is only about 0.1. The cold mass of the solenoid is 220 tons. At nominal field, the stored energy is 2.6 GJ; to reach this, a current of 19.14 kA is needed. The coil is made of NbTi which is cooled to 4.6 K using liquid helium. During the cool-down, the coil shrinks about 50 mm in the z- and about 30 mm in the r direction. A drawing of the solenoid is shown in figure 3.14. To return the magnetic field of the coil, a huge return yoke is used. This consists of eleven large parts, 5 in the barrel and 2 times 3 in the endcaps. The yoke barrel (YB) weighs 6,000 tons, the endcaps weigh 2,000 tons each. With a total weight of about 10,000 tons the yoke makes up about 80% of the total weight of the CMS experiment.

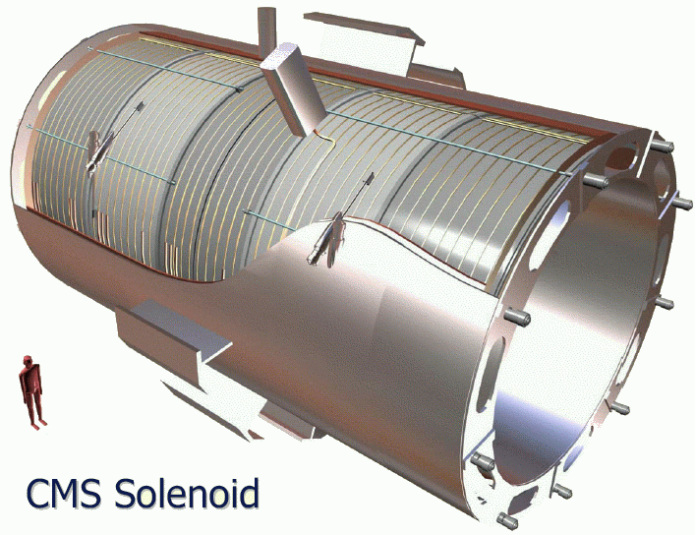

Figure 3.14: Drawing of the CMS solenoid coil.

The magnet has been brought to the nominal magnetic field of 4 T for the first time during the MTCC [33] of CMS.

3.5 Muon System

The CMS muon system [44] consists of three independent subsystems which all are embedded into the return-yoke of the solenoid magnet. Due to the large magnetic field of the solenoid, the magnetic field completely saturates the return yoke with a field of about 2 T and opposite direction with respect to the central solenoid field. This enables a precise measurement of charged particles traversing the muon system. In the barrel part ($|\eta| \lesssim 1.2$), Drift Tubes (DT) are used for the muon detection. In the endcaps, starting at $|\eta| \sim 1$, Cathode Strip Chambers (CSC) are used which are better suited for the operation at higher rates. Complementary to the two systems, Resistive Plate Chambers (RPC) are used in the pseudorapidity region $|\eta| < 1.6$. In total, the muon system has about 1 million electronic channels and covers an area of approximately 25,000 m^2. A schematic layout of the whole CMS muon system with the individual subsystems labeled is shown in figure 3.15. While the yoke provides a large source of multiple scattering which makes it difficult or impossible to detect muons below a certain momentum threshold, hadronic punch-through is negligible. In front of the first muon stations a total of 16 interaction length of material is located, increasing to up to 25 interaction length for the outer layers. The expected performance of the CMS muon system for two regions of pseudorapidity in stand-alone mode and in combination with the inner tracking system is displayed in figure 3.16.

3.5.1 Drift Tubes

The drift tube system is located in the barrel region of CMS, inside and around the 5 barrel pieces of the return yoke. Each yoke part contains four layers of drift tubes. The drift tubes

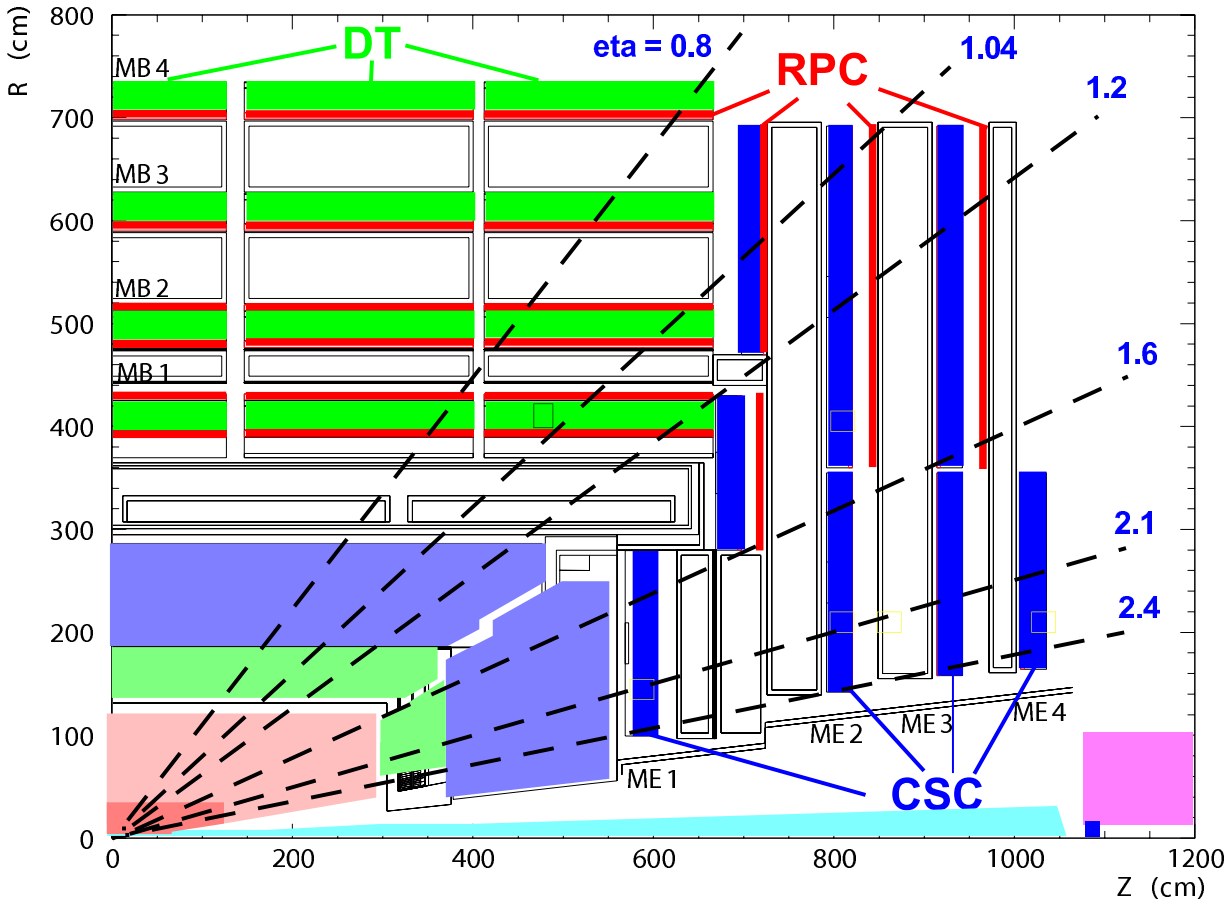

Figure 3.15: Layout of the CMS muon system in the start-up configuration.

have a diameter of 2.1 cm and a length of 2.4 m. The maximum drift time inside a tube is 380 ns. The gas inside the tubes is a mixture of 15 % Argon and 85 % CO_2. The single point spatial resolution is about 200 μm, a whole layer of drift tubes reaches a resolution of about 100 μm and a pointing precision of about 1 mrad.

3.5.2 Cathode Strip Chambers

The cathode strip chambers of CMS are located in the endcap part. The chambers have a trapezoidal shape and cover a certain wedge in $r\phi$. Each chamber consists of seven cathode plates which are interleaved with six anode wire planes. The chambers cover the whole polar angle with small overlaps among neighboring chambers and the azimuthal angle down to 10° or $|\eta| < 2.4$. The CSCs also provide a very robust and efficient muon trigger at the first level with very high muon finding effiency in addition to an unambiguous bunch crossing identification. A total of 468 CSCs are used. The resolution of the CSC system is about 200 μm in spatial resolution and 10 mrad in the ϕ direction.

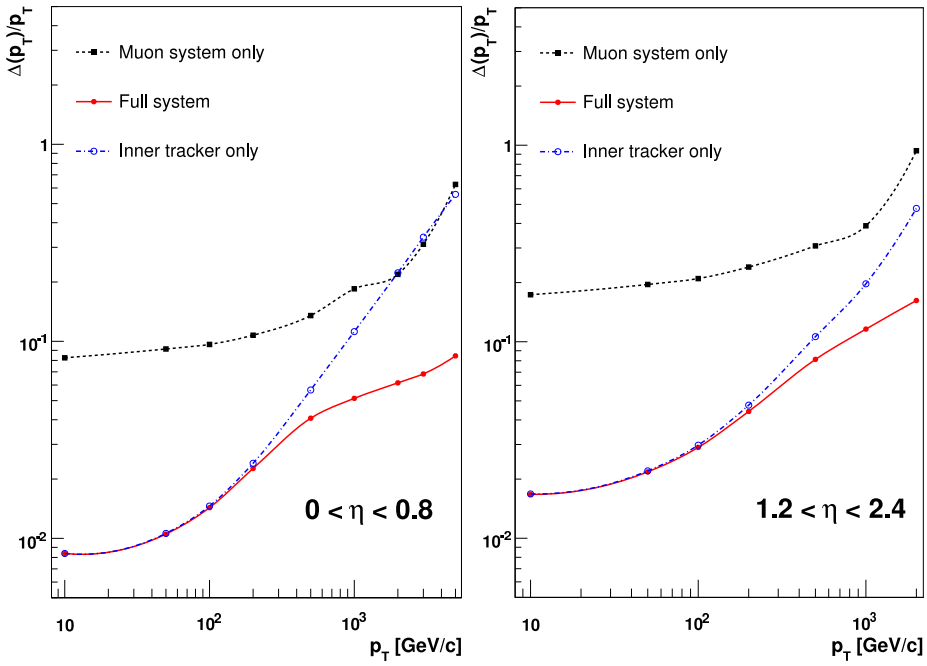

(a) (b)

Figure 3.16: The muon momentum resolution as a function of the momentum (p_T) using the muon system only, the inner tracking only, and a combination of both. (a) $|\eta| < 0.8$, (b) $1.2 < |\eta| < 2.4$. From [37].

3.5.3 Resistive Plate Chambers

Resistive plate chambers are used as redundant measurements for intermediate pseudorapidities. They provide very fast measurements and good trigger performance, but only rather coarse position and hence momentum measurements. The nominal CMS design foresees the usage of RPCs down to pseudorapidities of 2.1. The initial phase, however, will use a reduced setup with RPC coverage only up to $|\eta|$ of 1.6.

3.6 Trigger

In contrast to most other HEP collider experiments, the CMS trigger system consists of only two independent trigger levels which are used to reduce the input data rate of 40 MHz down to a level of about 100 Hz which can be written to disc. The layout of the CMS trigger system is depicted in figure 3.17.

3.6.1 First Level Trigger

In the First Level Trigger (L1), only calorimeter and muon system information are taken into account. The tracker does not take part in the decision since unpacking and track finding would exceed the time limit for the L1 decision. The first level trigger is a pure hardware

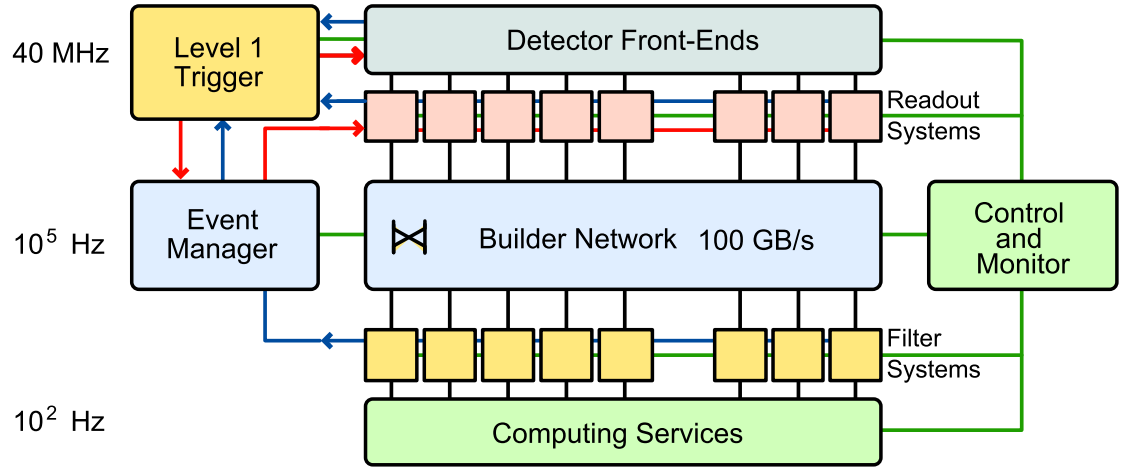

Figure 3.17: Architecture of the CMS trigger and data acquisition system [45].

trigger based on field-programmable gate arrays (FPGAs) where possible to retain flexibility, and on application-specific integrated circuits (ASICs) otherwise. Some parts of the L1 are located directly on the respective detector parts while the global L1 is located in the service cavern USC. The L1 is based on the concept of *Regions of Interest*. First, a local trigger (also called *Trigger Primitive Generator, TPG*) generates possible candidates for the global L1. This is done by summing energies in certain configurations of HCAL and ECAL trigger towers and by reconstructing hits in the muon system. In the regional trigger stage, TPG objects are combined to generate more refined L1 objects. Here, simple track reconstruction is performed in the muon system and certain isolation criteria are applied in the calorimeter. A simple τ-trigger looks for isolated tracks in the calorimeter which could hint to one prong τ-decays. e/γ candidates are identified by looking for certain shower profiles in the ECAL, also accounting for possible bremsstrahlung and shower spread in the magnetic field. The objects of the regional L1 are forwarded to the global L1, which is located in the service cavern about 90 m from the experiment. There it is decided whether an event fulfills a given single trigger or a combination of certain triggers to be further analyzed by the HLT. The latency between a bunch crossing and an L1 accept signal is 3.2 μs.

3.6.2 High Level Trigger/ Switch Network / Event Builder

The most important part for the CMS high level trigger is a high-speed switch network which is capable to gather and distribute the information from the various subsystems to combine all information of one event which is then processed by a single CPU. The switching network has to be run at a rate of about 100 Gb/s. About 1000 local pipelines are needed to store the data at the detector to wait for a L1 accept signal. These have to be connected to $\mathcal{O}(1000)$ CPU cores which are needed for the processing of the output of the L1 in order to reduce the rate to about 100 Hz. The switch network therefore has to provide a 1000×1000 fabric to enable all possible interconnections. All subsystems including the tracker participate in the trigger decision. The high level trigger runs a speed-optimized version of the offline reconstruction software. For the tracker, the concept of *regional unpacking* is utilized, i.e.

only those regions of the tracker are unpacked and reconstructed which are in the vicinity of an L1 object from the calorimeters or the muon system. Only after a HLT accept signal is sent, the full data from the whole experiment is forwarded to the global DAQ and written to disc.

4 Test of Individual Modules – Testbeam Analysis of Irradiated Modules

As described above, the modules of the CMS silicon tracker will be exposed to a harsh radiation environment. In this chapter results from testbeam measurements performed on irradiated modules of the CMS silicon tracker will be described. The modules were irradiated using 26 MeV protons from the secondary beam of the cyclotron at the Forschungszentrum (FZK) in Karlsruhe, Germany, up to the fluences which are expected over the lifetime of the experiment. Several parameters are investigated, notably the signal-to-noise ratio, the spatial resolution as well as cross-talk and charge-sharing. The testbeam measurements were performed from October 26$^{\text{th}}$ to December 5$^{\text{th}}$ 2004 in the testbeam area 22 of the DESY II synchrotron in Hamburg.

4.1 Experimental Setup

4.1.1 Testbeam Area 22 on the DESY II Synchrotron

The testbeam measurements were carried out at the DESY II synchrotron at DESY[1] in Hamburg, Germany. An electron beam in the energy range 1–6 GeV with an energy spread of 5% and a divergence of 2 mrad [46] is available in the testbeam area. A schematic view of the testbeam is shown in figure 4.1. The electrons from the primary beam are directed onto a carbon fiber which acts as a target for the production of high energy photons, which are converted into electron–positron pairs using a metal plate. The resulting beam is then spread in energy using a dipole magnet. Specific energies can afterwards be selected with a collimator.

[1] Deutsches Elektronen Synchroton

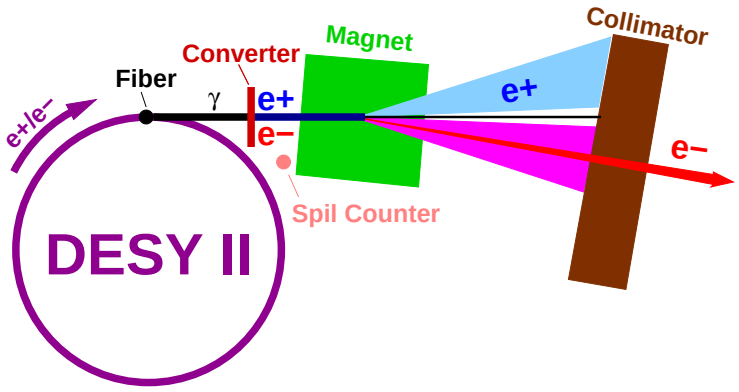

Figure 4.1: Schematic layout of the DESY-22 testbeam.

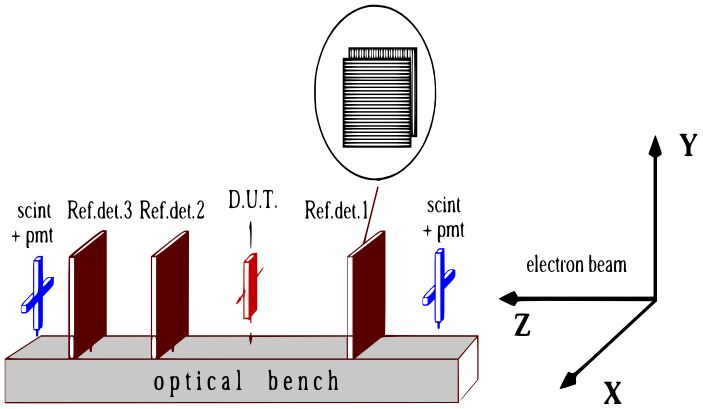

Figure 4.2: Layout of the testbeam setup.

4.1.2 Testbeam Setup

The testbeam setup consists of a precision hodoscope with three layers of silicon microstrip modules, one of which is placed in front and the other two behind the module under investigation (DUT[2]). The distances, as measured from the first hodoscope layer, are 15 cm to the DUT, 27.7 cm to the second hodoscope layer and 39 cm to the third. An individual hodoscope layer consists of two independent strip sensors which are rotated by 90° with respect to each other. With this, the hodoscope provides a precise measurement in both x and y, where the sensitive coordinate of the DUT is denoted as 'x', the coordinate perpendicular to x along the plane spanned by the sensor is called 'y' and the beam direction is called 'z'. The strip pitch of the hodoscope layers is 20 μm, resulting in a single hit resolution of $\mathcal{O}(2\mu\text{m})$. In both front and back, the setup is equipped with scintillation counters that are used for triggering. A sketch of the testbeam layout is shown in figure 4.2. The module itself is housed in a specially manufactured box which is used to simulate the environmental conditions in the CMS tracker. The module is mounted on a copper plate that is connected to a cooling system using a commercial cooling plant to control the temperature. The whole box is mounted on a movable table, allowing both the x- and y-position as well as the rotation angle to be altered. In figure 4.3, two photographs of the testbox and the front-end part of the readout system for the modules are displayed.

4.1.3 Investigated Modules

Different Modules from the Tracker Outer Barrel (TOB) and the Tracker End Cap (TEC) were investigated. Four modules from the outer two layers of the outer barrel (hereafter refered to as OB1 modules) were tested. These modules have 768 strips with a pitch of 122 μm, and are read out by 6 APVchips [40]. The sensors were manufactured by ST Microelectronics. Both irradiated and non-irradiated modules were investigated. The sensors have an active area of 17202.4 mm^2. Three modules from the inner part of the TOB (OB2 modules) were investigated. These modules have the same active area as the OB1 modules but have only 512 strips (and hence only 4 read-out chips) with a strip pitch

[2]Device under test

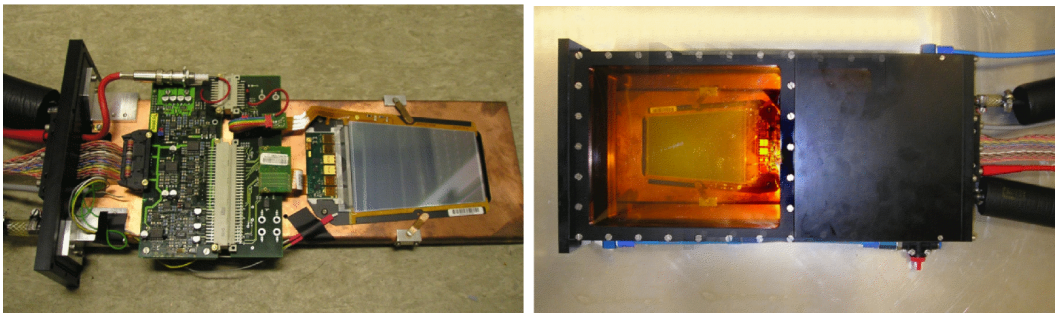

Figure 4.3: Testbox for CMS modules during the Testbeam.

of 183 μm. The modules were irradiated to different fluences, which are also indicated in figure 4.4, where the depletion voltage is shown as a function of the dose. The curve is the expectation of the Hamburg model [30] for the modules under investigation [47]. The fluence of 0.65×10^{14} MeV neutron equivalent/cm^2 corresponds to the expected fluence at a radius of 41 cm after 10 years of LHC running. The fluences of 0.1×10^{14} MeV neutron equivalent/cm^2 and 0.29×10^{14} MeV neutron equivalent/cm^2 are expected to be before and after the type inversion of the modules. After the irradiation, the modules were annealed at a temperature of 60°C for 80 minutes and afterwards stored in a freezer to avoid reverse annealing.

Two modules from the Tracker End Cap (TEC) were also investigated. The modules in questions are wedge-shaped modules from the 5th ring (W5) in the TEC. One module was produced by STM, one by Hamamatsu Photonics. This sensor is of particular interest as the majority of the final tracker modules came from this manufacturer. The TEC modules have an active area of 15635 mm^2 and a pitch that varies from 126 μm at the readout side to 156 μm on the other side. The respective fluences for the irradiated modules are listed in table 4.1. For more details on the various silicon modules used in the CMS Tracker see e.g. [48].

Table 4.1: List of irradiated modules

Module ID	Type	Irradiation ($\times10^{14}$ MeV n eq/cm^2)	pitch (μm)	thickness (μm)	No. strips	Manufacturer
05211	OB1	0.1	122	500	768	STM
05208	OB1	0.29	122	500	768	STM
05207	OB1	0.65	122	500	768	STM
05217	OB2	0.1	183	500	512	STM
05222	OB2	0.28	183	500	512	STM

4.1.4 Measurement Program

An extensive set of runs was taken for each module. For all modules, the readout system was synchronized with respect to the beam-clock. The DESY II synchrotron provides the testbeam area with a clock signal with a frequency of 1 MHz. A custom-built frequency

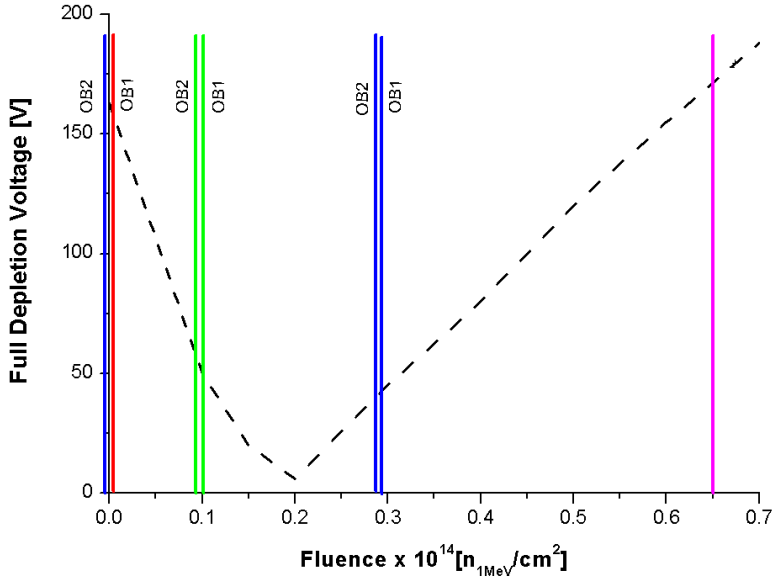

Figure 4.4: Variation of the depletion voltage as a function of irradiation level. The line indicates the expectation of the Hamburg Model [30] for the modules under investigation [47].

Table 4.2: List of non-irradiated modules

Module ID	Type	pitch μm	thickness μm	No. strips	Manufacturer
05275	OB1	122	500	768	STM
05223	OB2	183	500	512	STM
27536	W5	126–156	500	768	Hamamatsu
20532	W5	126–156	500	768	STM

multiplier was used to adjust this frequency to (40 ± 1) MHz to be compliant with the needs of the APV read-out chip. Since the DESY II synchrotron is refilled every 80 ms and the clock restarts with an arbitrary offset, a veto is introduced if the phase shift between the two clocks is larger than 5 ns. A fine latency scan was performed to identify both the correct readout bucket and the best position within this bucket. The measurements listed in table 4.3 were performed on the various modules. The table also shows whether the telescope was active for the respective measurement and which readout mode was used. For most of the measurements, runs were taken in both peak and deconvolution mode[3]. The xy measurement, which will be described in section 4.3.4, was only performed in peak mode. The energy and angular scans were performed with only a coarse scan in peak mode and a finer scan in deconvolution mode. The voltage scan was only performed in deconvolution

[3]For a description of the two readout modes see page 34.

mode whereas for the peak mode only one measurement at 400 V is performed. In the last two cases, deconvolution mode was chosen, because this is the mode which will be used to read the modules out, in order to cope with the increased occupancy caused by high luminosity. The positions 1 to 5 are indicated in figure 4.5.

Table 4.3: Details of the runs taken in the DESY testbeam.

	Events	Telescope	Readout mode	Parameters
Voltage Scan	5000	no	peak	400V
			dec	50V,100V, 200V, 300V, 400V, 550V
Energy Scan	10000	yes	peak	3 GeV, 6 GeV
			dec	1.6 GeV, 3 GeV, 4.6 GeV, 6 GeV
Angle Scan	10000	yes	peak	20°, 40°, 60°
			dec	10°, 20°, 30°, 40°, 50°, 60°, -40°, -60°
Temperature Scan	5000	no	peak	-15°C, -20°C, -10°C
			dec	-15° C, -20°C, -10°C
XY Scan	20000	yes	peak	Pos 1,2,3,4,5
	-50000		dec	

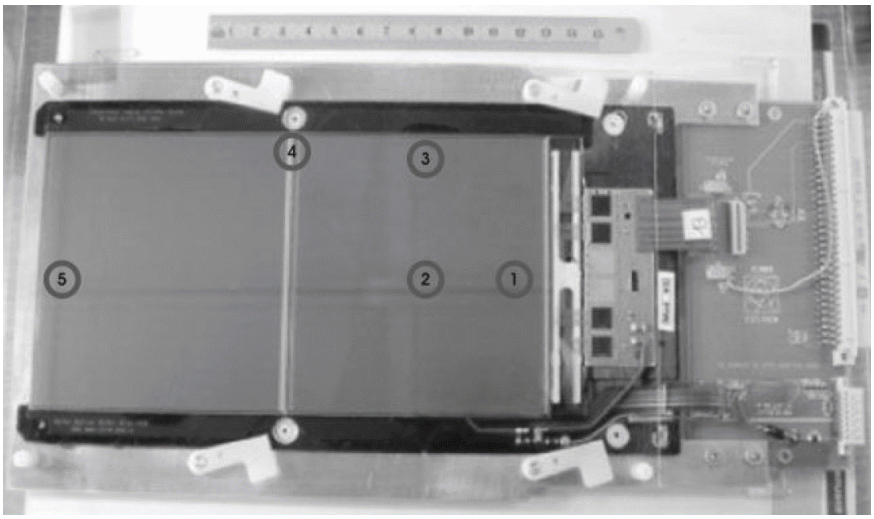

Figure 4.5: Beam positions on the sensor for XY geometry scans.

The nominal environmental conditions for the measurements were chosen to be similar to the operating conditions for the tracker inside the CMS detector. The conditions described below are constant for all runs except for those in which one of the quantities below was deliberately altered. In this case all but the respective parameter are kept constant at their default values:

Temperature: The temperature was kept at -15°C. This is the expected running temperature for the tracker underground

Voltage: The bias voltage was set to 450 V. This is high compared to the depletion voltage for non-irradiated modules, but ensured that all investigated detectors were fully depleted.

Relative Humidity: The box was flushed with nitrogen to keep the relative humidity below the dew point.

Incident angle: The angles of the modules were chosen such that each module was perpendicular to the beam direction in both x and y.

4.1.5 Read-Out

The data from the CMS Module is read out using the raw data as coming from the ARC (APV Readout Controller) system [49]. The data from the module is saved in raw mode and processed offline. A special version of the ARC software is used for this testbeam, which provides the possibility to save a time stamp along with the APV information to enable matching of the datasets from the DUT and the telescope offline. A time stamp is also recorded for the telescope. For the telescope layers, the data is collected in the same way as in previous testbeams. For details see e.g. [50].

4.1.6 Basic Characterization of the Modules

The following analysis steps were performed before any actual measurement was performed on the data. First, the pedestal and raw noise of the individual channels were determined. Afterwards, the common mode was determined and subtracted. Finally, dead and noisy strips were marked.

The pedestals were determined separately for every channel by fitting a Gaussian to the signal distribution summed over a large number of events ($\mathcal{O}(10^4)$). The mean value of the Gaussian is taken as the pedestal for the respective channel and is subtracted from the channel signal. The width of the Gaussian is then the noise for the respective channel. Figure 4.6a shows the distribution for a single channel including the fitted Gaussian. In figure 4.6b, a typical example of a pedestal distribution is shown for a module with 6 APV read-out chips (768 channels). The corresponding noise distribution is displayed in figure 4.6c. The borders between the individual chips are indicated in the distributions. It can be seen that the noise is flat along the module, and edge effects are small. This shows that the modules are well behaved and that the signal-to-noise ratio can be calculated without taking special precautions for e.g. edge channels of the modules under investigation.

The common mode, on the other hand is correlated among groups of strips, as it comes from electronic sources such as power supplies or readout electronics. In this study, the common mode was determined using groups of 32 strips, which were connected to the same analog input of the APV chip. The common mode for a given event was calculated as the truncated mean of the pedestal-subtracted signal of the 32 channels, where the 3 highest and the 3 lowest channels are not included. The common-mode was then subtracted from the pedestal-subtracted data for the corresponding event. The width of the resulting distribution for each individual channel is referred to as the 'common-mode subtracted noise'. Figure 4.7 shows a comparison between the raw noise and the common-mode subtracted noise spectrum of an OB1 module. From the figure it can be seen that the common-mode noise is low and furthermore does not change the noise level or behavior significantly.

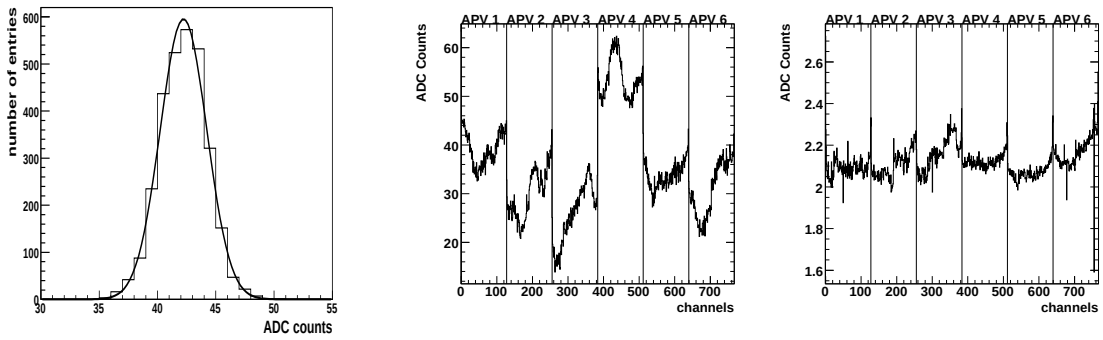

(a) (b) (c)

Figure 4.6: Examples of (a) a single channel distribution fitted with a Gaussian, (b) the pedestal distribution and (c) noise distribution. The examples come from an OB1 module.

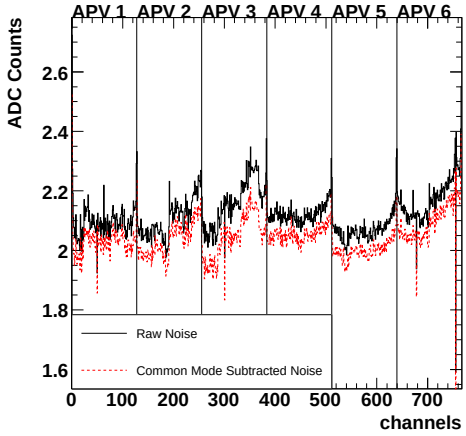

Figure 4.7: Example of the raw noise distribution (solid black line) and common mode subtracted noise distribution (red dashed line) for single strips. This example comes from an OB1 Module.

4.2 Description of Observables

In this section different cluster-finding algorithms for the reconstruction of a hit on the sensor are described. Furthermore, the procedure for the determination of the signal-to-noise ratio and variables for the investigation of cross-talk and charge sharing are outlined.

4.2.1 Cluster Finding

Cluster finding is performed using the so-called *three threshold algorithm*, i.e. using all strips that exceed a certain threshold. A single strip is required to have a signal-to-noise ratio of more than four to be considered as a seed strip. Neighboring strips are added to the cluster

if they have a signal-to-noise ratio of more than three. The whole cluster has to have a signal-to-noise ratio of more than five. The total signal of the cluster is given by:

$$S = \sum_{i|w_\mathrm{i}>w_\mathrm{cut}} w_\mathrm{i}$$

where w_i is the signal from the i-th strip and w_cut is the cut value for that strip, determined using the noise of the strip and the signal-to-noise ratio cut for this strip (seed/neighbor). The noise of a cluster is determined using

$$N = \sqrt{\sum_{i|w_\mathrm{i}>w_\mathrm{cut}} n_i^2}$$

with n_i being the noise of the i-th channel. The noise is calculated using all channels above the thresholds defined above.

4.2.2 Signal-to-Noise Ratio

The signal-to-noise ratio is determined from the ratio of the total cluster signal divided by the total cluster noise. The resulting distribution is fitted with a convolution of a Landau distribution with a Gaussian. The convolution integral is given by

$$f(\Delta, \sigma_L, A, \sigma_G) = \frac{A}{\sqrt{2\pi}\sigma_G} \int_{-\infty}^{\infty} f_L(\Delta', \sigma_L) \exp\left[-\frac{(\Delta - \Delta')^2}{2\sigma_G^2}\right] d\Delta', \tag{4.1}$$

where Δ is the 'most-probable-value' (MPV) of the fit, σ_L is a width parameter of the Landau function, A is the area of the fit function which serves as a normalization constant and σ_G is the width of the Gaussian distribution which accounts for the smearing due to strip noise and other effects[4]. The MPV of the fit gives the signal-to-noise ratio (SNR). An example for a signal-to-noise distribution with the fit function is shown in figure 4.8.

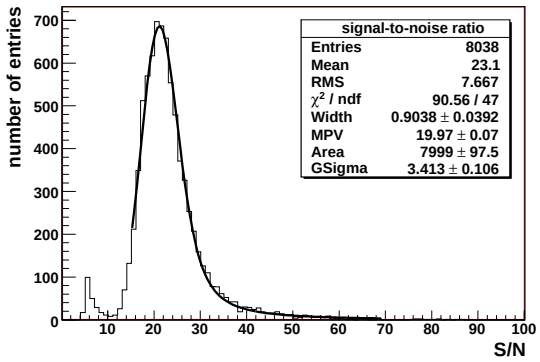

Figure 4.8: Example of a signal-to-noise distribution for clusters fitted with a convolution of a Landau and a Gaussian. MPV denotes the 'most-probable-value' of the distribution.

[4] A software implementation can be found at `http://root.cern.ch/root/html/examples/langaus.C.html`.

4.2.3 Cluster Position

The position of the cluster is reconstructed with different clustering algorithms as described in the following. First, the standard CMS algorithm is described. After this, different algorithms which have certain advantages with respect to the standard algorithm will be described. There performance will be compared in section 4.3.7.

Standard Weighted Algorithm (Center-of-Gravity)

In this algorithm, which is the standard CMS algorithm for reconstruction of hit positions in the strip tracker, the cluster position x_{rec} is calculated via

$$x_{\mathrm{rec}} = \frac{\sum\limits_{i|w_{\mathrm{i}}>w_{\mathrm{cut}}} w_{\mathrm{i}} \cdot i}{\sum\limits_{i|w_{\mathrm{i}}>w_{\mathrm{cut}}} w_{\mathrm{i}}} \cdot p$$

where p is the strip pitch. This cluster algorithm is used for all resolution studies unless stated otherwise.

Double Centroid Algorithm

The double centroid algorithm [51] uses the seed strip of a cluster and its two neighbors for the position reconstruction. With this, possible fluctuations of the noise do not influence the cluster since the neighboring strips are taken into account irrespective of their signal level. In case of the standard center-of-gravitity algorithm described above, strips could fluctuate above the signal-to-noise ratio cut and thus be included in the cluster even in the absence of a physical signal. The position of the cluster for the double centroid algorithm is reconstructed by

$$x_{\mathrm{rec}}^{\mathrm{DC}} = \frac{\mathrm{CG}_l w_{\mathrm{l}}^2 + \mathrm{CG}_r w_{\mathrm{r}}^2}{w_{\mathrm{l}}^2 + w_{\mathrm{r}}^2}$$

with

$$\mathrm{CG}_{l(r)} = \frac{w_{\mathrm{l(r)}} \cdot (i \mp 1) + w_{\mathrm{seed}} \cdot i}{w_{\mathrm{i}\mp 1} + w_{\mathrm{seed}}} p,$$

where i is the strip number for the seed strip and $\mathrm{CG}_{l(r)}$ is the center-of-gravity of the seed strip with the left(right) neighbor and p the strip pitch as above.

Head-Tail Algorithm

The Head-Tail algorithm [51, 52] uses the information from the first (head) and the last (tail) strip of a cluster and the average charge of the strips within the cluster. Therefore the reconstructed position is less dominated by the highest strip in the cluster as is the case for the standard weighted and the double centroid algorithm. In detail, the cluster position is reconstructed by taking:

$$x_{\mathrm{rec}}^{\mathrm{HT}} = \frac{(x_H + x_T) \cdot p}{2} + \frac{w_{\mathrm{H}} + w_{\mathrm{T}}}{2 \cdot w_{\mathrm{AV}}} \cdot p \tag{4.2}$$

where $x_{H(T)}$ is the position of the first(last) strip in the cluster and

$$w_{\mathrm{AV}} = \frac{1}{N} \sum_{i|w_{\mathrm{i}}>w_{\mathrm{cut}}} w_{\mathrm{i}} \tag{4.3}$$

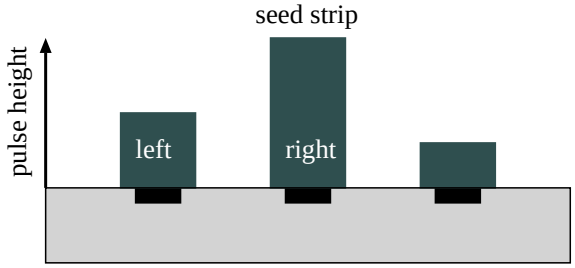

Figure 4.9: Illustration of the definition of η.

is the average charge per strip in the cluster. This algorithm is good at large incident angles (big clusters).

η Algorithm

The η algorithm [53] is also used to reconstruct the position of the incident particle. It makes use of the quantity η, which is defined as

$$\eta = \frac{w_{\text{right}}}{w_{\text{left}} + w_{\text{right}}} \tag{4.4}$$

where $w_{\text{left/right}}$ is the pulse height of the left(right) strip according to the following definition: The system is defined as the maximum strip of the cluster under investigation and the higher of its two neighbors. This is illustrated in figure 4.9. The position is reconstructed as

$$x^{\eta}_{\text{pred}} = p \cdot f(\eta) + x_{\text{left}} \tag{4.5}$$

where p is the readout pitch of the detector and x_{left} is the x coordinate of the left strip according to the definition of η, i.e the seed strip or its left neighbor. The function $f(\eta)$ is defined as:

$$f(\eta) = \frac{\int_0^{\eta} \frac{dN}{d\eta} d\eta'}{\int_0^{1} \frac{dN}{d\eta} d\eta'}. \tag{4.6}$$

The η-distribution is taken from a large dataset while the individual value of $f(\eta)$ is calculated for each cluster. It can be expected that this algorithm is of particular benefit at angles at which the charge is distributed mainly among two strips.

Binary Algorithm

To study the binary resolution of a module, the center position of the maximum strip is taken as the cluster position. For this reconstruction mode, a resolution of pitch/$\sqrt{12}$ is expected. For the binary readout, no beneficial effects of charge sharing are taken into account.

A study of the spatial resolution based on the different cluster algorithms is presented in section 4.3.7.

4.2.4 Charge Sharing

To get a better understanding of the charge collection process and the effects which influence this process, charge sharing and cross-talk are investigated. Charge sharing refers to the situation were charge is physically divided between neighboring strips whereas cross-talk refers to charge being introduced on neighboring strips only by electronic cross-talk, called "capacitive coupling" in the following. The quantities that are sensitive to charge sharing and capacitive coupling are described below:

The η-function The quantity η is also often employed to measure cross-talk and charge sharing. A slight variation of the η quantity, $\eta_{\text{telescope}}$, is also investigated, which differs from the above only in the definition of the left and right strip. In this case the choice is made according to the position predicted by the external track reference, irrespective of the actual pulse height of the strips. The traditional version of η is expected to have a slight bias since the higher of the two neighboring strips is always chosen. This bias will also influence the value measured for the cross-talk. Both definitions have the disadvantage that possible asymmetries in the cross-talk will be averaged and cannot be separately measured.

Symmetric Coupling Another quantity which circumvents the bias of the first η definition is the so-called symmetric charge coupling and is defined as:

$$\zeta = \frac{w_{\text{left}} + w_{\text{right}}}{w_{\text{left}} + w_{\text{seed}} + w_{\text{right}}}. \tag{4.7}$$

Note that here left and right are not the same as in the definition of η but refer to the two neighboring strips of the seed strips.

Average Coupling A third possibility to get a handle on the cross-talk is to take the average coupling of the seed to the two neighbors [54]:

$$\Sigma = \frac{w_{\text{left}} + w_{\text{right}}}{2 \cdot w_{\text{seed}}}. \tag{4.8}$$

This quantity will avoid the bias that can effect the standard η as both neighboring strips are taken into account. Again the definition of the left and right strip are not the same as for η.

A drawback is the fact that differences in the coupling to both neighbors cannot be spotted.

4.2.5 Telescope Analysis

For the telescope, the following steps are performed: First, a cluster finding is performed on the telescope data using a simple center-of-gravity algorithm analog to the one described above. A straight line is constructed from the hits in the first two layers. The third layer is not included in the tracking but a hit in this layer within a reasonable distance from the reconstructed track is required. This procedure was used because it minimized the effect of multiple scattering on the spatial resolution. The procedure for this analysis is in close analogy to other testbeam measurements performed on the setup before [50].

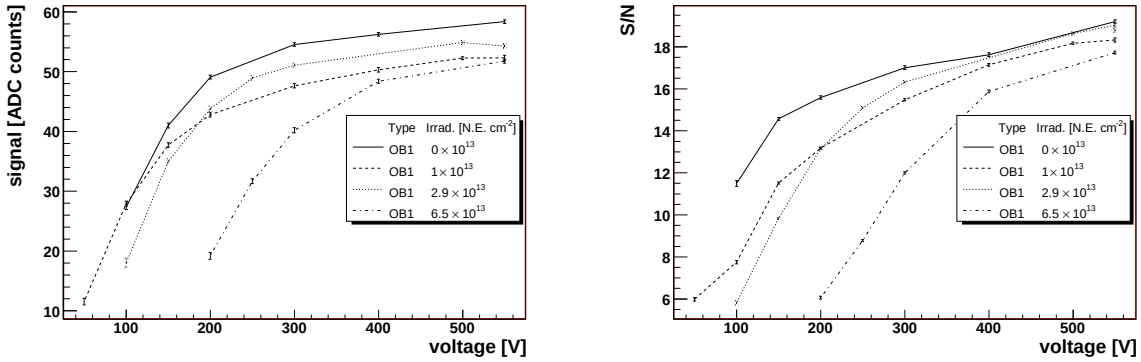

Figure 4.10: Signal (left) and signal-to-noise ratio (right) as function of the bias voltage for OB1 modules. From [55].

4.3 Results

In the following section, the results from the different studies are presented. The signal-to-noise ratio and spatial resolution as well as charge sharing and cross-talk are investigated. After that, the different cluster algorithms are investigated in order to achieve an optimal spatial resolution.

4.3.1 Voltage Scan

The applied bias voltage is expected to affect both the signal and noise of the modules. The signal should increase strongly with voltage up to the depletion voltage, while increasing only slightly above it. Since the depletion voltage and the carrier lifetime are expected to change with increasing irradiation, it is expected that the voltage behavior changes with radiation. This can be seen in figure 4.10, where the signal and SNR are plotted as a function of the bias voltage for different modules. The rise of both the signal and the SNR is similar for all modules, the distribution for the most irradiated module is shifted to higher voltages. This is expected since this module should have a considerably higher depletion voltage after irradiation.

4.3.2 Temperature Scan

The CMS tracker will be operated at an ambient temperature below -10°C. There are a number of reasons for this: Firstly, the leakage current in the silicon bulk material varies according to:

$$I_{\text{leak}} \propto T^2 \cdot \mathrm{e}^{-\frac{E_g}{k_B T}}, \tag{4.9}$$

where E_g is the energy gap between conduction and valence band, k_B is Boltzmanns constant and T is the temperature of the system. The leakage current directly contributes to the noise of the system, as the generated charge is collected by the readout system. Secondly, the noise in the readout electronics will be reduced at lower temperatures, leading to a

significantly better noise behavior. Furthermore, the effect of reverse annealing is reduced at these temperatures [56].

In figure 4.11, the SNR is displayed for several modules from different parts of the detector. It can be seen that while the overall SNR differs for the different modules and geometries, the SNR decreases with increasing temperature for all modules. This is in agreement with the result in figure 4.10.

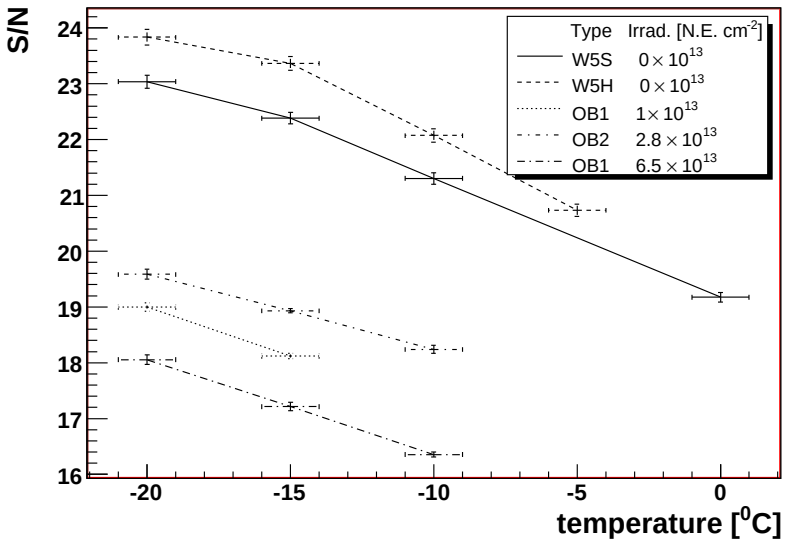

Figure 4.11: Signal-to-noise ratio as a function of the ambient temperature for modules from different parts of the detector. From [55].

Figure 4.11 also shows that the behavior of the W5 STM and W5 Hamamatsu modules is very similar. This result is consistent with what was observed previously [57], and gives confidence that both module types will show a stable performance after irradiation.

4.3.3 Determination of Spatial Resolution

The spatial resolution can be determined by examining the distribution of the residuals $r = x_{\text{meas}} - x_{\text{pred}}$, where x_{meas} is the position on the sensor reconstructed by one of the clustering algorithms defined in section 4.2.1, and x_{pred} is the position on the sensor predicted by the track-fit using information from the telescope layers. An example of a residual distribution can be seen in figure 4.12. When fitted with a Gaussian, the width, $\sigma_{\text{DUT}}^{\text{raw}}$, is a measure of the spatial resolution of the sensor. To get unbiased information about the resolution of the modules, the effects of multiple scattering (MS) must be corrected for, as they can not be neglected at the energies used in this testbeam. The energy dependence of multiple scattering can be parameterized as

$$\Delta\theta_{\text{MS}} \approx \frac{13.6\text{ MeV}}{\beta c|\vec{p}|[\text{GeV/c}]}\sqrt{\frac{\Delta x}{X_0}}\left[1 + 0.038\ln\left(\frac{\Delta x}{X_0}\right)\right] \tag{4.10}$$

where β is the velocity of the particle in units of the speed of light c, $|\vec{p}|$ is the particle momentum and Δx is the thickness of the target material in units of radiation length X_0.

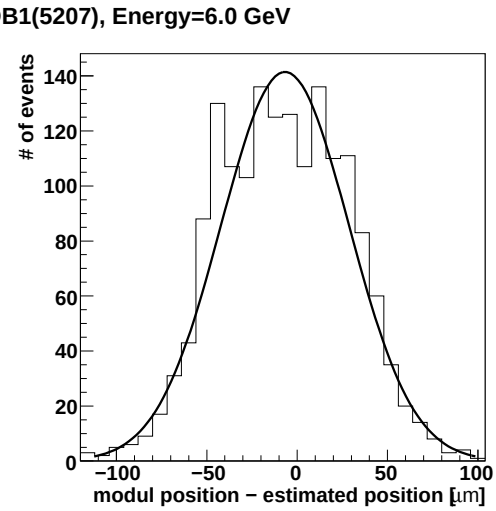

Figure 4.12: Residual distribution for one module at 6 GeV beam energy.

This scattering angle contributes to the measured resolution of the module. It is also important to understand the contribution from the uncertainty in the track prediction due to the finite resolution of the telescope layers. This second term can be written as:

$$V[z] = k_2 \left(\sigma_{\text{eff}}^{\text{tel}}\right)^2 \tag{4.11}$$

where $V[z]$ is the variance of the track prediction at a distance z from the origin. $\sigma_{\text{eff}}^{\text{tel}}$ is the effective resolution of the telescope layers and k_2 is a constant which depends on the distances within the testbeam setup. The measured resolution of the module can therefore be written as:

$$\left(\sigma_{\text{DUT}}^{\text{raw}}\right)^2 = k_1 \cdot \Delta\theta_{\text{MS}}^2 + k_2 \cdot {\sigma_{\text{tel}}^{\text{eff}}}^2 + {\sigma_{\text{DUT}}^{\text{intr}}}^2 \tag{4.12}$$

where k_1 also depends on the geometry of the setup and $\sigma_{\text{DUT}}^{\text{intr}}$ is the intrinsic resolution of the module. The energy dependence of multiple scattering can be exploited to determine its contribution by measuring at different beam energies. Since the other terms are considered constant, the energy dependence can be characterized as

$$\left(\sigma_{\text{DUT}}^{\text{raw}}\right)^2 \propto k_1 \cdot \Delta\theta_{\text{MS}}^2 \left(\frac{1}{E^2}\right) \tag{4.13}$$

This is shown in figure 4.13 where the square of the measured resolution of one of the OB1 modules is shown as a function of E^{-2}. A clear linear dependence can be seen as expected from the multiple scattering contribution. By fitting the measurements with a straight line, the resolution at infinite energy can be determined by taking the intersect of the fit. The remaining contribution to the measured resolution can then be written as

$$\left(\sigma_{\text{DUT}}^{\text{raw}}\right)^2 (E \to \infty) = k_2 \cdot {\sigma_{\text{tel}}^{\text{eff}}}^2 + {\sigma_{\text{DUT}}^{\text{intr}}}^2 \tag{4.14}$$

Since k_2 depends only on the geometry of the setup and the effective resolution from the telescope layers is known, this contribution can also be subtracted, thereby obtaining the intrinsic resolution of the module in question.

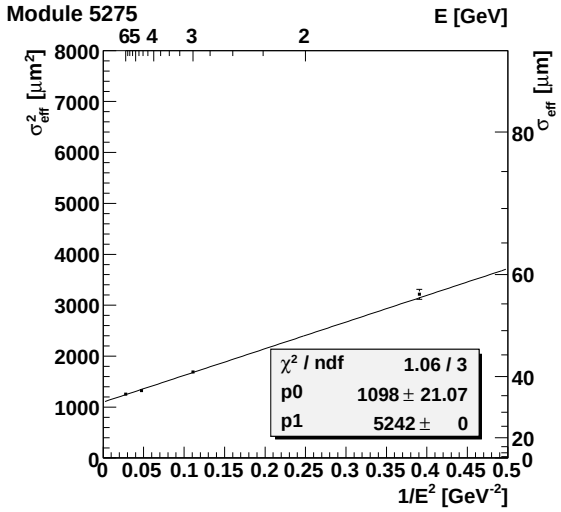

Figure 4.13: Example of a $\frac{1}{E^2}$ fit to extrapolate to infinite energies.

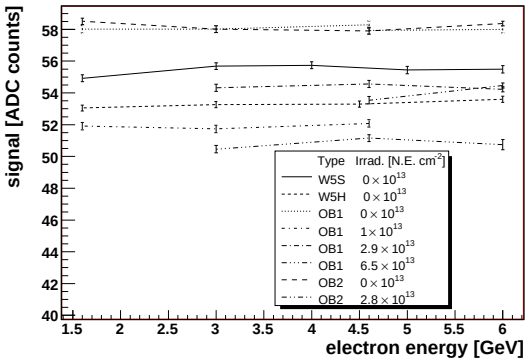

Figure 4.14: Signal level as a function of the energy of the incident electron beam. From [55].

In addition, the signal levels from the sensors were monitored as a function of beam energy to exclude a change in the resolution due to a change in the signal-to-noise ratio, as can be seen in figure 4.14. No change is visible, as expected. In figure 4.15a, the intrinsic resolutions are summarized for the OB1 modules under investigation in which the resolution is shown as a function of the irradiation level. The expected digital resolution of $pitch/\sqrt{12}$ is shown as a solid line to guide the eye. Two main features can be noted: the measured intrinsic resolution is very close to the expected digital one and little influence of the irradiation on the resolution is observed. The first point is expected, as the strip pitch for these sensors is large compared to the expected width of the charge distribution. This limits charge sharing among neighboring strips to a very small region. The effect is further enhanced due to the high value of the chosen bias voltage, which reduces the charge collection times and therefore charge diffusion. The fact that the measured resolution is independent of the amount of irradiation can also be understood since the signals and signal-to-noise ratios measured at different beam energies are almost twice as high as the design specifications.

This ensures that the signal can be reconstructed without ambiguities even for the highest irradiation level. In figure 4.15b the same distribution is shown for the OB2 modules under investigation. For these modules it can also be seen that there is no significant impact from irradiation and the resolution is close to the expected digital one. The results suffer from the fact that some fits to residual distributions have a low probability. In figure 4.16, the spatial resolutions for the two wedge-shaped sensors under investigation are shown. Since the strip pitch of these sensors is not constant along the sensor and the exact y-position of the beam on the sensor is not known, the digital resolution is given as hatched band indicating the range of possible values ($\frac{120\mu\text{m}}{\sqrt{12}}$–$\frac{156\mu\text{m}}{\sqrt{12}}$=34.64$\mu$m– 45.03$\mu$m) that can be expected for these sensors. It can be seen that the measured resolutions lie within this band and are thus compatible to the results obtained before, i.e. a resolution which is close to the expected binary resolution due to the high bias voltage.

4.3.4 XY Scan

The next step was to investigate the SNR and the spatial resolution for different positions on the sensor, as described in section 4.1.4. Apart from this, the conditions are identical to those in the previous section. The XY scan was only performed for some of the OB1 modules. Due to technical difficulties only few runs could be analyzed. All runs for the XY scan were taken in peak mode. In table 4.4 the measured SNR for different positions on the sensor are summarized. No significant differences can be seen for the different positions. The overall values for the two modules differ by about 20% as expected [36].

Table 4.4: Signal to noise ratio for the different points of the XY scan. See figure 4.5 From [55].

type	irradiation	Point on Module				
	$\times 10^{13}$ MeV n eq/cm^2	1	2	3	4	5
OB1	0	30.5	28.8	28.8	28.4	26.4
OB1	6.5	24.4	-	24.0	23.5	22.1

The dependence of the resolution on position is summarized in table 4.5. The observed differences show no systematic behavior in terms of position or irradiation. It can therefore be concluded that the SNR and resolution should remain stable after 10 years on operation, regardless of the position on the sensor.

Table 4.5: Spatial resolutions for the different points of the XY scan. See figure 4.5

type	irradiation	Point on Module				
	$\times 10^{13}$ MeV n eq/cm^2	1	2	3	4	5
OB1	0	-	-	$(33.2 \pm 0.7)\mu$m	$(38 \pm 1.7)\mu$m	$(37 \pm 1.7)\mu$m
OB1	6.5	$(35 \pm 1)\mu$m	-	$(38.9 \pm 0.9)\mu$m	$(32 \pm 1)\mu$m	$(34 \pm 1)\mu$m

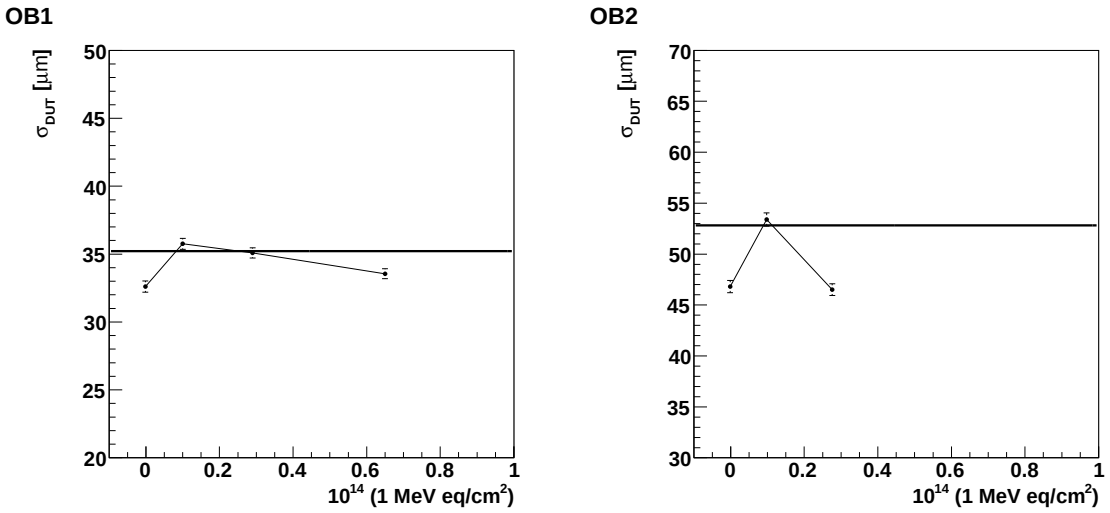

(a) (b)

Figure 4.15: Resolution of OB1 (left) and OB2 modules (right) under investigation as a function of the fluence. The points are connected to guide the eye, the solid line shows the digital resolution of $\frac{\text{pitch}}{\sqrt{12}}$ for the respective module.

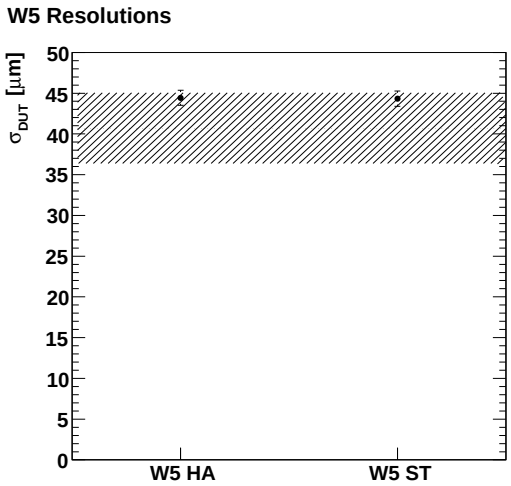

Figure 4.16: Resolution of the W5 Hamamatsu module (left) and the W5 ST module (right). The hatched band indicates the expected binary resolution for the varying pitch of the modules.

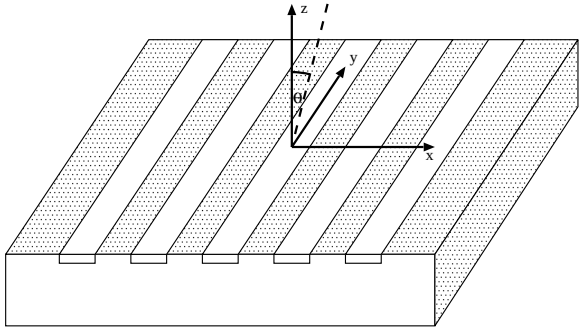

Figure 4.17: Definition of angle θ for angular scans.

4.3.5 Angular Scan

As well as the scans performed with the beam perpendicular to the sensor surface, beam angle scans were made. Several effects can be expected due to geometrical considerations. Firstly, the path length s of the beam particles in the modules increases. This increase can be parameterized as:

$$s(\theta) = \frac{s(0°)}{\cos\theta} \tag{4.15}$$

where $s(0°)$ is the path length through the detector at 0° incident angle and θ is the angle with respect to the sensor surface, as illustrated in figure 4.17. Due to effects which go beyond simple geometric consideration the cluster charge S is not strictly proportional to the path length, and this function does not describe the data well. The modified function

$$S(\theta) = \frac{p_0}{\cos(\theta - p_2)} - p_1 \tag{4.16}$$

is therefore used, where $p_0 - p_1 = S(0°)$ and also a possible asymmetry with respect to zero is allowed (p_2), though it is not expected. A function of the second form is fitted to the data of one of the modules in figure 4.18a. One can see that it describes the data for all but the largest angles. In figure 4.18b the distributions for the other modules are shown. It can be seen that they behave similar to the distribution in figure 4.18a also for the highest irradiation levels.

Also for the spatial resolution, changes are expected for different incident angles. Due to charge sharing, the resolution can be expected to improve. The optimum angle is reached when always exactly two strips are hit. This angle can be calculated as

$$\theta_{\text{opt}} = \arctan\frac{p}{d} \tag{4.17}$$

where p and d are the strip pitch and thickness of the sensor respectively. This situation is illustrated in figure 4.19. Due to different pitches and sensor thicknesses, the optimum angle differs for the different module types. The expected optimum angles are summarized in table 4.6.

In figure 4.20a the spatial resolutions obtained in the angular scans are summarized for three of the four OB1 modules. It can be seen that there is again little influence

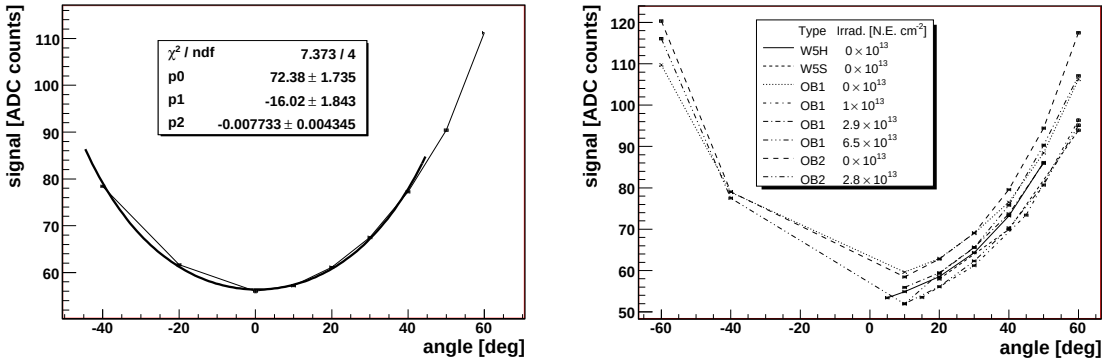

(a) (b)

Figure 4.18: Cluster pulse height of single angular signal distribution with fit (a) and angular distributions for all other modules (b). From [55].

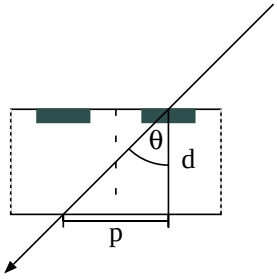

Figure 4.19: Schematic illustration of optimal angle for charge sharing among two neighboring strips.

	OB1	OB2	W5
θ_{opt}	13.7°	20.2°	13°- 18°

Table 4.6: Expected optimum angles for charge sharing for different module types.

of the irradiation. Even at the largest angles, the modules show similar behavior. This shows that effects like a shift of the reconstruction surface within the sensor due to charge trapping are not a large problem. Furthermore, it can be seen that all distributions reach a minimum value at an angle which is fully compatible with the expected optimum angle for this geometry. In figure 4.20b, the equivalent distribution is shown for two of the OB2 modules. It can be seen that also here the best spatial resolution is achieved at an angle which is in agreement with the predicted optimum angle. Runs for other OB2 modules could not be analyzed due to technical problems. Both runs at an incident angle of 20° also had problems which inhibited an analysis of the data.

4.3.6 Charge Sharing/Cross-Talk

To get further insight into the charge collection process at different irradiation levels, the charge sharing and the cross-talk are investigated using the quantities outlined in section 4.2.4. In addition, the charge collection is investigated using information from the telescope.

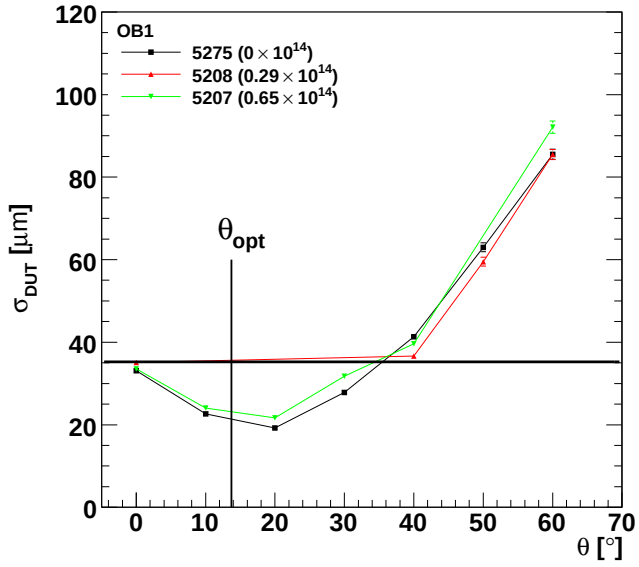

(a)

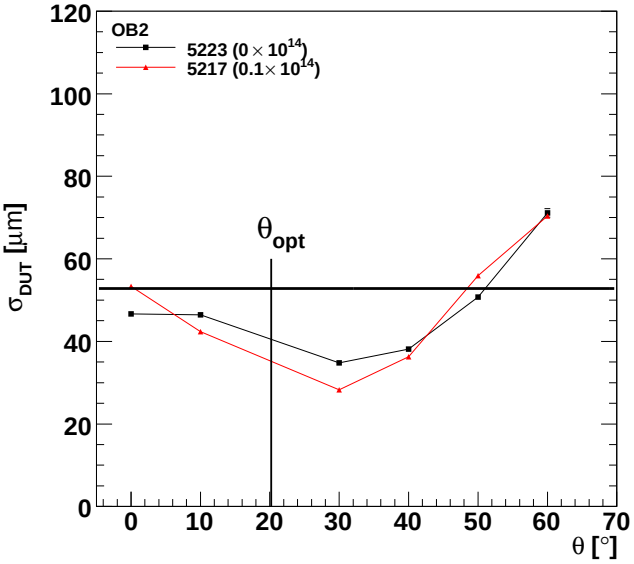

(b)

Figure 4.20: Spatial resolution as a function of the incident angle for different irradiation levels for OB1 modules (a) and two OB2 modules (b).

Determination of Charge Sharing using Telescope Information

To investigate the charge sharing process, the distribution of the charge in clusters is investigated. For this, the charge of the seed and its two neighbors is investigated as function of the reduced hit position x_{red}, which is the difference of the predicted hit position from the center of the seed strip under investigation in units of the strip pitch. In figure 4.21,

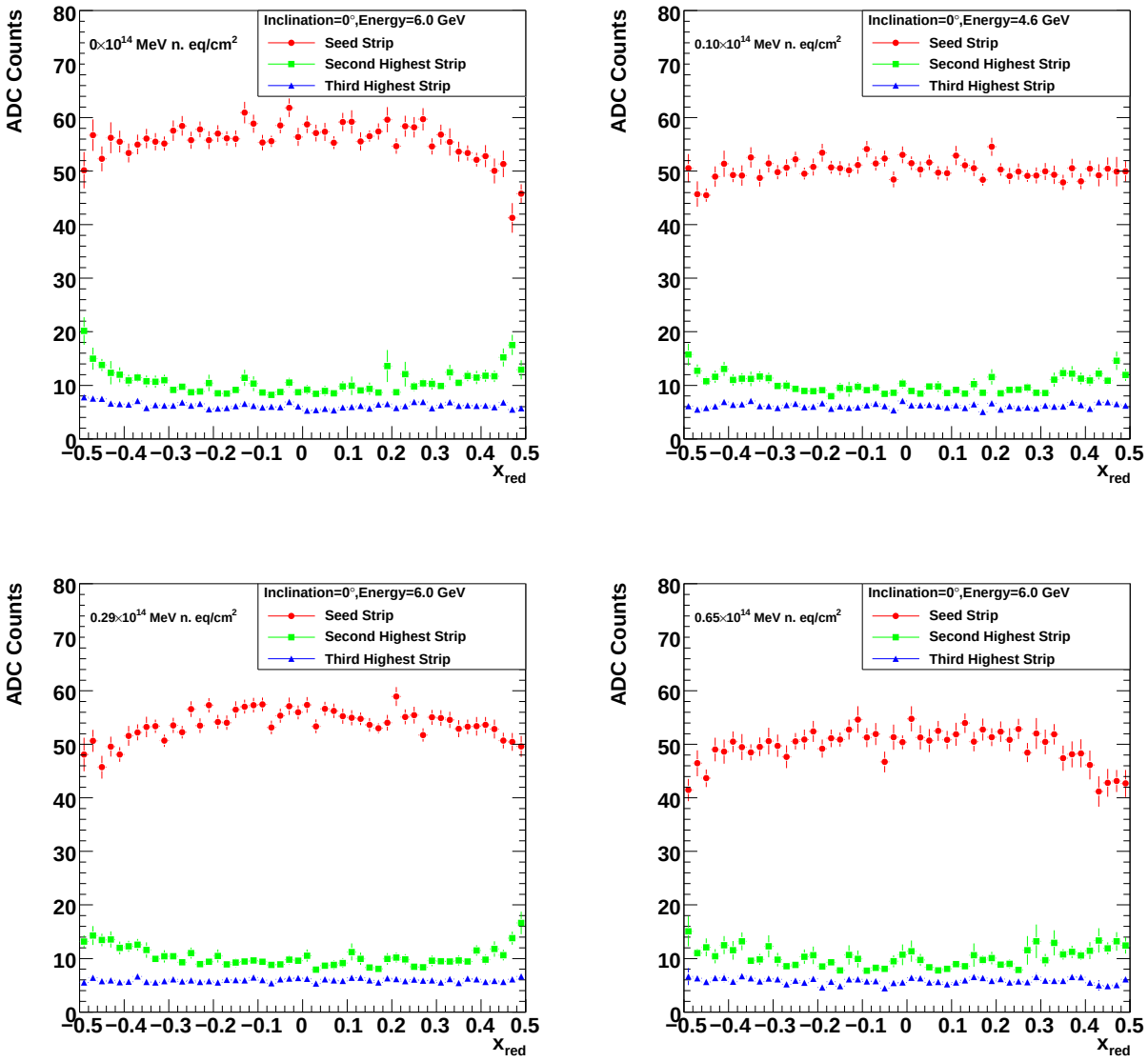

Figure 4.21: Pulse height of the seed strip and the second and third highest strip for the non-irradiated OB1 module (upper left) and with irradiation levels of 0.1×10^{14} MeV neutron equivalent/cm^2 (upper right), 0.29×10^{14} MeV neutron equivalent/cm^2 (lower left) and 0.65×10^{14} MeV neutron equivalent/cm^2 (lower right).

the charge on the three strips is displayed as a function of x_{red} for four different irradiation levels. Here, a value of $x_{\text{red}} = 0$ corresponds to the middle of the seed strip. Little change can be seen as a function of the irradiation. In figure 4.22, the same distributions are shown for the non-irradiated OB1 module for inclination angles from 10° to 60°. It can be seen that there is a clear anti-correlation between the seed strips and the second-highest strip at 10°. This anti-correlation is then observed between the second and third highest strip at an angle of 20°. At larger angles no clear correlation between the strip signals can be observed. This behavior is consistent with the one observed for the spatial resolution where an optimal resolution was observed between 10° and 20° corresponding to the situation where always two strips are hit.

Charge Sharing and Cross-Talk from the η-Function

The η-function can be used to quantify certain aspects of the charge collection process. These can be taken from both definitions of the η-function from section 4.2.4; in the following, though mostly the definition using pointing information from the telescope will be used, as it offers unbiased information.

In figures 4.23 and 4.24 one example for each of the definitions is shown. One can see that the distributions are largely similar which can be understood since in many cases the strips under investigation will be the same. The distributions are shown for an OB1 module for nominal conditions (cf. section 4.1.4). In both distributions, two distinct peaks can be seen at η values of approximately 0.1 and 0.9, respectively. This corresponds to the situation were the charge is collected very asymmetrically on only one of the two strips. In the central η-region ($0.25 < \eta < 0.75$) few events can be seen. These intermediate η values are expected when the charge is distributed quite evenly among the strips. To check this, $\eta_{\text{telescope}}$ is evaluated as a function of the relative predicted position in units of the strip pitch (figure 4.25). Here it can be seen that intermediate η values can be associated with positions in the middle between the two strips ($x_{\text{pred}} = 0.5$). Furthermore it can be seen that charge sharing occurs only in a very narrow region, while for impact positions as close as 20% of the border of a readout strip ($\eta < 0.4$ and $\eta > 0.6$), almost all charge is concentrated on one strip. The value of η in these regions is independent of the predicted position on the strip. Hence, it can be concluded that no charge sharing among the strips is present and the displacement of the peaks from zero and one gives an estimate of the cross-talk to the neighboring strips. The width of the peaks can be associated with the single strip noise.

Figure 4.26 shows an example of a fit to one peak of the η distribution. The mean value of the fit (0.117) gives the average value of the cross-talk to the left and the right strip, respectively. The most-probable value for the seed strip charge for the respective run is about 51 ADC counts as can be seen from figure 4.27. The width of the peak of the η distribution is 0.039. This would correspond to a single strip noise of about 2 ADC counts, given a most probable seed charge of 51 ADC counts, which is in very good agreement with the obtained values (see e.g. figure 4.7).

This situation can be expected to change with the incident angle of the particle. This is shown in figure 4.28 where a profile plot $\eta_{\text{telescope}}$ is shown as a function of x_{pred} for different incident angles. It can be seen that, as the incident angle increases the distributions become more and more flat and already at 40° the deviation from a horizontal line is only very slight. This is due to the fact that the cluster size at this angle is already more than four strips on average as can also be seen from figure 4.29 were the cluster size is shown for the

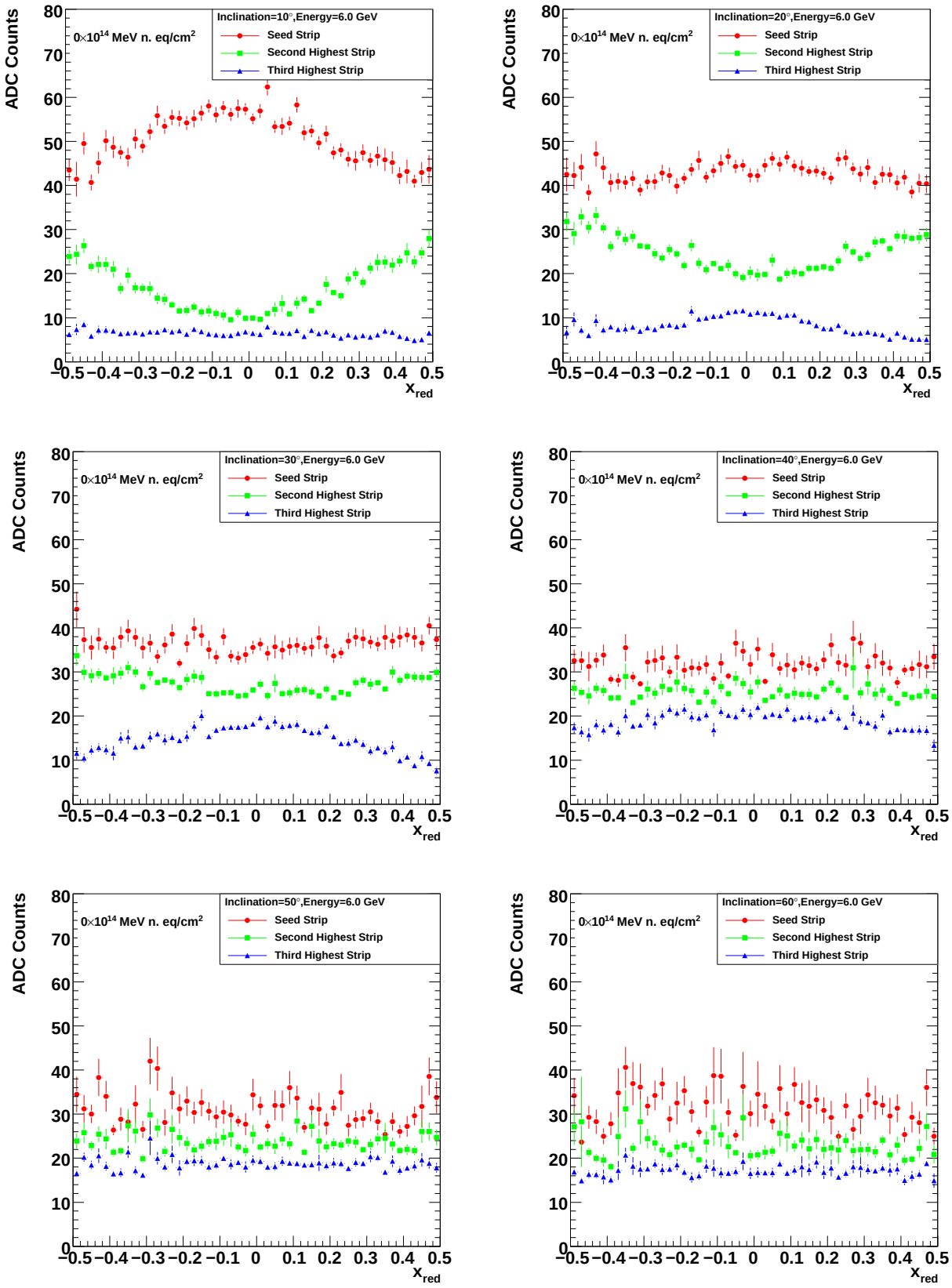

Figure 4.22: Pulse height of the seed strip and the second and third highest strip for the non-irradiated OB1 module for incident angles from 10° to 60° from top left to bottom right.

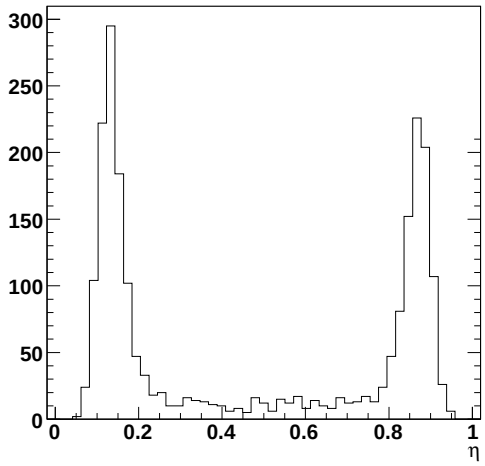

Figure 4.23: η distribution obtained with cluster information only.

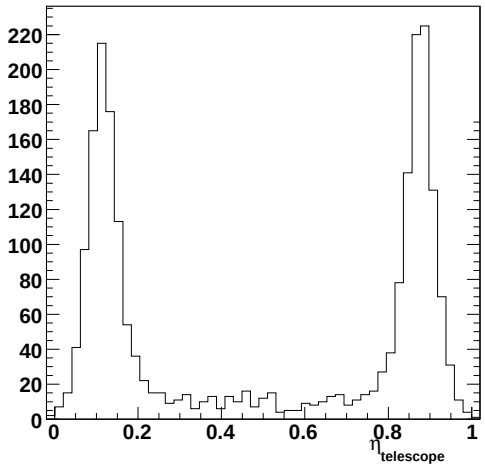

Figure 4.24: η distribution obtained using flagging from the telescope.

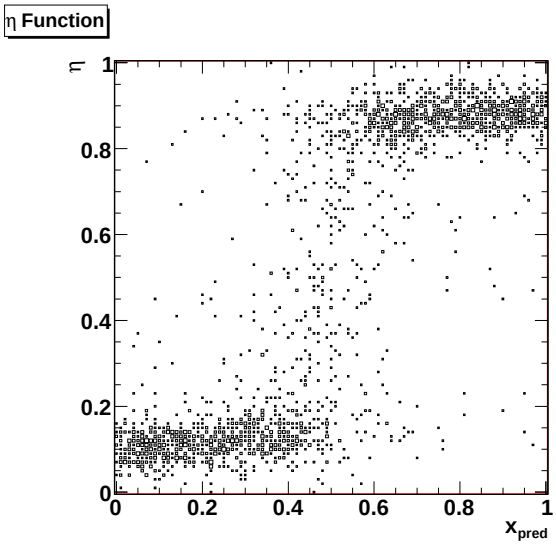

Figure 4.25: $\eta_{\text{telescope}}$ as a function of the predicted hit position.

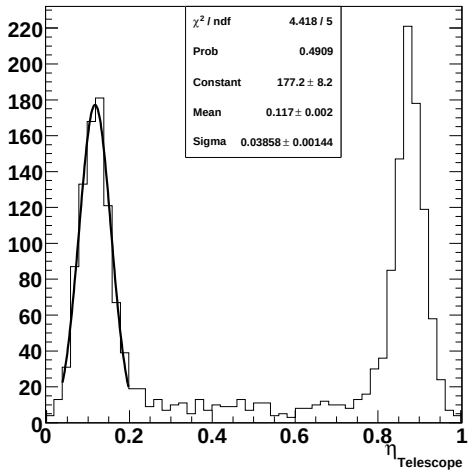

Figure 4.26: η-distribution using flagging from telescope. A Gaussian fit to one peak of the distribution is shown.

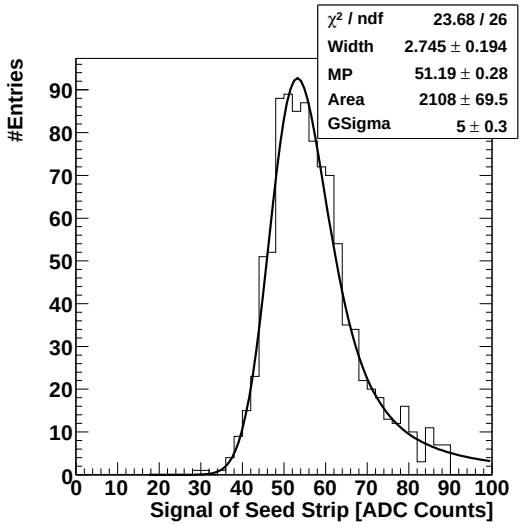

Figure 4.27: Distribution of seed strip charges for cluster under investigation. A Landau-Gaussian fit to the distribution is shown.

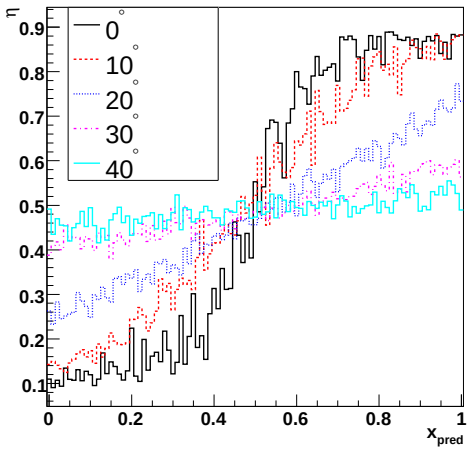

Figure 4.28: Profile distributions of $\eta_{\text{telescope}}$ as a function of the predicted hit position for incident angles of 0° (black), 10° (red), 20° (blue), 30° (violet) and 40° (turquoise).

same angles as before. In this case very little information about the cluster is contained in the two strips under investigation. This is also reflected in the η-function itself which is displayed in figure 4.30 for angles between 10° to 60°. At angles above 40°, the shape of the function hardly changes and there is only a single peak around $\eta = 0.5$, which corresponds to equal charge division among the strips.

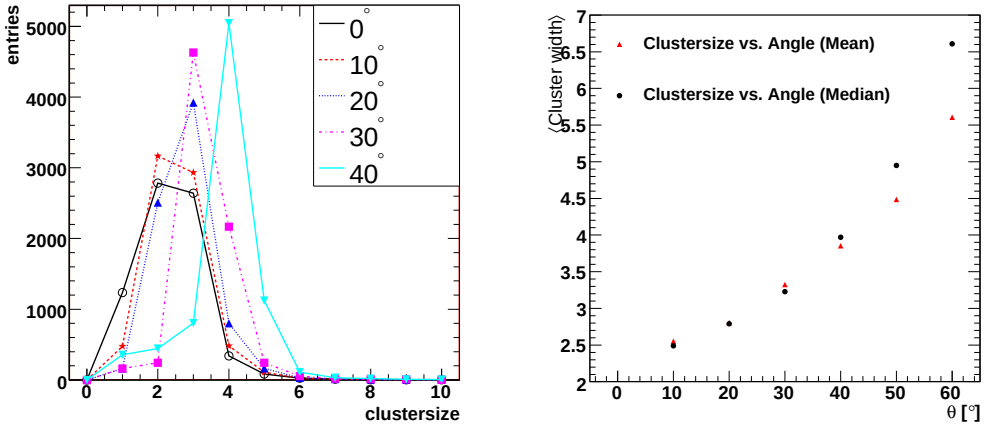

(a) (b)

Figure 4.29: Cluster size for incident angles of 0° (black), 10° (red), 20° (blue), 30° (violet) and 40° (turquoise) (a) and mean and median of cluster size distribution (b).

Direct Measurement of Cross-Talk

With the testbeam setup it is also possible to measure the cross-talk directly. This is especially useful since it enables a comparison between a direct measurement and the indirect measurements which can also be used in data without external track reconstruction. Furthermore, the cross-talk can be measured not only to the immediate neighbor, but also e.g. to the next and second-to-next neighboring strip.

For the direct measurement, events were selected where the hit position was within ±25% of the center of a strip. With this selection it is ensured that charge measured on neighboring strips is induced solely by capacitive coupling since the charge cloud generated by the traversing particle will only be few μm wide, i.e. less than 1/10 of a strip pitch for OB1 modules (pitch 122 μm).

In figure 4.31, the resulting distributions are shown for the non-irradiated OB1 module. In figure 4.31a the cross-talk to the left strip is shown, while 4.31b shows the cross-talk to the right. One can see that while the amount of charge transfered to the individual strips is decreasing rapidly for the second and third neighbor, it is still different from zero. For all modules, these distributions are fitted with Gaussians. The mean values are shown in figure 4.32 where the cross-talk is shown for the different strips for different irradiation levels. It can be seen that the cross-talk is slightly ($\mathcal{O}(1\%)$) asymmetric between the left and the right neighbor. The reason for this is not known, it can however be suspected that this

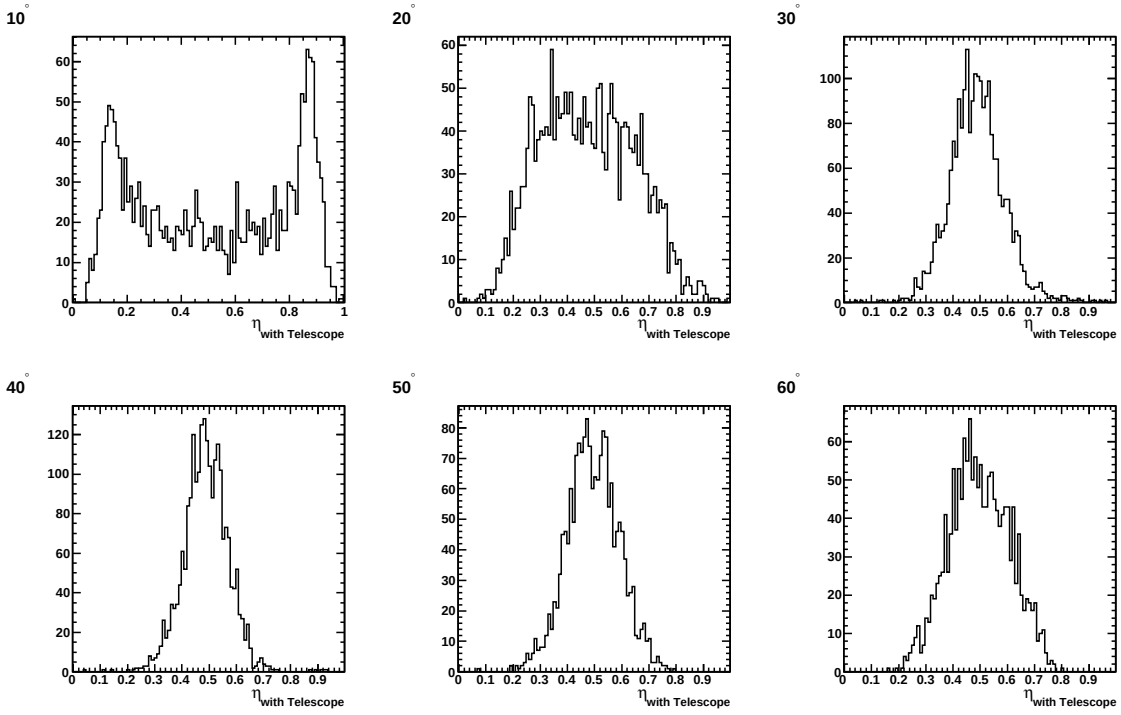

Figure 4.30: η-distribution for incident angles from 10° to 60° from top left to bottom right.

is caused in the readout chip. Furthermore, the figure shows that the amount of cross-talk increases only very slightly with irradiation.

Systematic Study of Cross-Talk Variables

Since a direct measurement of the cross-talk as described above is not easily possible in data, the variables outlined in section 4.2.4 can be used for this, as they rely solely on cluster information. To study the effect of different cross-talk values and possible asymmetries in the cross-talk, the following simple situation is considered. For 0° incident angle, the generated charge is most often collected by a single strip only. In this case, the charge on the neighboring strips is induced solely by cross-talk. The charge distribution can then be modeled as follows. The seed strip has a charge of $w_{\text{seed}}^{\text{raw}}$ generated by the collection of the charge. This is then reduced by the capacitive coupling to the neighboring strips. Assuming a coupling of $0 < k < 0.5$ to both neighboring strips, the charge on the three strips under consideration can be written as

$$w_{\text{seed}} = (1 - 2k) w_{\text{seed}}^{\text{raw}} \tag{4.18}$$

$$w_{\text{left}} = w_{\text{right}} = k w_{\text{seed}}^{\text{raw}}. \tag{4.19}$$

The cross-talk quantities can be calculated from this as

$$\eta = \frac{w_{\text{right}}}{w_{\text{left}} + w_{\text{right}}} = \frac{k}{1 - 2k + k} = \frac{k}{1 - k} \tag{4.20}$$

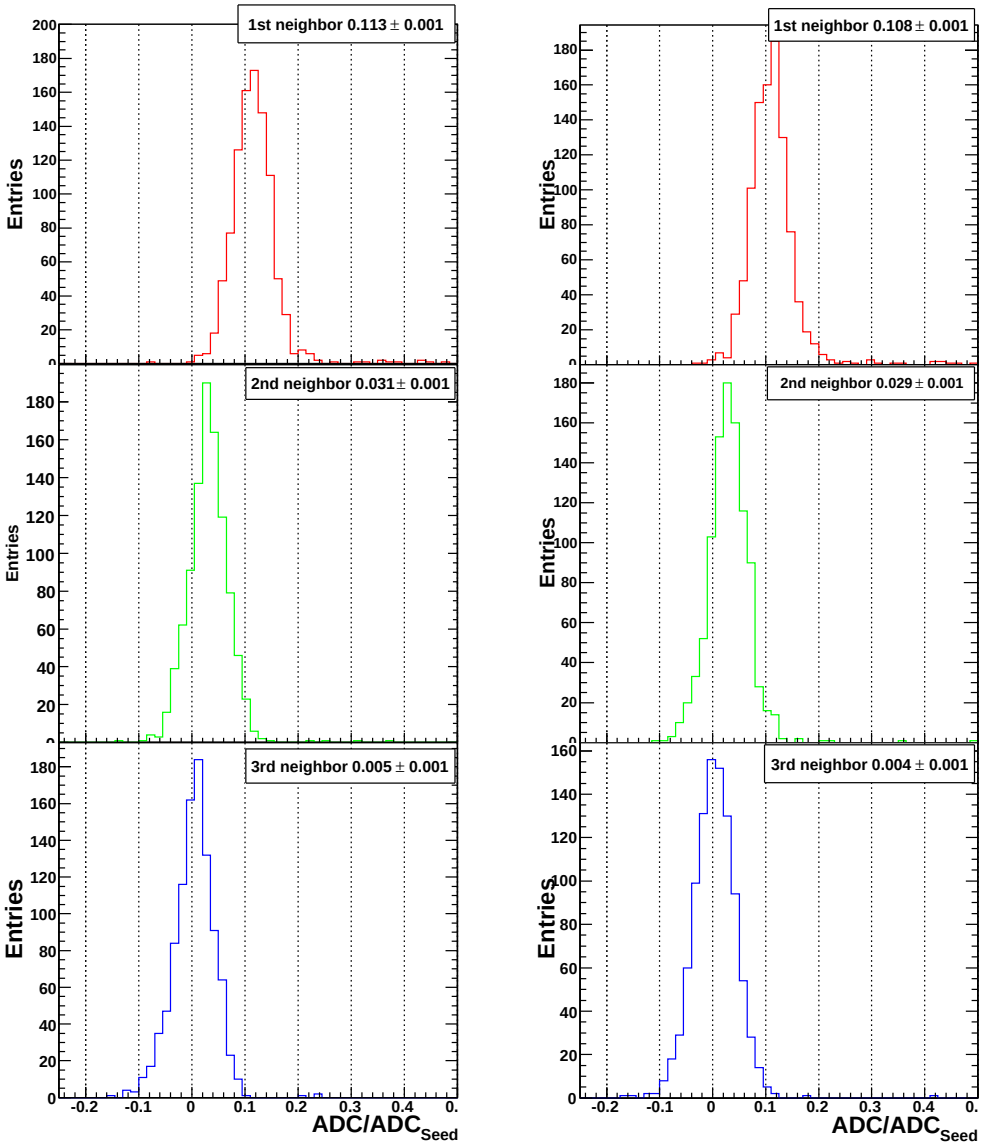

(a) left neighboring strips

(b) right neighboring strips

Figure 4.31: Strip charge in units of the charge of the hit strip for three strips on the left (a) and on the right (b) side of the seed strip.

where for simplicity only one of the two possible configurations is indicated and

$$\zeta = \frac{w_{\text{left}} + w_{\text{right}}}{w_{\text{left}} + w_{\text{seed}} + w_{\text{right}}} = \frac{2k}{1} = 2k \text{ and} \tag{4.21}$$

$$\Sigma = \frac{w_{\text{left}} + w_{\text{right}}}{2 \cdot w_{\text{seed}}} = \frac{2 \cdot k}{2(1-2K)}. \tag{4.22}$$

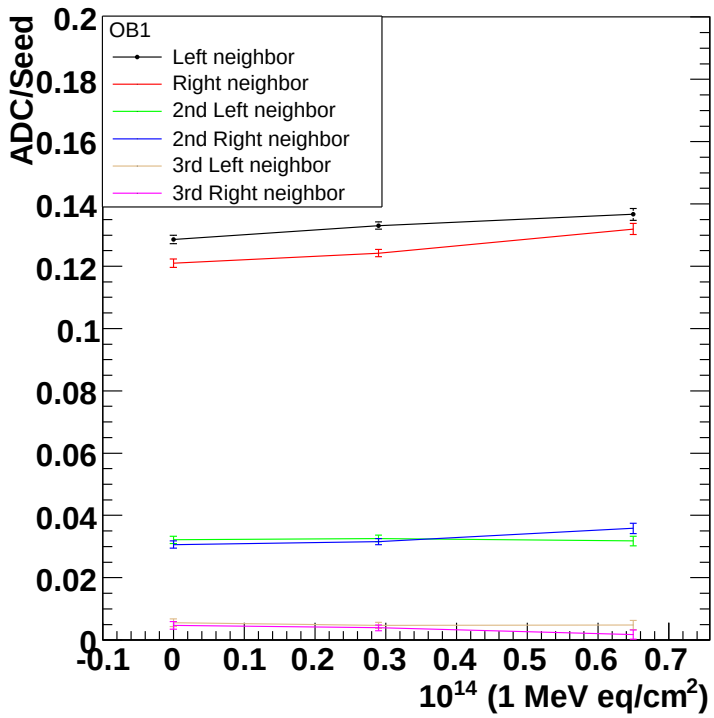

Figure 4.32: Cross-Talk for OB1 modules as a function of the irradiation level for three strips left and right of the hit strip.

Note that again for ζ and Σ the definition of the left and right strip is different from the one used for η. One can easily see that by dividing ζ by 2 one can reproduce the initially modeled cross-talk.

To account for a possible asymmetry in the cross-talk to the neighboring strips, the following modification can be made: If the cross-talk to one side (here, the right side is arbitrarily chosen) is larger by some small amount $a < k$, the charge distributions change as follows:

$$w_{\text{seed}} = (1 - 2k - a)w_{\text{seed}}^{\text{raw}} \tag{4.23}$$
$$w_{\text{right}} = (k + a)w_{\text{seed}}^{\text{raw}} \tag{4.24}$$
$$w_{\text{left}} = kw_{\text{seed}}^{\text{raw}}. \tag{4.25}$$

This changes the cross-talk variables to

$$\eta = \frac{w_{\text{right}}}{w_{\text{left}} + w_{\text{right}}} = \frac{k+a}{1-2k-a+(k+a)} = \frac{k+a}{1-k} \tag{4.26}$$

$$\zeta = \frac{w_{\text{left}} + w_{\text{right}}}{w_{\text{left}} + w_{\text{seed}} + w_{\text{right}}} = \frac{2k+a}{1} = 2k+a \tag{4.27}$$

$$\Sigma = \frac{w_{\text{left}} + w_{\text{right}}}{2 \cdot w_{\text{seed}}} = \frac{2k+a}{2(1-2k-a)}. \tag{4.28}$$

One can see that in this case ζ (again divided by 2) gives the average of the two cross-talk values. The resulting cross-talk values from the variables are shown in figure 4.33 as a function of the input cross-talk for three different asymmetries a. It can be seen that, as described above, ζ reproduces the input cross-talk for $a = 0.0$ and is offset by $\frac{a}{2}$ for values different from zero. The η quantity on the other hand departs from the input cross-talk as $\frac{k}{1-k}$. This simple model does of course not hold for more complicated cross-talk scenarios but gives a rough estimate of possible intrinsic biases.

Correction for Cross-Talk

If the magnitude of the cross-talk is correctly measured, one can attempt to correct for this effect. This can be done by a method called finite impulse response (FIR). This method is described in Appendix C. With the cross-talk values determined using the direct measurement, the FIR coefficients can be calculated. The correction can then be applied to the data. This is shown in figure 4.34, where the direct measurement of the cross-talk is repeated with the corrected strip signals. One can see that the distributions are nicely centered around zero on both sides of the seed strip. The width of the distribution is again a measure of the average single strip noise. In figure 4.35a the $\eta_{\text{telescope}}$ distribution is shown with the strip signals corrected with the FIR method. One can see that after the correction the peaks are well centered around zero and one as it would be expected for a situation without cross-talk. In Figure 4.35b, the distribution of $\eta_{\text{telescope}}$ is shown as a function of the reduced predicted impact position. Here it can be seen that the correction works well and events where the middle between two strips is hit still correspond to intermediate values of η. Note that values below zero and above one are also possible with this definition. It is also possible to reconstruct cluster positions using this correct η-distribution, but a redefinition of the algorithms might be necessary due to the negative values which are possible.

4.3.7 Clustering Algorithms

In this section, the different cluster algorithms which were introduced in section 4.2.1 are compared.

For the η-algorithm, input functions $f(\eta)$ are used, which are obtained from (uncorrected) η-distributions as shown in the previous sections. An example of the input functions can be seen in figure 4.36, where $f(\eta)$ is shown as a function of η for different incident angles for the non-irradiated OB1 module.

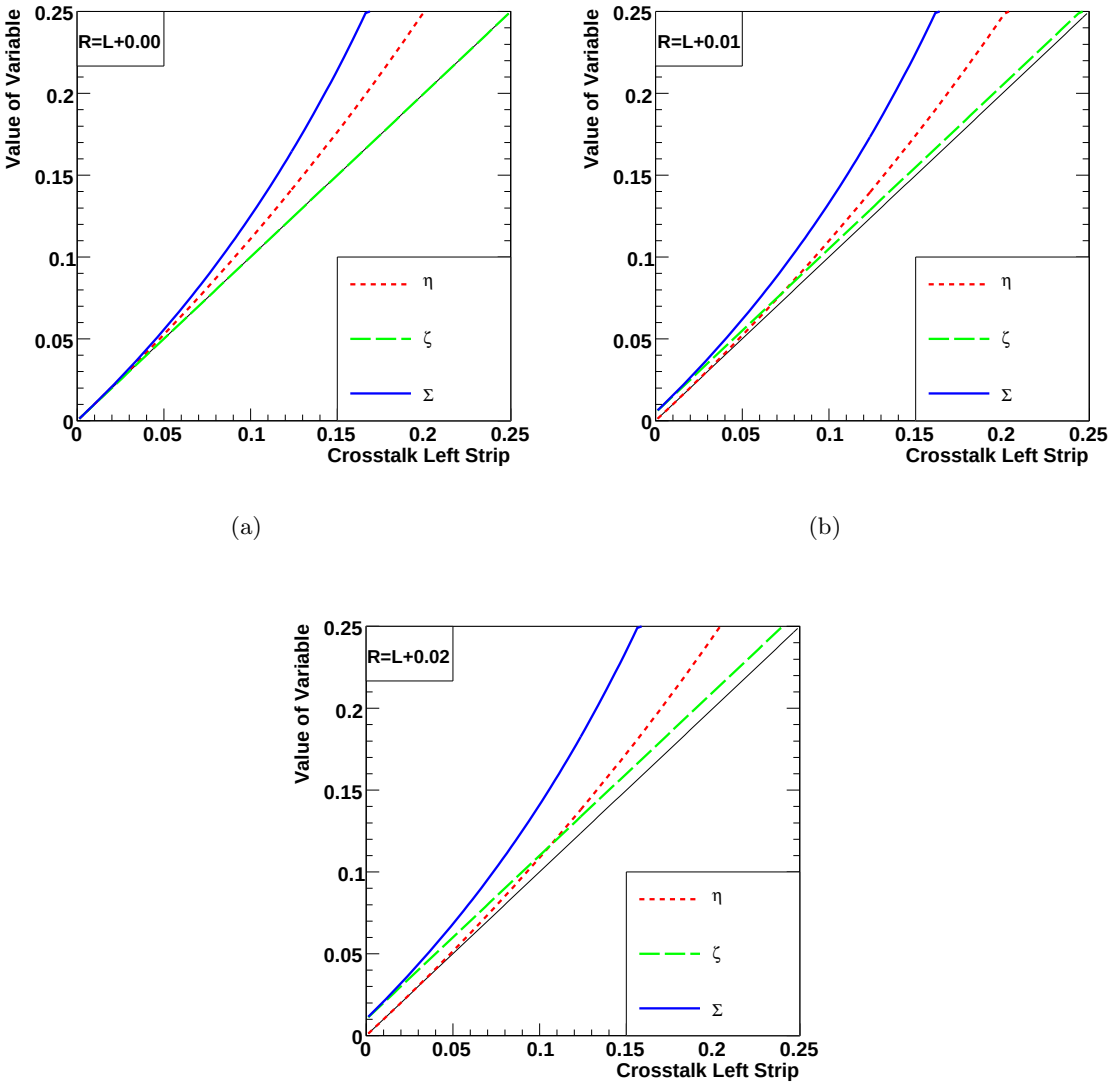

Figure 4.33: Cross-Talk variables as a function of the input cross-talk with an asymmetry of 0.00 (a) 0.01 (b) and 0.02 (c) between the cross-talks on the two neighboring strips. The 45° line is shown in black to guide the eye.

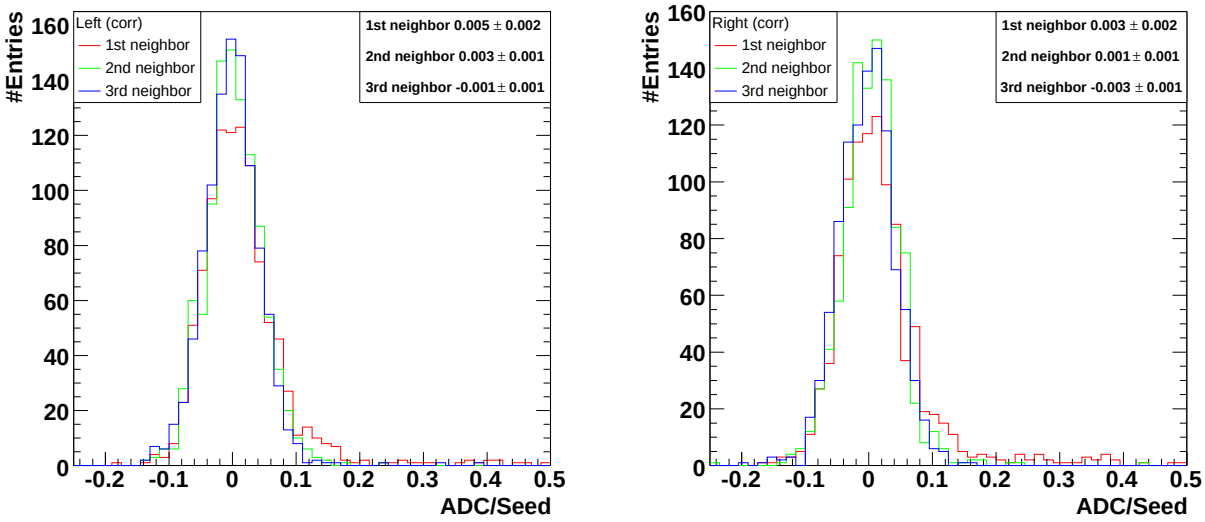

(a) (b)

Figure 4.34: Strip charge in units of the charge of the hit strip for three strips on the left (a) and on the right (b) side of the seed strip after finite impulse response correction.

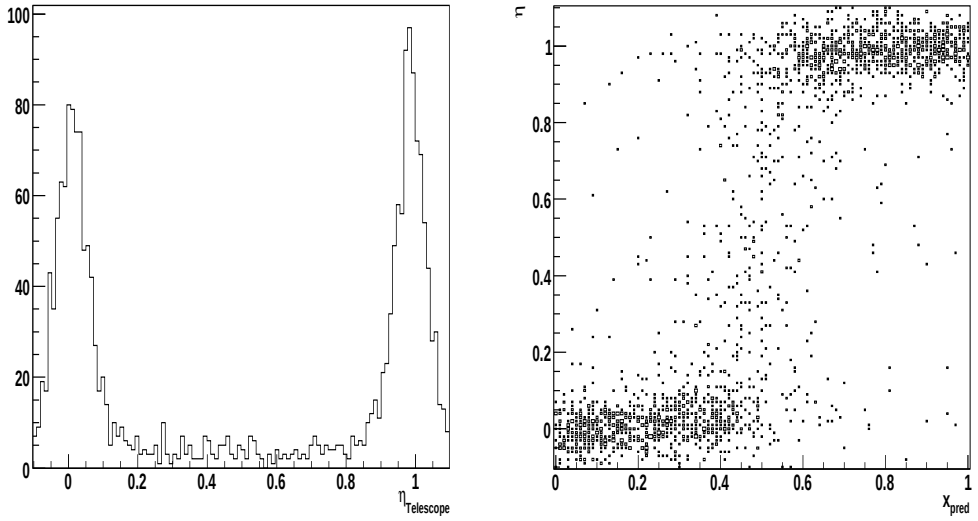

(a) (b)

Figure 4.35: $\eta_{\text{telescope}}$ using strips corrected for cross-talk (a) and as a function the predicted hit position (b).

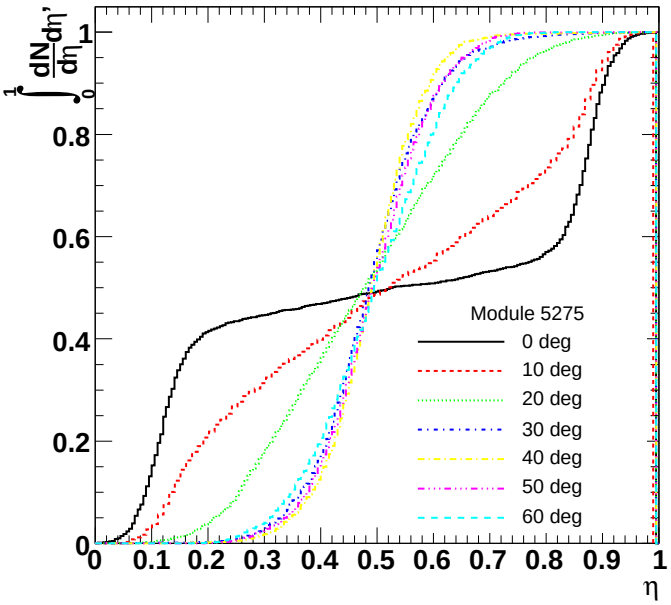

Figure 4.36: Integrated η-function for different incident angles.

Comparison of Cluster Algorithms

Figure 4.37 shows the resolutions for the different algorithms for the non-irradiated OB1 module. It can be seen that different algorithms perform best in different angular regions. For 0° incident angle, all algorithms apart from the head-tail algorithm perform very similar, showing a resolution close to the expected binary resolution. At small angles ($< 20°$), the η-algorithm performs best. At 10°, the obtained resolution is about 14 μm, compared to 22 μm for the standard weighted algorithm, which is an improvement of around 35%. At 20°, the improvement is still about 10%. The double centroid does not show an improvement with respect to the standard reconstruction, and shows a resolution which is almost a factor of 2 worse than for the η-algorithm. It can also be seen that the resolution for the binary algorithm stays roughly constant as can be expected. For 30° and 40° the standard algorithm is performing better than the other algorithms. At values of 50° and 60° the head-tail algorithm performs better than all other algorithms, an improvement of 30% and 20% with respect to the standard algorithm can be seen.

In figure 4.38 the three algorithms which performed best in any of the regions are compared for the non-irradiated and the highest irradiated module. The results for non-irradiated and the irradiated module are stable within 10% for all algorithms. This shows that the results for the various clustering algorithms will be stable even after 10 years of LHC running.

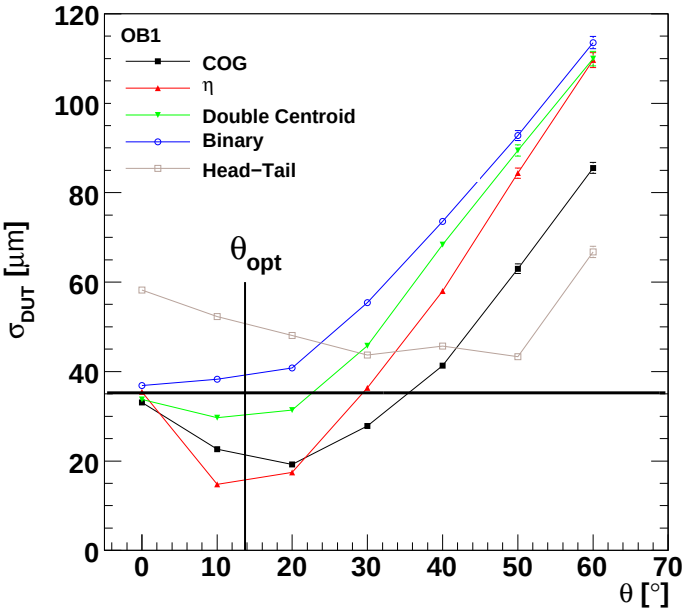

Figure 4.37: Measured spatial resolutions for different cluster algorithms as a function of the incident angle θ.

Conclusion for Cluster Algorithms

The following conclusions can be drawn from the results shown before. At incident angles $\geq 40°$, the head-tail algorithm performs best and can be used to improve the reconstruction of highly inclined tracks. As shown in figure 4.29b, the cluster size could be used as an estimator for the track angle. At small inclination angles, the resolution can be improved using the η algorithm. As shown in figure 4.38, these results do not change after high fluences.

While the head-tail algorithm can be used directly, the η algorithm needs the f(η) distributions as input. This means that the η algorithm is probably not well suited for online reconstruction.

4.4 Summary and Outlook

Data taken with an electron testbeam with irradiated and non-irradiated silicon modules from different parts of the CMS silicon strip tracker have been analyzed. The data were taken at the testbeam area 22 of the DESY II synchrotron at DESY in Hamburg. A precision hodoscope (telescope) provided an external track reconstruction. The modules were housed in a special box to control ambient conditions. Both angular and position scans were possible with the setup. Data were mostly taken in deconvolution mode, since this will be the relevant run mode for the modules after several years of LHC running.

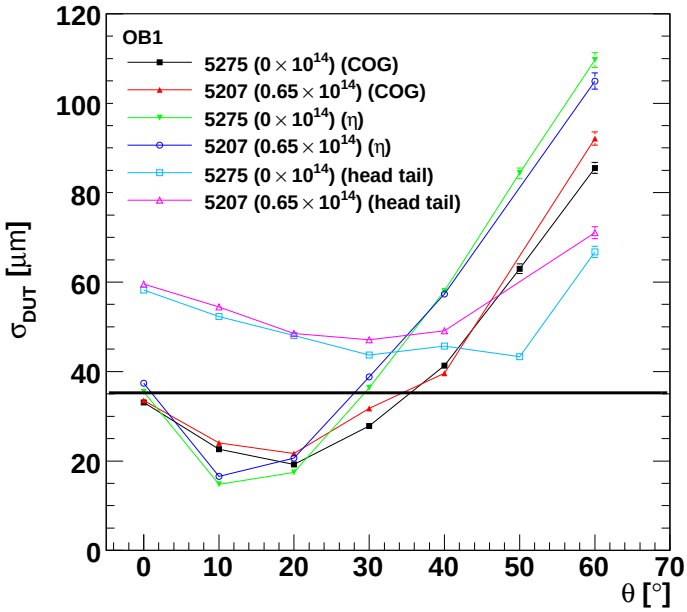

Figure 4.38: Measured spatial resolutions for different cluster algorithms as a function of the incident angle θ for the non-irradiated and highest irradiated module.

The data were pedestal and common mode subtracted. The modules show a stable noise behavior under the various operating conditions. Different scans were performed and analyzed. The modules show the expected behavior for a variation of the applied bias voltage. Even at the highest irradiation levels, the modules can be operated safely, reaching signal-to-noise ratios well above the goal of a signal-to-noise ratio of 10. Also for the variation of the ambient temperature, the behavior of the modules is as expected.

For scans in the beam energy, different positions on the sensor and the incident angle of the particles, data from the telescope was available. The measured spatial resolutions are well within the expected range and are stable also after irradiation. This also holds true for different positions on the sensor.

In the angular scans, the signal level increases as expected due to the increased path length in the detector. Due to beneficial charge sharing, the spatial resolution improves up to an optimum angle which is in agreement with the expected one. No change is observed in the behavior of the modules for different irradiation levels.

For some runs, the charge collection and the cross-talk is investigated in more detail. The found behavior is consistent with the expectations. The cross-talk is found to be about 10% to the neighboring strips. The increase with increasing irradiation is of order of few percent.

Different cluster algorithms are compared for different incident angles and fluences. It is found that the resolution can be improved up to 35% compared to the used standard reconstruction algorithm. The use of the η algorith, however, is likely to be possible only in an offline reconstruction of the data as memory consumption will probably forbid its

application in the HLT where the online reconstruction takes place.

Summarizing it can be said that the modules under investigation perform very well, reaching or exceeding the posed requirements. The spatial resolution can still be optimized for certain scenarios with respect to the current scheme.

5 Testing of Large Structures – The CMS Silicon Tracker Slice Test

After the testing of single modules described in the previous chapter, the performance of larger structures is investigated. The so-called "Slice Test" of the CMS Silicon Strip Tracker took place at CERN from March to July 2007. The strip tracker was mechanically completed and a large part was connected to powering and readout. In this thesis, data from two TEC sectors which took part in the Slice Test are analyzed. Special emphasis is put on the noise stability. Furthermore, the stability of different operational parameters of the system is analyzed. This chapter is structured as follows: First, the goals of the Slice Test will be described. Next, the setup and the measurement program will be outlined. After this, studies on the noise stability, different grounding and readout configurations will be described. In the last part, defects of components will be indicated and their distribution in the TEC sectors participating in the Slice Test setup will be shown. For other results from the Slice Test see [58–60].

5.1 Goals of the Slice Test

The goals of the Slice Test comprised several aspects of the tracker operation.

- A common commissioning procedure for all subdetectors had to be established. This ensures that all subdetectors can be read out simultaneously.
- Safe operation of the tracker had to be ensured. Dedicated monitoring of all important operation parameters has been performed. This included monitoring of low- and high-voltages as well as temperatures and dew points.
- The performance of the system should be tested at various operation temperatures. The stability of the system was investigated with respect to signal and noise, as well as to mechanical deformations (alignment).
- Cosmic muon data should be recorded and transfer and reconstruction chains should be established. Data quality monitoring tools were used to check the quality of the data both online and offline.

5.2 Slice Test Setup

The Slice Test was performed after the assembly of all sub-components of the strip tracker at CERN. A dedicated clean room area was available for the assembly, the so-called Tracker Integration Facility (TIF), which was also used for the Slice Test. Furthermore, a Tracker Analysis Center (TAC) was set up in close proximity to the TIF to enable easy monitoring

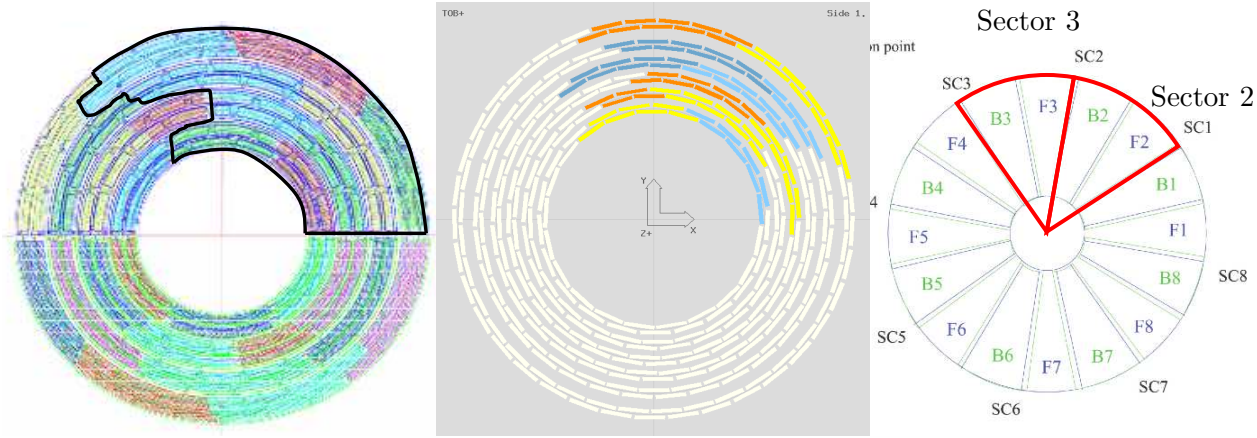

(a) (b) (c)

Figure 5.1: Schematic display of the read out configurations used in the CMS Tracker Slice Test from the (a) TIB, (b) TOB and (c) TEC.

and maintenance. A significant part of the tracker was connected to powering, cooling and readout. The hardware for powering and readout was identical to the final one. For the cooling a special cooling unit was used with reduced cooling power compared to the final system. The cooling plant also enabled running at different temperatures. Commissioning and cosmic data were taken at coolant temperatures of +15°C, +10°C, 0°C, -10°C and -15°C. At -15°C, only about 50% of the connected modules took part due to limitations in the cooling power of the system. The read out "slice" comprised about 25% of the $+z$ side of the tracker. This corresponds to 12.5% of the total system. The slice contained more than 2000 silicon modules from all strip tracker subdetectors (TIB, TID, TOB and TEC) with an active area of more than 25 m^2. The geometric distribution of the read out modules for TIB, TOB and TEC is depicted in figure 5.1. All participating modules are located in the upper part of the strip tracker and cover a similar region in ϕ. The total number of modules and readout channels for the different subdetectors and for the whole slice is listed in table 5.1. In the barrel part of the detector, ten silicon layers were available for tracking. The positive tracker end cap (TEC+) took part with two of the eight sectors (2 and 3, cf. figure 5.1c) with all nine discs. The setup was equipped with a cosmic trigger which consisted of scintillators above and below the tracker support tube to reconstruct vertical tracks through TIB and TOB, as well as an inclined tracks through the TEC and TID (for detailed results from the tracking performance at the TIF, see [59]).

5.3 Commissioning

At set of calibration runs is taken prior to data taking. This procedure is described in the following and will be abbreviated by *commissioning*. It comprises the following steps:

1. adjustment of laser amplification,
2. final adjustment of the timing,

Table 5.1: Number of readout channels and modules for the Slice Test per subdetector and for the whole system.

(Sub-)Detector	Number of Modules	Number of Channels	Fraction of subdetector
TIB	438	282,624	16%
TID	204	141,312	25%
TOB	720	476,460	15%
TEC	800	483,328	13%
Tracker	2162	1,383,424	15%

3. pedestal and noise determination.

Most analyses presented were performed using software which was already used during the integration of one of the tracker end caps (TEC–). The commissioning of the tracker is performed as described (e.g.) in [61].

5.3.1 Gain Scan

After a first coarse adjustment of the timing, an optical link setup run (often refered to as *gain scan*) is performed. This has the goal to adjust the gain of the laser system such that the dynamic range of the system is used in the best possible way. For this, the synchronization pulses sent by the APV chips (so-called *tick marks*) are used.

The data structure of the APV consists of a three bit digital header, followed by an eight bit address to identify the pipeline cell. Next follows an error bit which can be set in case of erroneous behavior of any of the chips components, and finally the 128 channel analog data. A tick mark is sent immediately after a data frame if no further data follows. In the absence of data, tick marks are issued every 70 clock cycles by the APV. The height of the tick mark is 8 mA or 800 mV at the input of the Analog-Opto-Hybrid. To estimate the gain of the optical link, the ratio of the height at the input (800 mV) and at the Front-End-Driver (FED) is compared. The FED has a conversion of 1 ADC count/mV, hence dividing the tick height in ADC counts by 800, one obtains the gain factor in units of V/V. As mentioned in section 3.2.6, a value of 0.8 V/V has been specified as the optimal one [41].

During a gain scan, the tick height is determined from the difference between the lowest and highest signal level (digital ZERO and ONE) sent by the APV. The sampling point is defined by the laser bias setting at which the lasing starts for a digital ZERO. This is indicated in figure 5.2 where the signal at the FED is displayed as function of the laser bias for digital ZERO and ONE, respectively. The resulting tick height is indicated in the figure. After a gain scan, the gain setting which gives the result closest to 0.8 V/V is chosen. The resulting distribution of the lasers among the four gain settings is shown in figure 5.3a for a run at +15°C and figure 5.3b at -10°C. It can be seen that in both cases the bulk of the lasers is operated in gain setting 1. The number of lasers in gain setting 2 and 3 decreases with temperature, while the number of lasers in gain setting 0 increases. This behavior is expected, since the laser gain increases with decreasing temperature (see e.g. [37]) As has been noted in [62], lasers operated in gain setting 0 may suffer from a loss in dynamical range if the tick height gets too large in this setting. Lasers which have to be operated in gain setting 3, may suffer from signal loss over the lifetime of the experiment. The evolution

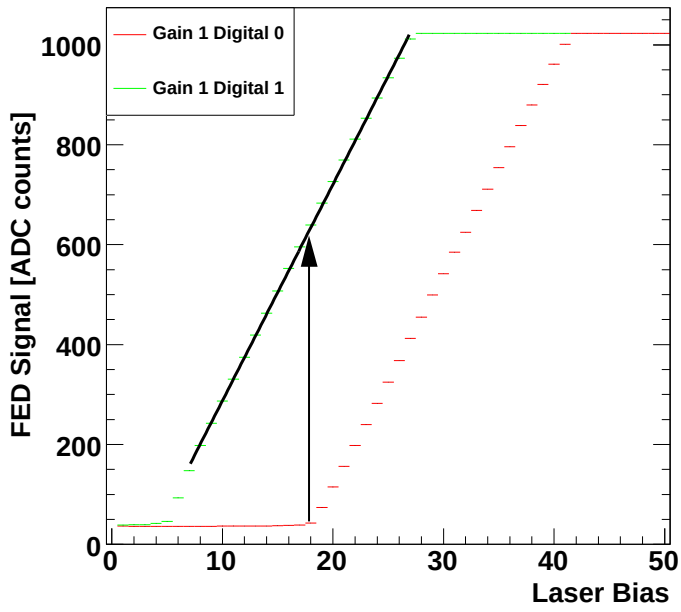

Figure 5.2: Distribution of measured pulse height for digital ZERO and ONE sent by the AOH laser driver and reconstructed by the FED as function of the laser bias. The resulting tick height is indicated in the figure.

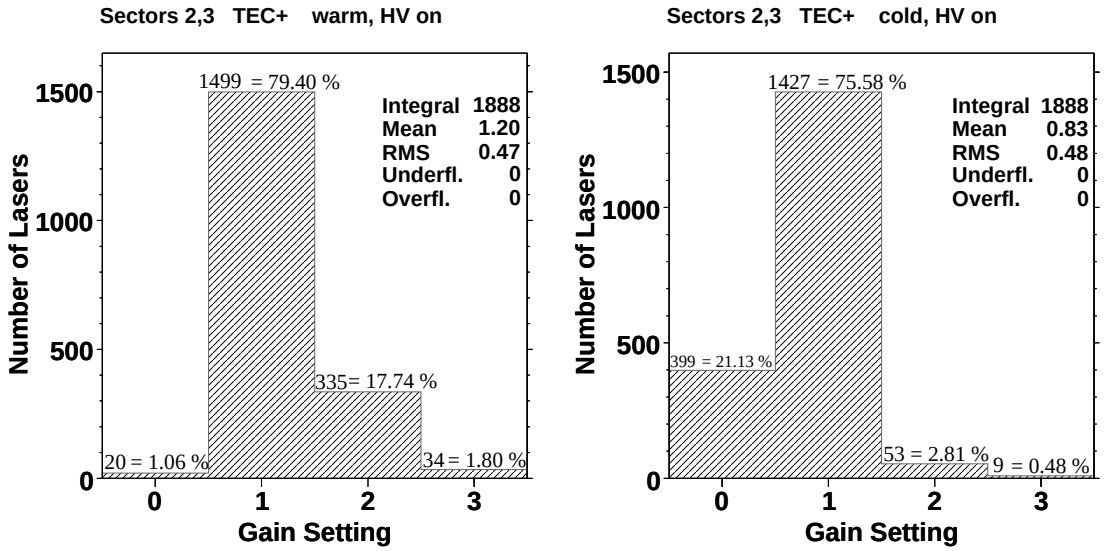

(a) (b)

Figure 5.3: Distribution of gain settings for lasers in TEC sectors 2 and 3 at +15°C (a) and at -10°C (b).

of the gain settings with temperature is summarized in figure 5.4 where the number of lasers in each setting is displayed as function of the run number.

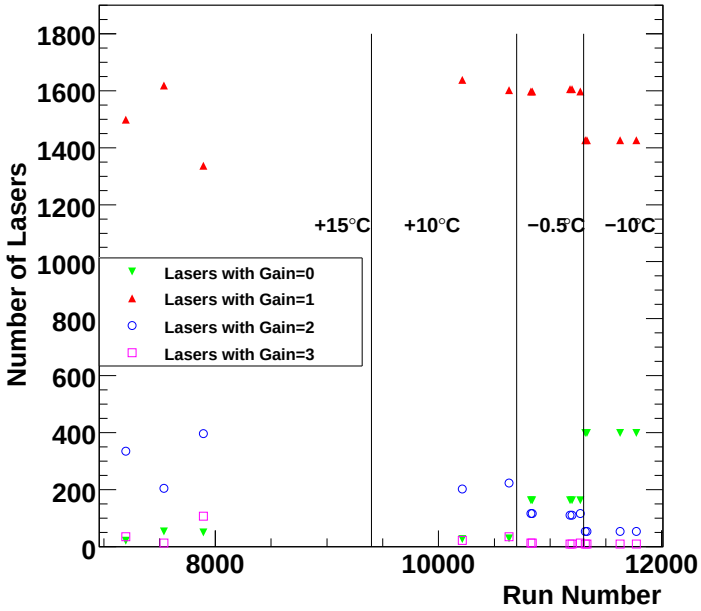

Figure 5.4: Distribution of gain settings vs. run number for two TEC sectors. Run periods with different coolant temperatures are indicated.

5.3.2 Timing Run

After the adjustments of the gains, the timing of the system is adjusted to account for differences in propagation length in the optical link system. Furthermore, the optimal sampling point has to be determined since each nanosecond of timing misalignment results in a signal attenuation of 4% [61]. The results of the timing run can furthermore be used to check the outcome of the gain scan. For this, the time domain distribution of the tick marks is investigated. An example of this is shown in figure 5.5 where tick marks from two lasers (four APVs) are shown from one module in the slice. It can be seen that the timing of the modules is indeed perfectly aligned. It can also be seen that the tick heights vary among the individual lasers. The tick heights from all lasers in the two sectors in the slice can be seen in figure 5.6(a) for one run at +15°C. The mean value of the distribution is centered nicely around the design value of 640 ADC counts. In figure 5.6(b), the equivalent distribution is shown for a run at -10°C. It can be seen that the mean value is roughly constant even though the shape of the distribution is altered. The altered shape results from the switching of lasers from one gain setting to the next. This switch occurs when the gain factor falls below 0.64 (512 ADC counts) or rises above 0.96 (768 ADC counts) [62] to the next higher or lower level, respectively, if available. The stability of the mean value is

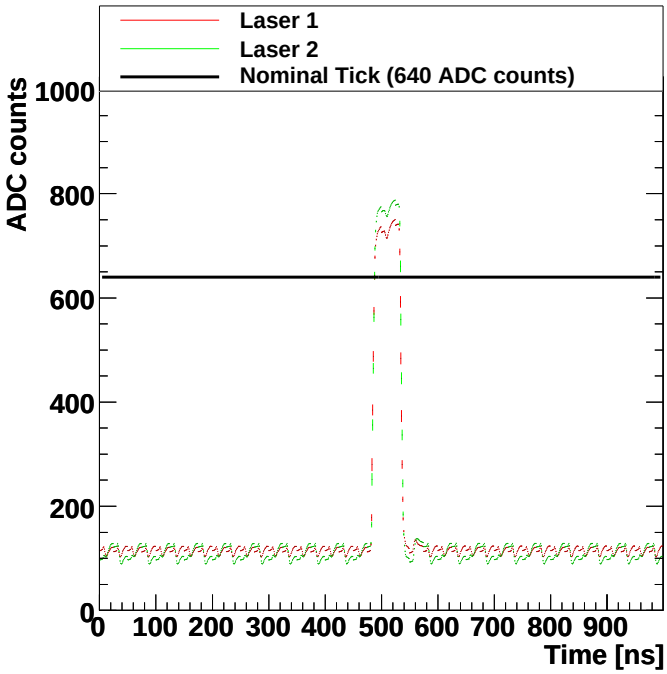

Figure 5.5: Time domain capture of tick marks from 4 APVs (2 lasers) from one module. The nominal tick height of 640 ADC counts is indicated.

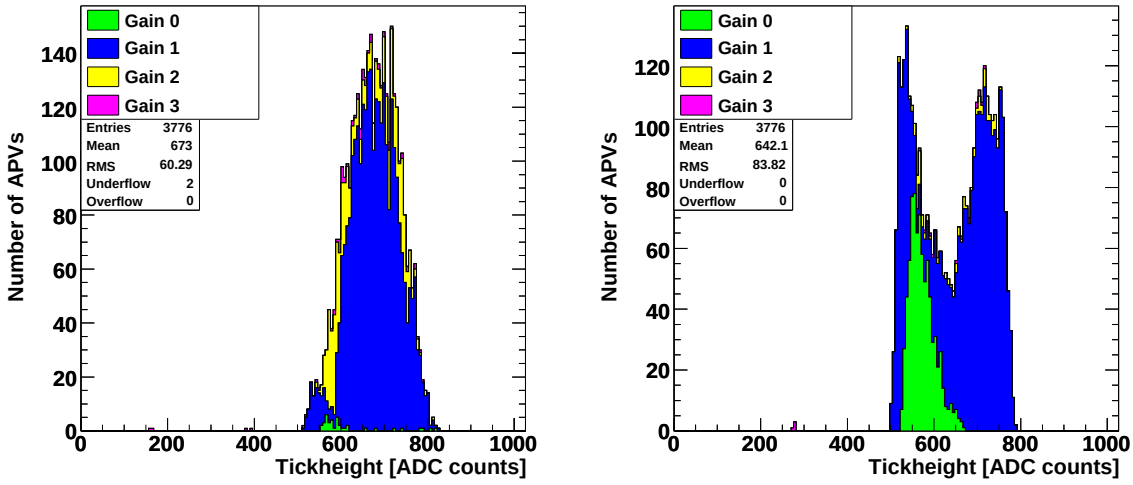

(a) (b)

Figure 5.6: Reconstructed tick heights for two TEC sectors at +15°C (a) and -10°C (b).

summarized in figure 5.7 where the mean value of the tick height is shown as function of the run number. Transitions between different operating temperatures are indicated in the figure. It can be seen that the value is stable around 640 ADC counts which indicates that the gain adjustment works as foreseen.

The tick value for a given APV can be used to convert the response from a FED to the equivalent electric charge collected in the detector. For this, the internal amplification factor of 1 MIP/mA in the APV has to be taken into account. For an assumed tick height of 8 mA and an ionization of 25,000 electrons for a minimum-ionizing particle in 300 μm of silicon, one arrives at a charge equivalent of 200,000 electrons for the tick. This can be used for the conversion according to

$$\text{signal}_\text{e} = \text{signal}_\text{ADCcounts} \frac{200{,}000\ e}{\text{tick height}_\text{output}}. \tag{5.1}$$

The noise figure in electrons will be called *scaled noise* in the following.

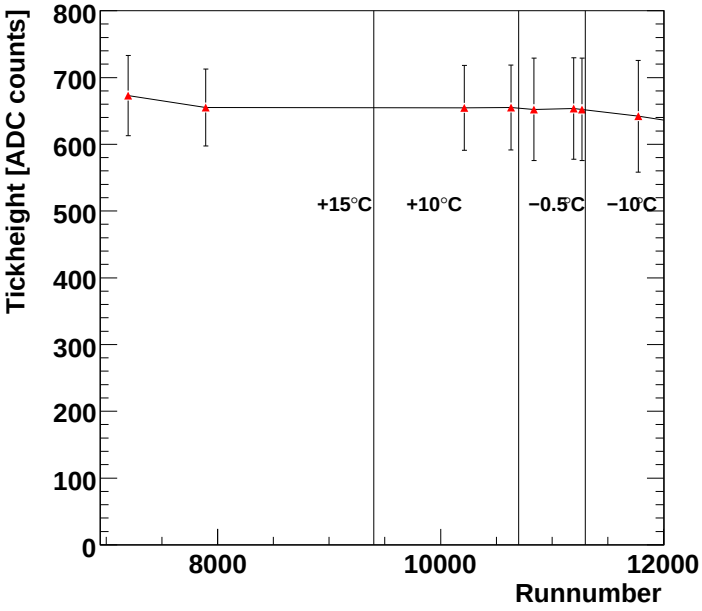

Figure 5.7: Mean value of tick heights as a function of the run number for two TEC sectors. Run ranges with different temperatures and temperature transitions are marked in the figure.

5.3.3 Pedestal Run

During a pedestal run, data are recorded with random triggers to determine the response of the detector in the absence of physics events. The data are analyzed similarly to what has been described in section 4.1. First, the pedestal and raw noise of a channel are determined.

The common-mode is determined and subtracted per event. In the Slice Test, the common-mode is determined for groups of 128 channels (1 APV). In figure 5.8, the raw noise and the common-mode subtracted (CMS) noise are displayed for one module from the two TEC sectors using the conversion factor into electrons from equation 5.1. It can be seen that the common-mode (i.e. the difference between the two distributions) is small. Furthermore

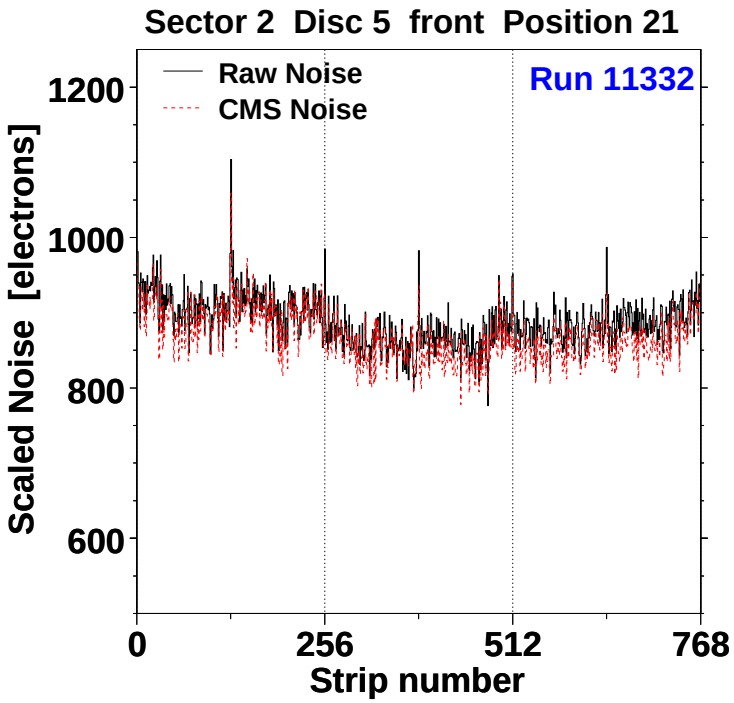

Figure 5.8: Example of raw noise and common-mode subtracted noise for one module from the slice test setup for one run at -10°C.

it can be seen that edge strips tend to have a higher noise compared to non-edge strips. In figure 5.9, the noise behavior of one whole sector is summarized. The mean raw noise and the mean common-mode subtracted noise per APV chip is shown as function of the position in the sector. The disc number increases from left to right; each disc is subdivided into front (blue) and back petals (red). Within a petal, the ring number increases from the left to the right. It can be seen that, on average, the noise increases with increasing ring number, which is due to the increase in strip length with increasing radial distance to the beam line. This scaling behavior can be used to normalize the noise figures from different module types to a common reference. The strip length of the modules from the innermost TEC rings is chosen. The scaling factor is determined from a fit to the distribution of the mean noise values of the different strip length. This is shown in figure 5.10 where the mean noise for a given strip length ($\pm$ 1 standard deviation) is displayed as a function of the strip length. One can see that there is a linear scaling of the noise. A first order polynomial fit to the data is shown in the figure. The fit parameters are used to scale the noise from each strip to the reference length. The outcome of this procedure is displayed in figure 5.11

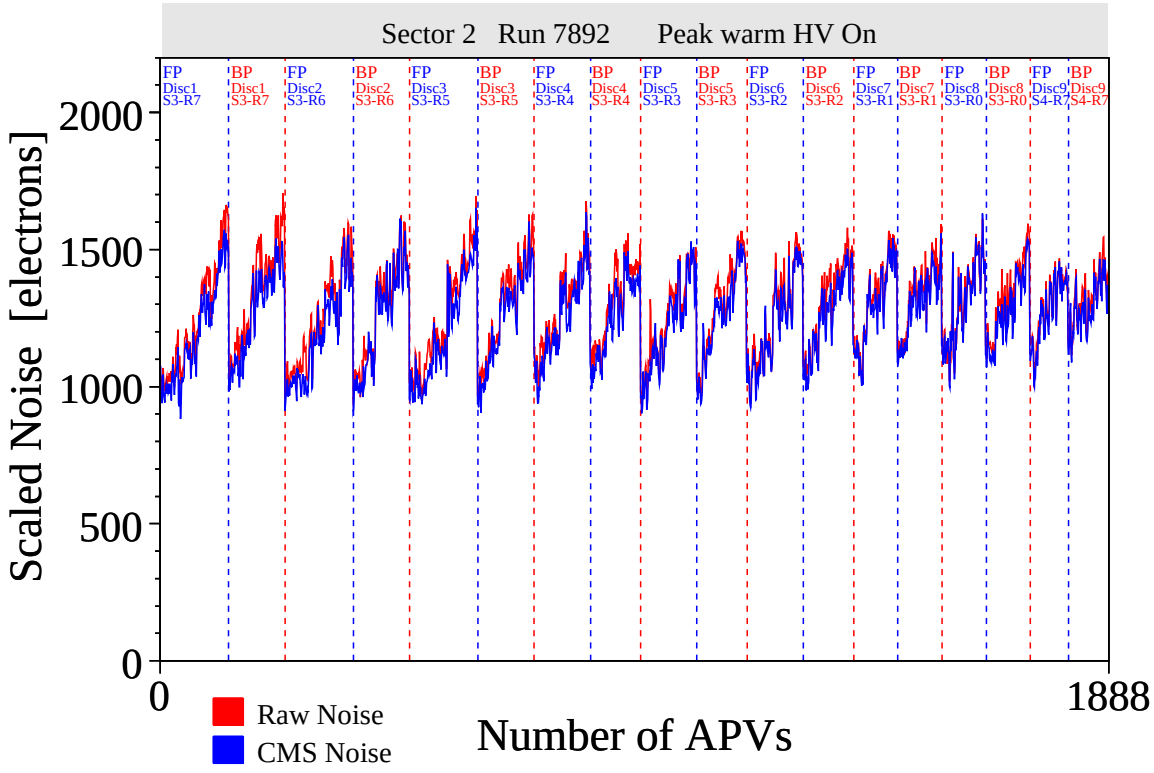

Figure 5.9: Mean raw noise (red) and mean common-mode subtracted noise (blue) per APV for one TEC sector. Front petals are shown in the blue bins, back petals are shown in the red bins. The ring number increases from left to right in each petal.

where the noise for each strip in the two TEC sectors in the slice is shown, normalized to electrons using the gain factor for the respective APV and scaled to the strip length of ring 1. The plot is shown for normal, dead and noisy strips separately. In the following, only normal strips are considered (for details on dead and noisy strips see section 5.6). The strip noise follows an almost Gaussian distribution with some outliers above and below the bulk of the distribution which are located on single components which show a sub-standard but otherwise fine behavior. A Gaussian fit to the central distribution results in a mean normalized and scaled CMS noise of 894 electrons.

5.4 Noise Stability

The noise behavior of the silicon modules is very important for the operation of the tracker. Therefore, the evolution of the noise with temperature and for different powering and readout schemes is evaluated. Several effects influence the noise of the silicon modules at different temperatures. One effect is the dark current in the silicon bulk material, which is related to the occupation probability of states in the band gap (cf. chapter 1). For the modules in the CMS tracker, another important contribution to the temperature dependence is introduced by the APV chip. In [63] it has been estimated that a change of 10–15% in the noise figure

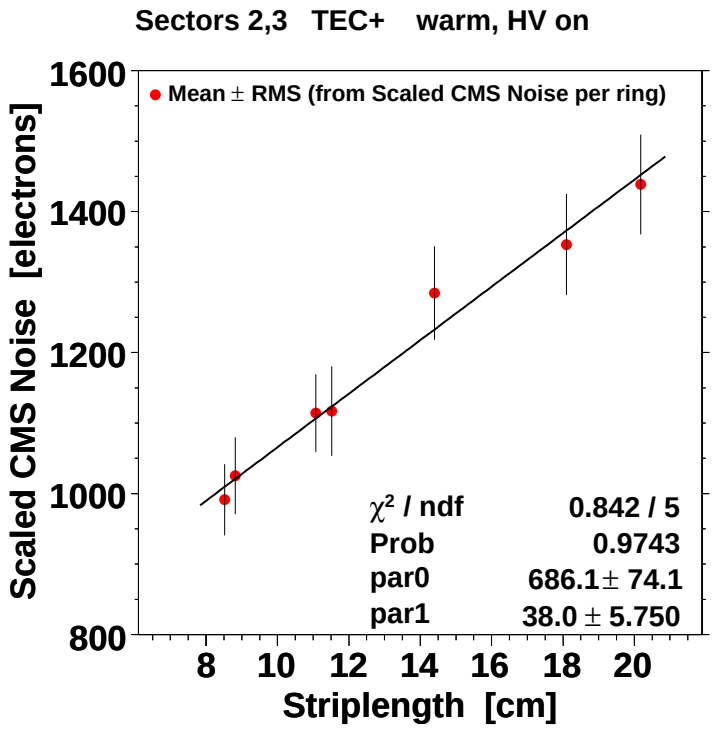

Figure 5.10: Noise scaling with strip length for modules from TEC sectors 2 and 3.

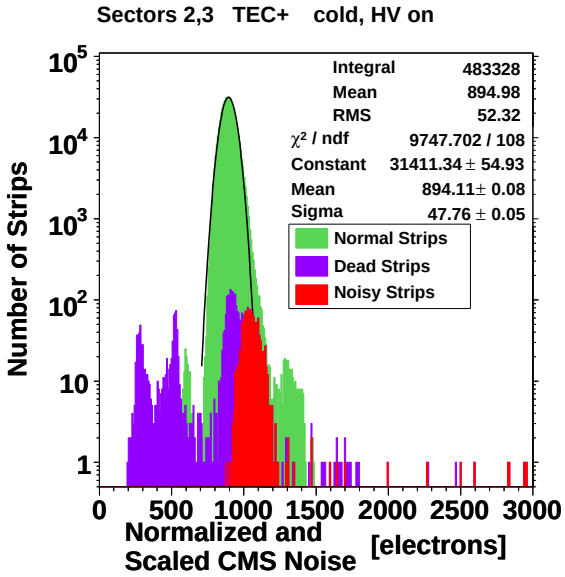

Figure 5.11: Normalized and scaled single strip noise for both sectors for two runs at -10°C. Dead strips are shown in purple, noisy strips are shown in red, normal strips are shown in green. A Gaussian fit to the central part of the noise distribution for normal strips is shown.

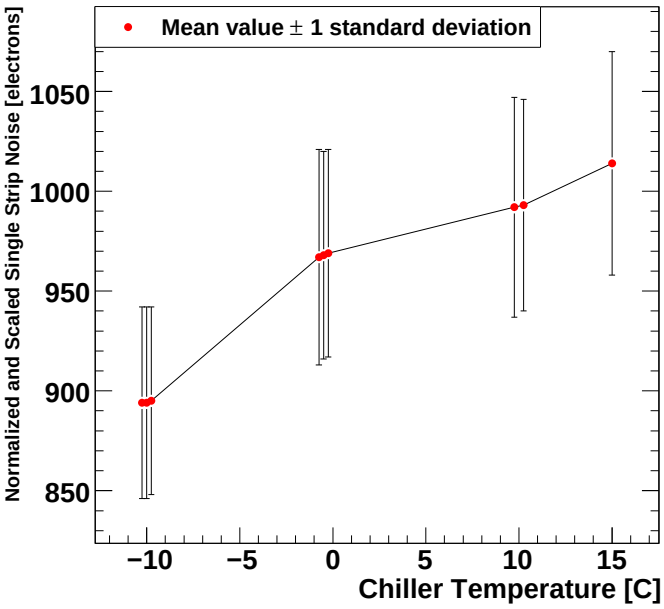

Figure 5.12: Mean values ±1 standard deviation of the normalized and scaled CMS noise at different coolant temperatures during the slice test. Runs at one temperature step are drawn at temperature points ±0.25°C for visibility. The temperature refers to the temperature of the cooling fluid.

can be expected for a change of 40°C in the ambient temperature. In figure 5.12, the mean value (±1 standard deviation) from the Gaussian fit to the scaled and normalized common mode subtracted noise (CMS noise) is displayed as function of the input temperature of the coolant (chiller). Runs at the same temperature are drawn at ±0.25°C with respect to the coolant temperature to enhance visibility. The noise reduces with temperature as it is expected. The noise changes by about 10% for a change of 25°C in the temperature. This is in qualitative agreement to the expectation quoted above. A more quantative estimation is not possible since the temperature of the cooling fluid can not be directly related to the temperature of the silicon or the hybrid. From the figure it can be seen that the mean value and standard deviation of the noise distribution is stable for a given temperature.

In addition to the absolute noise figure also the relative change due to different temperatures for each individual channel is investigated. This is done by comparing the noise figures from two runs. An example of this is shown in figure 5.13 where the difference of the normalized and scaled CMS noise is shown for all normal strips (see above) from the two TEC sectors for two runs at +10°C and -10°C, respectively. The distribution is fitted with a Gaussian. The data are well described by the fit, except for a group of modules which experienced problems in the power supply during one of the two runs. In figure 5.14 the mean value and standard deviation of these distributions are shown for several runs with respect to a common reference run. It can be seen that the noise difference for the

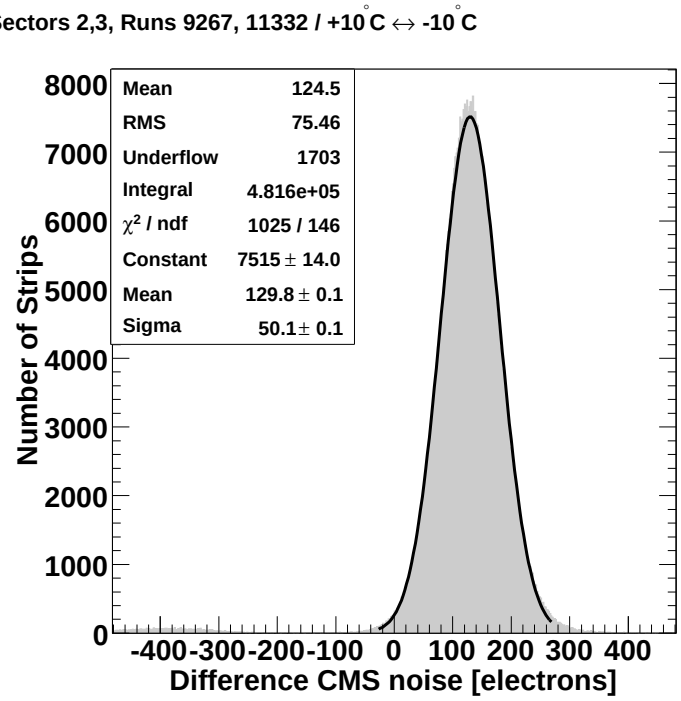

Figure 5.13: Single strip difference of the common mode subtracted noise for both TEC sectors for two runs at +10°C and -10°C.

individual strips is stable for a given temperature and also the standard deviation of the distribution is largely stable. The reference run is also indicated in the figure and has mean value and standard deviation equal to zero by definition.

5.5 Powering and Readout Studies

In addition to crosstalk among single readout strips, described in chapter 4, also crosstalk among different subdetectors can be present. To exclude possible interference between the different subsystems, studies with different powering and readout schemes were performed. For these studies, a special subset of modules from the TEC sectors was read out separately: Three of the petals which were powered through a prototype patch panel (PP1)[1]. First, the stability of the noise is checked. In three pedestal runs, all modules which are connected through the patch panel were powered. This is shown in figure 5.15a, where two of the runs are compared to the third run. It can be seen that the noise difference is small and stable within below 2%. One of the above runs is taken as reference for the following comparisons.

Next, the powering scheme described above is compared to two different schemes: in the first run (7915) the complete TEC sectors were powered; during the second run (7942), only the petals integrated in the readout partition were powered. The result of this can be seen

[1] A total of 15 petals was powered wholly or partly through this patch panel

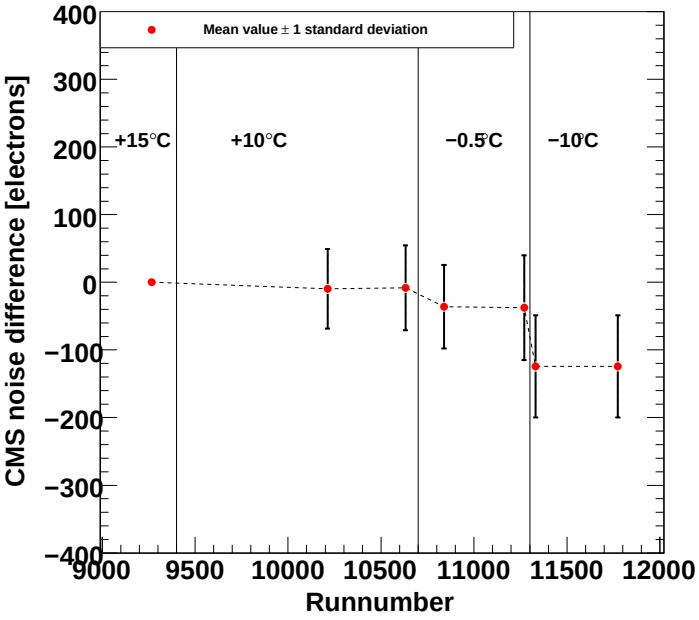

Figure 5.14: Single strip noise difference for different running periods for the two TEC sectors with respect to a reference run at 15°C. The mean value ±1 standard deviation is shown. Run ranges with different temperatures and temperature transitions are marked in the figure.

in figure 5.15b, where the two runs are compared to the reference run. It can be seen that the noise is very similar for all runs. A small shift of few electrons and a similar increase of the width can be seen, which can probably be attributed to fluctuations in the temperature due to changes in the powering state on short timescales. The overall change of the noise is again of the order of about 2%. It can be concluded that there is little sensitivity of the noise to the powering of modules in the TEC. Finally, the sensitivity to powering of other subdetectors is checked. Three different powering states of the tracker outer barrel are investigated. In the first run (8143), the whole TOB is powered. In the second run (8144), only those modules of the TOB, which are powered through the same patch panel, are powered. In the third run (8148), the TOB modules powered through PP1 are powered and also receive random triggers. The noise difference with respect to the reference run is shown in figure 5.15c. It can be seen that no additional fluctuation of the noise is introduced; the mean value and width of all three distributions is similar to the TEC internal runs. From the above investigations it can be concluded that the TEC shows very little sensitivity to changes in the powering and readout scheme.

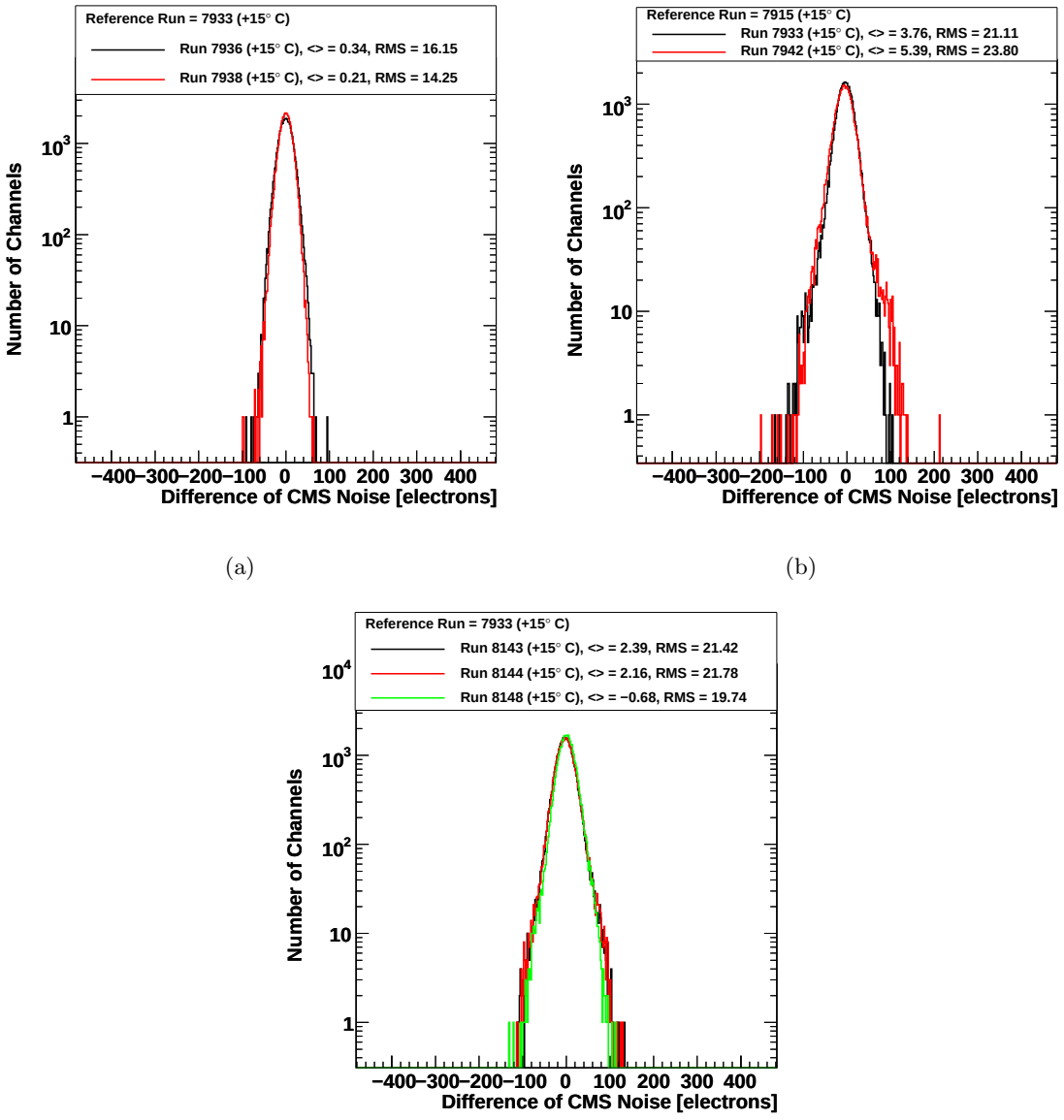

(a) (b)

(c)

Figure 5.15: Single strip noise difference of two different runs with respect to a reference run with identical conditions (a). Comparison of two runs with varying powering schemes in the TEC sectors to a reference run (b). Comparison of runs with varying powering and readout schemes in the TOB to a reference run (c). See text for details.

5.6 Defect Monitoring

5.6.1 Classes of Defects

Several causes can be responsible for failures or sub-standard performance of components. These will not be addressed in detail in the following. Instead, the focus will be on the identification and monitoring of both persistent and temporary defects. Defects can be grouped into different categories. These are not unique to the two TEC sectors for which they will be investigated in the following, but are generic categories for all subdetectors.

Sub-standard performance : Components which fall into this category are not defect in the sense of a complete failure of the component. Instead the performance is likely to be lower than required (e.g. tickheight lower than 500 even in gain setting 3 or a bad signal-to-noise ratio). These modules can be used for analysis as they produce signals. Yet it has to be ensured that the performance does not fall below minimum requirements.

Temporary Failure : In this defect class, components show a behavior which makes the data produced by them questionable or unuseable but the behavior is not constant in time or temperature.

Persistent Failure : Defects which have no probability of recovery can be considered as persistent failure. In this case the component can be regarded as not-working and hence should be generally masked for further analysis, e.g. track reconstruction.

These defects are mostly correlated among groups of strips. Different reasons can be responsible for this:

Failure of an APV Chip: If an entire readout chip fails permanently this affects groups of 128 channels.

Failure in the Optical Chain: In this case 256 channels are affected. The failure may be due to a failure of the laser, the MUX input, the optical fiber or others. If the failure is due to problems at the back-end of the readout electronics the fiber may be recovered in contrast to on-detector defects which cannot be accessed after the integration of the system.

Failure of a Whole Module: If the communication with a whole module fails, e.g. due to problems in the DCU, a module may become unusable which in the course affects 512 or 768 channels.

5.6.2 Bad Strips

In addition to the above mentioned correlated defects, also a failure of individual strips on a module are possible. Again different categories can be identified:

Low Noise Strips

Low noise strips can be caused by a connection failure of the strip to the pitch adapter. Due to the reduced capacity, the noise of this channel will be significantly reduced with

respect to its neighbors. For modules in which two individual sensors are bonded together, the intermediate bond can be detached, leading to a similar effect.

High Noise Strips

High noise strips can be caused by large shot noise. Strips located on the APV edge tend to have higher noise compared to non-edge strips.

5.6.3 Temperature Evolution of Defects

Several effects can lead to a temperature dependence of defects. The noise of components scales with temperature and therefore a strip could be less elevated with respect to its neighbors, thereby no longer being considered as "bad". Mechanical stress can also lead to a temperature dependence since connections could be opened/closed as the system expands/contracts with changing temperature. In figure 5.16, an example of a temperature dependent defect can be seen. In this case it is a laser which shows a faulty behavior in the cold environment. This behavior was already observed during the so-called 'TEC cold test'[64, 65]. It can be seen that at +10°C, the tick mark looks as expected with a height of about 700 ADC counts, similar to the examples shown in figure 5.5. At -15°C on the other hand, no clear tick mark can be seen anymore. The exact origin of this defect is unknown.

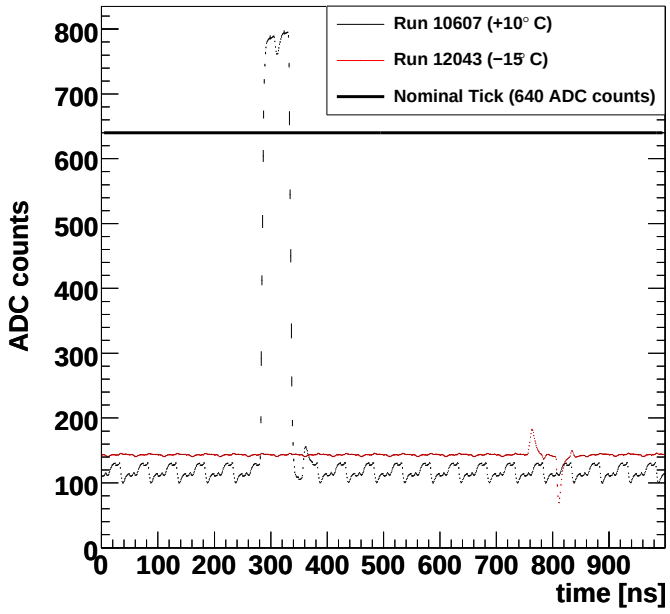

Figure 5.16: Tickmark signal as a function of time of one laser for two runs at -10°C and -15°C, respectively. For more details see text.

In figure 5.17, an example of the temperature evolution of one defect can be seen. The defect

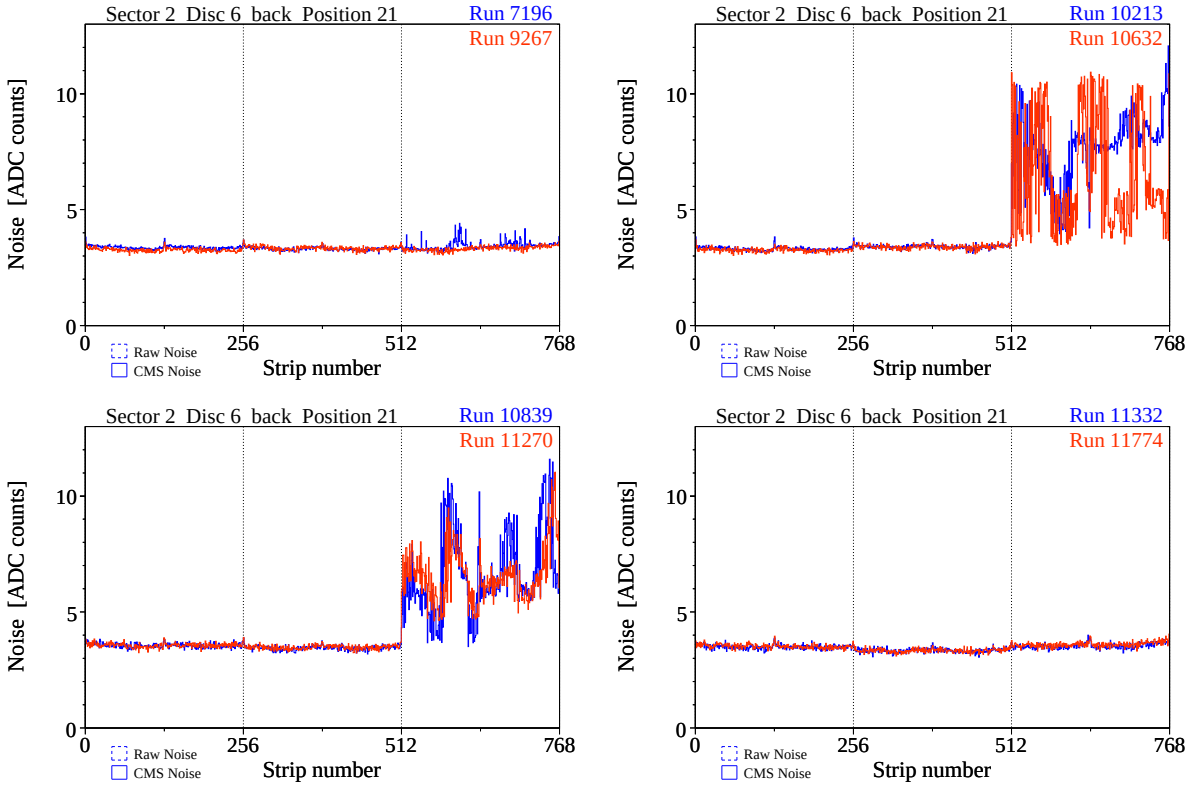

Figure 5.17: Temperature evolution of one defect identified during the slice test for +15°C (top left), +10°C (top right), -0.5°C (bottom left) and -10°C (bottom right). For each temperature, two runs are shown from near the beginning and end of the running period.

is present on one laser, i.e. 256 strips on the respective modules. For each temperature step, two runs are shown. It can be seen that there are strong differences in the noise at different temperatures, but no simple dependence on the temperature. Furthermore it can be seen that at +10°C, a strong variation is present even at a constant temperature.

This illustrates the need to mask defects of this kind in the reconstruction process as they may lead to large numbers of fake hits.

5.6.4 Summary of Defects

In table 5.2 a summary of persistent defects in the two TEC sectors is given. The evolution of defects at the different temperature steps is shown. For some of the defects it is indicated that they had already been identified before the slice test. The number of affected channels is also given in the table. It ranges from 128 channels for a single faulty APV chip to 768 channels for a module which went faulty during the slice test due to an obvious problem with the PLL (cf. section 3.2.6). It is also indicated whether the defect represents a complete failure of the component or only a sub-standard performance. The location of the defect is indicated giving the sector (S2/3), the petal type (FP/BP) and the disc (1–9), the ring

number and position within the ring (ring.position) and the laser on the module (1–3) if applicable. The total number of bad channels listed in the table is 2,944, of which 2,176 are counted as "dead" in the following since a recovery seems highly unlikely or impossible. The number of dead channels corresponds to 0.45% of the strips in the two TEC sectors. Together with the sub-standard components, a total of 0.61% of the channels are affected.

Table 5.2: Summary of persistent defects in TEC+ sectors 2 and 3 during the slice test. Modules which were not connected at -15°C are marked as "n.c". Defects which are marked with a bullet (•) in the first row are counted as dead for further analysis. See text for details

Dead	Location	Defect	No. of affected channels	+15°C	+10°C	0°C	-10°C	-15°C
•	S3 BP4 2.1/0	bad tick (known before slice test)	256	×	×	×	×	×
	S3 BP1 5.3/0	low tick	256	×	×	×	×	×
•	S3 BP5 7.3	two bad APVs (known since integration)	256	×	×	×	×	×
•	S3 BP3 4.3 1	bad APV (known since integration)	128	1	1	2	2	2
•	S2 FP3 1.4/0	laser with bad noise in dec. mode	256	×	3	4	×	n.c.
•	S2 BP6 2.1/0	laser with bad noise in peak and dec. mode	256	×	×	×	–	–
•	S2 FP7 5.4	PLL not working	768	–	×	×	×	n.c.
	S2 FP8 3.2/2	laser with high noise	256	4	×	–	–	n.c.
•	S2 BP2 7.5/0	low noise & pedestal	256	–	–	–	–	×
	S3 BP4 7.2/2	very high base tick is saturated	256	–	–	–	–	×

× = defect is present – = defect is not present
1 = bad strips 2 = low noise
3 = no run in dec. mode av. 4 = not clear

Dead and Noisy strips using Noise behavior

In section 5.6.2 the possible failure of individual strips was discussed. In the following the fraction of "bad" strips will be determined for different data taking periods. Bad strips are defined as follows: A strip which shows a noise level of more than 5σ above the average for the respective APV chip will be considered as *noisy*. Conversely, a strip which has a noise level of 5σ below the average noise for the APV will be considered *dead*. Edge strips will not be considered in the following evaluation. For an evaluation of the noise behavior of APV edge strips see e.g. [64]. In figure 5.18, the temperature evolution of the number

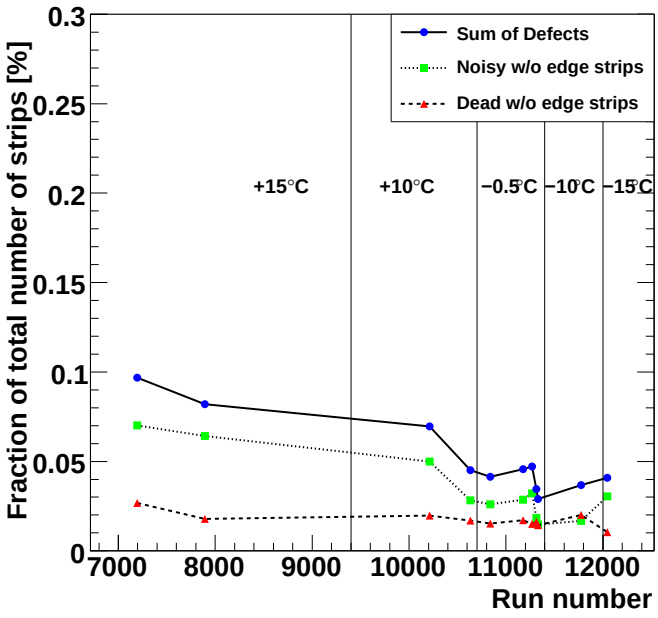

Figure 5.18: Temperature evolution of fraction of bad strips excluding edge strips and localized defects.

of individual faulty strips is shown. The number of dead, noisy and total number of faulty strips divided by the total number of strips in the two TEC sectors (483,328) is shown as a function of the run number. Boundaries between different temperature periods are indicated in the figure. In can be seen that the total number of faulty strips is below 1‰ for the two TEC sectors. Together with the 0.61% of defects and sub-standard components mentioned in the previous section, this amounts to 0.71% of the total number of channels or an average of $\lesssim$4 faulty channels per module.

5.7 Summary of Slice Test Operation

In this chapter, analyses have been presented which were performed during the tracker slice test. Several aspects of the operation and calibration of the tracker have been investigated,

notably the noise stability as function of the operation temperature as well as powering and readout schemes. Furthermore, persistent and temporary defects have been identified and monitored.

The noise behavior is found to be very good and well understood. The influence of various factors on the noise has been investigated and is found to be small, in particular the dependence of the noise on the environmental temperature and different powering and readout schemes. The noise is found to be stable within about 2%.

Defects known before the integration of the system could be reestablished. Some new defects could be identified and their temperature dependence was monitored. The fraction of persistent defects is well below 1%. The amount of bad strips which are not within groups of strips which fail due to failures of higher level components, is found to be below 1 per mille. Similar results have been found in [58].

6 Alignment

And now for something completely different.
Monty Python

In the previous chapters it has been shown that the CMS tracker performs excellent and will withstand 10 years of LHC operation. However, its excellent properties can only be used in physics analyses to the full extent if the position of the individual modules is known to the μm level. Therefore the aspect of alignment plays a crucial role for the operation of the detector both at the start-up and later.

The aim of this part of the thesis was to create a tool package which can serve as a framework for the validation of alignment algorithms and, for different datasets, of the results of alignment. Indeed, the software written is used in CMS for the validation of alignment. In the following, examples for the validation of alignment are shown for different procedures applied to a Monte Carlo simulation and cosmic data, which can and will also be of relevance for collision data.

6.1 The Concept of Alignment

The term "alignment" describes the determination or adjustment of positions and orientations of one or more objects relative to other objects. In the context of the CMS silicon tracker, alignment means the determination of the absolute position and orientation of the individual silicon modules, and the larger structures on which they are mounted, with respect to each other.

In figure 6.1, a very simple example of a possible misalignment in a tracking system is displayed. The individual modules and the measurements reconstructed on the modules are indicated. A simple 1-dimensional track fit to the data points is shown. One of the modules is moved with respect to its nominal position. To estimate the position of the modules, a residual is defined as

$$r_i = x_{i,\text{measured}} - x_{i,\text{predicted}}, \tag{6.1}$$

where $x_{i,\text{measured}}$ is the measured position on the i-th module and $x_{i,\text{predicted}}$ is the position on the module which would be predicted by the track fit. In this case, the misalignment of a single module will bias the resulting track fit for all modules. In the case of high-energy physics detectors, misalignment can lead to a very severe worsening of resolution for the measurement of particle properties, such as the transverse momentum, and can also bias the measurement. In the above case, the solution to the alignment problem is given by a simple movement of the misaligned detector plane. In general, the alignment problem is much more complex. All possible degrees of freedom for a rigid extended object, three translational and three rotational, have to be taken into account[1]. The alignment problem

[1] In the most general case, also internal degrees of freedom such as bending or sheering of the module have to be considered.

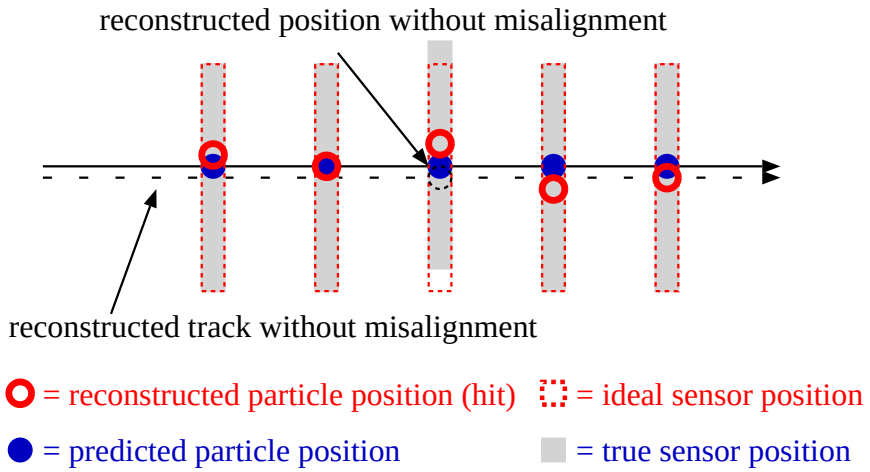

Figure 6.1: Illustration of a simple misalignment.

is mostly posed as a minimization problem in which the position and orientation of the objects to align have to be chosen in order to minimize the global χ^2 for a given sample of measurements. The χ^2 function can be defined in the following way:

$$\chi^2 = \sum_{\text{hits}} r_i^T(p,q) V_i^{-1} r_i(p,q) \tag{6.2}$$

where the sum runs over all hits associated to tracks in the given data sample. The residuals r_i are functions of the position and orientation of the module i (denoted as p) and the track parameters (q). V_i is the covariance matrix which represents the uncertainty of the residual, including correlations in case of a more dimensional measurement. The ideal set of parameters p has to be found in the alignment process. Several strategies can be used for this, some of which will be described in the following.

6.2 CMS Alignment Strategy

The CMS alignment strategy comprises several independent levels to ensure best knowledge about the alignment status at any given time. Three distinct steps of alignment procedures are foreseen which are complementary and of varying precision level.

Mounting and Survey: A high mounting precision is the first step for a good alignment of the detector. The mounting precision is checked by measurements. This provides a robust initial knowledge about the alignment of the detector and a good starting point for more refined alignment steps. Furthermore, survey measurements of larger detector structures can be used to measure possible deviations from the mounting position. This can be used e.g. in track-based alignment (see below) to put constraints onto otherwise poorly defined degrees of freedom. It should be noted, however, that survey measurements can only be done at room temperature, so that further corrections are needed to account for the shrinking of the detector at operation temperature.

Laser Alignment System: As described in Section 3.2.7, the CMS tracker has a multi-ray laser alignment system which interconnects different structures and provides position measurements with good precision for certain components in stand-alone mode. Furthermore it enables a monitoring of short-term movements of the illuminated structures. The ultimate precision of this alignment system has been estimated to be below 40μm [42].

Track-Based Alignment: The above methods do not achieve very high alignment precision levels compared to the intrinsic resolution of the employed modules. To achieve the highest degree of alignment precision, the method of track-based alignment will be used. It will be described in more detail below. A further advantage of track-based alignment is that it can be used in-situ, after the installation of the detector, at operation temperature, to correct for movements of detector parts during installation or operation. It has the disadvantage that comparably large datasets have to be used to correctly align the more than 16,000 modules as well as the intermediate structures. In a full scale Monte Carlo study, an alignment precision of 10-25 μm for the modules in the strip tracker and few μm in the pixel tracker has been obtained [66].

6.2.1 Track-Based Alignment

Track-based alignment has been used for many years in almost all high-energy physics detectors to align the central tracking detectors and other parts of the tracking system [67]. In CMS, three algorithms are investigated for track-based alignment. In this way it is possible to obtain different estimates of the alignment, which can be used to cross-check results. All three algorithms will shortly be described in the following.

Alignment Algorithms

HIP

The Hit and Impact Point (short: HIP) alignment algorithm [68] uses a local χ^2-minimization method. This is done by an independent minimization of the χ^2-sum of all hits for each module, thus updating the alignment parameters of the module in every step. Correlations between module movements are taken into account indirectly by a refitting of the tracks after every iteration.

Kalman

A second algorithm [69] which is employed for the alignment of the CMS tracker is derived from the Kalman filter [70]. The algorithm works sequentially through a sample of tracks, updating the alignment parameters after each track. To avoid CPU limitations, only degrees of freedom which are sufficiently "close" in certain matrices are updated. By this, the inversion of large matrices is avoided. At the end of an alignment process, the Kalman algorithm gives a set of alignment parameters with their uncertainties.

Millepede II

The Millepede II algorithm [71] is a global linear least-squares algorithm. The dependence of the residuals on the track parameters is explicitly taken into account. All correlations among parameters are taken into account with this approach and a solution in one step is in

principle possible. Only very large misalignment or outlier rejection might make iterations necessary due to linearization. Separating the alignment (global) parameters p and the track (local) parameters q (see equation 6.2), the size of the matrix equation to be solved can be reduced to the number of alignment parameters. Fast methods to solve this still large matrix equation are provided. For not too large alignment problems, the whole matrix can be inverted, giving access to parameter uncertainties.

A full-scale alignment study of the complete CMS tracker with Millepede II can be found in [66].

Complementary Datasets

The χ^2-formula, given in equation 6.2, may not have a unique solution but several solutions which are numerically close to each other due statistical limitations or rounding. Furthermore other so-called *weak modes* may be present which do not change the overall χ^2 of a set of tracks. A simple example of a weak mode is a global shift or a global rotation of the whole tracker, which leaves the χ^2 unchanged. Other examples are elliptical deformations of the whole tracker which may be difficult to spot due to the rotational symmetry of the tracker. A key ingredient to improve the determination of alignment constants and the suppression of weak modes is the usage of datasets which interconnect different detector components with each other. High p_T tracks (e.g. muons from $W^{\pm}/Z^0$ decays) play an important role for alignment since the uncertainty from multiple scattering is greatly reduced at higher momenta. Muons are especially valuable in this respect as they do not have hadronic interactions and thus provide very clean tracks for alignment. Furthermore, muons from Z^0 decays have additional features which can be utilized, such as a common vertex and a well-defined invariant mass. Low momentum tracks on the other hand are important since some degrees of freedom in the alignment problem are poorly constrained, and high statistics are needed for an unambiguous solution. Large samples of low-momentum tracks will be available already early in the running from *minimum bias* events, which require only minimal trigger requirements[2] and are otherwise recorded irrespective of the specific content. Additional datasets are needed to constrain certain weak modes. Muons from cosmic rays are of prime importance as they interconnect detector parts which are not traversed by single tracks from collision events (e.g. upper and lower detector part). Another topology which can be important are *beam halo muons* which are generated in collisions of protons from the primary beams with residual gas atoms at large distances from the interaction point. Pions will be created in these collisions which subsequently decay and give rise to muons which often travel parallel or at very small angles with respect to the initial beam direction.

6.3 Validation of Alignment

6.3.1 Description of Observables

In all alignment approaches described above, the best solution to the alignment problem is found by minimizing the χ^2-function. As a first validation step, it has to be checked

[2] Typical trigger requirements would be a synchronization with a bunch from the LHC and *any* activity in the calorimeter.

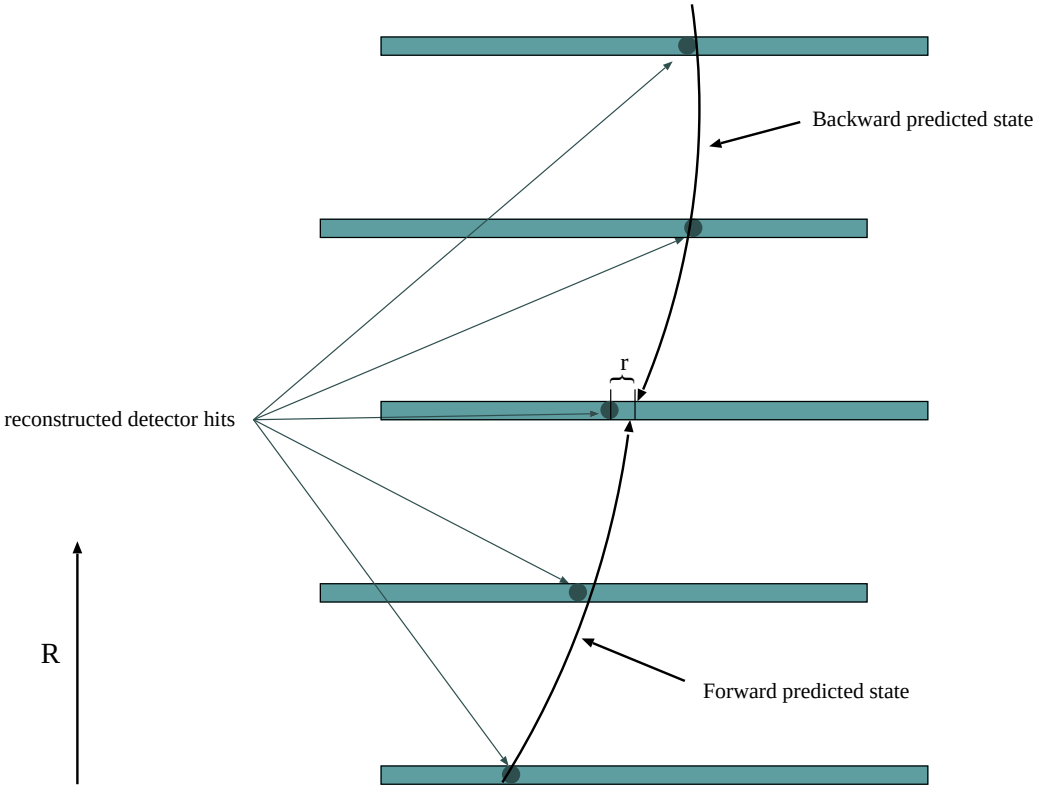

Figure 6.2: Illustration of the construction of a minimally biased residual for a given measurement.

whether the χ^2 has indeed improved with respect to the initial alignment state. For this, two different kinds of distributions can be checked: the χ^2- or the $\chi^2/ndof$-distributions which reflect the quality of the track fits after the alignment process. Furthermore, it is of interest to see if the quality of the fits depends on the position within the sensor. Hence, both χ^2 and $\chi^2/ndof$ are checked as a function of η and ϕ to see possible variations.

On the level of a single detector, a misalignment will manifest itself in the residual distribution. To get an independent estimate of the residual distribution, the detector under investigation is excluded from the track fit. Instead, the two track stubs pointing to the detector from both sides are combined. This is illustrated in figure 6.2. The combined predicted state is only minimally biased by the hit on the sensor since the track finding is not repeated but only the helix parameters are updated accordingly. If the alignment process is successful, the residual distribution should be centered around zero after the alignment. The width of the distribution depends on the quality of the alignment. In the ideal case, the width of the distribution should be dominated by the single hit resolution of the detector. In addition to the residuals, also the normalized residuals

$$\frac{r}{\sigma_r} = \frac{x_{\text{rec}} - x_{\text{pred}}}{\sqrt{\sigma^2_{x_{\text{rec}}} + \sigma^2_{x_{\text{pred}}}}} \tag{6.3}$$

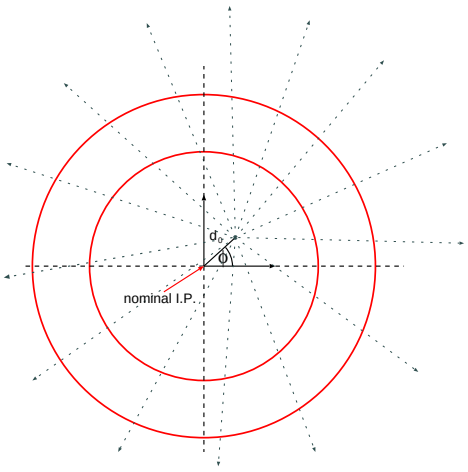

Figure 6.3: Illustration of vertex shift.

can be used to judge the quality of the alignment. Furthermore, it can be used to check the correctness of the error estimation. If both error contributions are estimated correctly and in the absence of misalignment, the distribution should be centered around zero with a width of one.

Apart from the residual based quantities mentioned above, other variables can be checked, which depend on track parameters but not on the individual measurements on the track. One example for this is the distribution of the transverse impact parameter d_0 of the track, where the distance is taken with respect to the origin at (0,0,0). When d_0 is plotted as function of the azimuthal angle ϕ, a sinusoidal shape can be expected for a movement of the nominal vertex. The amplitude of the sine-function corresponds to the radial displacement of the vertex, while the phase gives the rotational angle in the xy-plane. This is indicated in figure 6.3. Since the vertex position is also affected by other factors like the running conditions, this method cannot be used to determine the overall quality of an alignment. Differences between different alignment results, however, can hint at different correlated movements in the different solutions.

To detect a possible bias in the momentum measurement, the curvature of the tracks can be investigated. For certain deformations it can be expected that a difference can be seen between positive and negative tracks. On average, the momentum distributions should be equal for positive and negative tracks[3]. The asymmetry A_κ is defined as:

$$A_\kappa = \frac{N_{\kappa^+} - N_{\kappa^-}}{N_{\kappa^+} + N_{\kappa^-}}, \tag{6.4}$$

where $N_{\kappa^\pm}$ denotes the number of all positive (negative) tracks in the sample.

A first simple Monte Carlo study is performed to check the variables described above. Two preliminary alignment results [72] from the Millepede and the HIP algorithm are compared to the ideal detector geometry. These results are not achieved with the same conditions or track samples and thus it is not expected that the results will be identical. For the validation,

[3] A small asymmetry can be expected due to the non-zero charge of the initial state because of the identical charge of the two colliding protons.

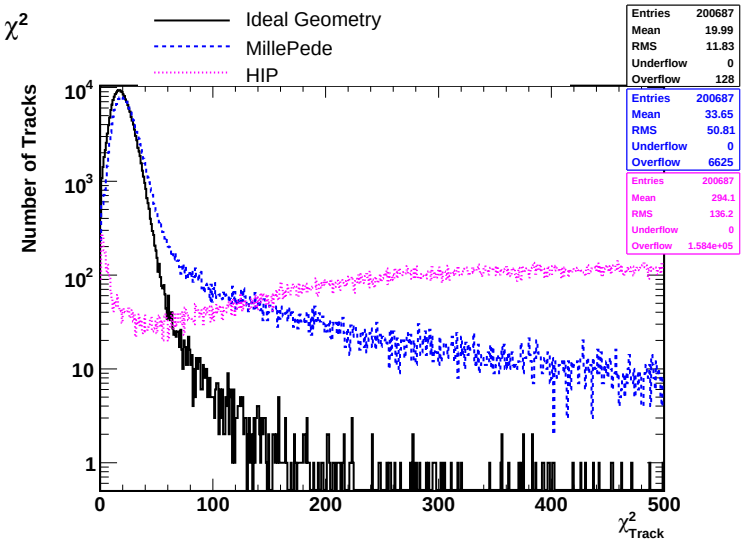

(a)

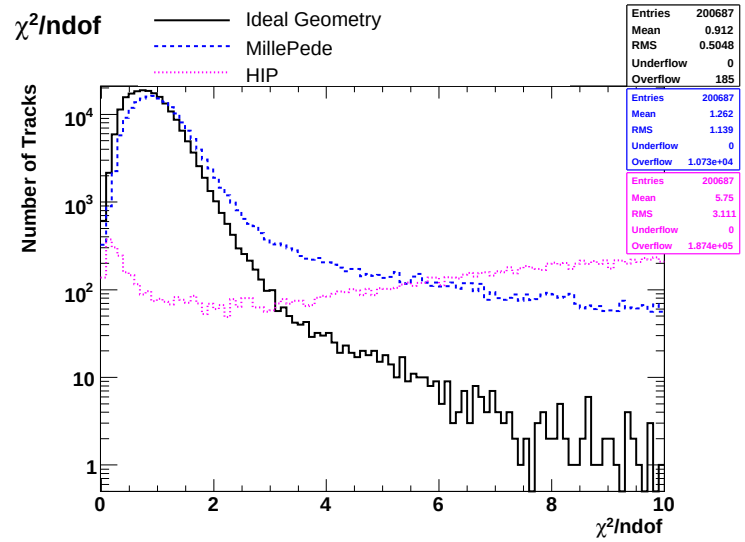

(b)

Figure 6.4: χ^2 (a) and $\chi^2/ndof$ (b) of track fits for the ideal geometry, compared to two alignments performed with the HIP and Millepede algorithm, respectively.

a sample of minimum bias events is used which is generated with the Pythia generator at a center-of-mass energy of 10 TeV, using a fast simulation (based on the FAMOS package [73]) of the CMS detector. Tracks are required to have a transverse momentum p_T of at least 3 GeV and at least 8 hits in the layers of the silicon tracker (pixel and strip). First, the χ^2- and $\chi^2/ndof$-distribution are compared. These are displayed in figure 6.4a and 6.4b. It can be seen that for tracks with a $\chi^2/ndof < 2$, the distribution for Millepede is already quite close to the one with the ideal geometry. The alignment result from the HIP algorithm on the other hand did not converge properly, hence a large mean value is observed. The

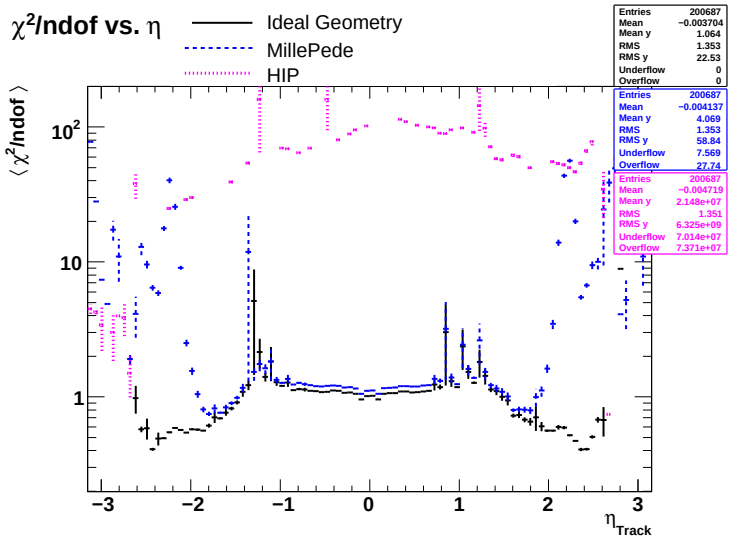

Figure 6.5: Mean $\chi^2/ndof$ of track fits as a function of η for the ideal geometry, compared to two alignments performed with the HIP and Millepede algorithm, respectively.

longer tail in the distribution of the Millepede alignment can be understood by looking at the mean $\chi^2/ndof$-value as a function of the track pseudorapidity η. This can be seen in figure 6.5 where the same two alignment results are again compared to the ideal geometry. χ^2 values very close to the ideal ones can be seen for the Millepede alignment result in the central and moderately forward region of the detector ($|\eta| \lesssim 2$), while large deviations can be seen at higher values of η. The large tail in figure 6.4 can be attributed to this region of the detector.

The other immediate check for the validation of the successful χ^2 minimization is to look at the absolute and normalized residuals of the tracks in various regions of the detector. The residual (r) is the same as defined in equation 6.1.

Two example residual distributions can be seen in figure 6.6, where the residual is displayed for the pixel tracker (6.6b) and the strip tracker (6.6a) including contributions of all respective subdetectors. It can be seen that all three histogramms are nicely centered around zero, however with large differences in the rms of the distributions. The ideal geometry peaks best around zero with very few outliers outside the displayed range. For the Millepede alignment result, the width of the distribution is larger but smaller than for the HIP object. It can be seen that the distribution for the HIP alignment shows much broader tails than the other distributions.

Next, the mean value of the transverse impact parameter, d_0, as a function of ϕ is compared for the different geometries. A sinusoidal shape can be seen in all distributions. The distributions are fitted with sine functions of the form $A\sin(\phi - \phi_0)$, where A denotes the amplitude and ϕ_0 the phase of the fit. It can be seen that the amplitude is different from zero for all three geometries. The amplitude is similar for the Millepede (256 μm) and the ideal geometry (323 μm). The HIP alignment shows a much larger amplitude. The phase differences between the ideal geometry and Millepede corresponds to a rotation of about 5°.

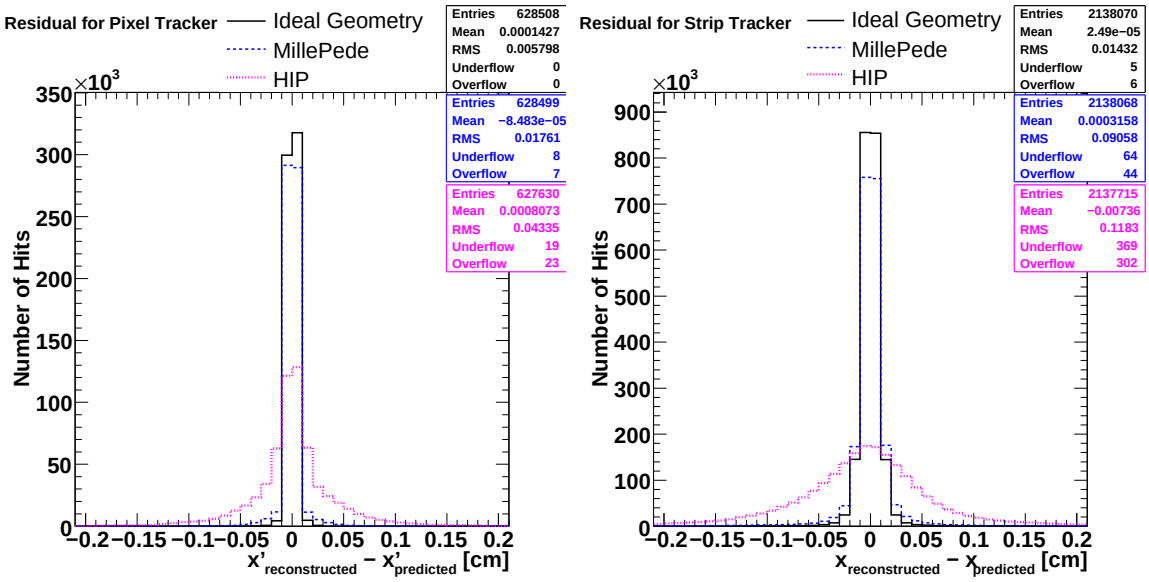

(a) (b)

Figure 6.6: Residual distribution of hits for the ideal detector geometry compared to two alignment results from the Millepede and HIP algorithms, respectively.

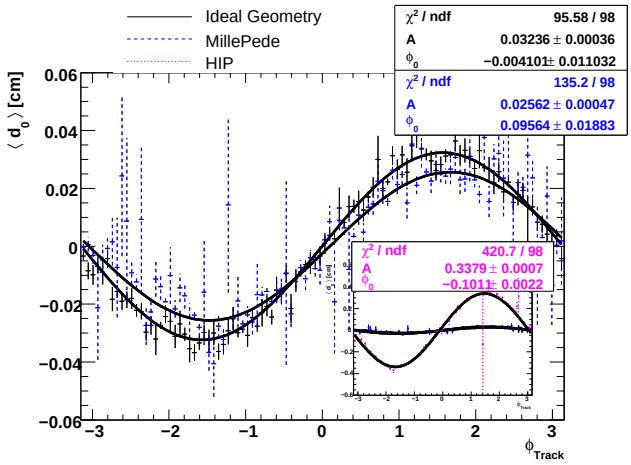

Figure 6.7: Mean value of the transverse impact parameter $\langle d_0 \rangle$ as function of the polar angle ϕ. Sinusoidal fit functions to the indivdual distributions are shown.

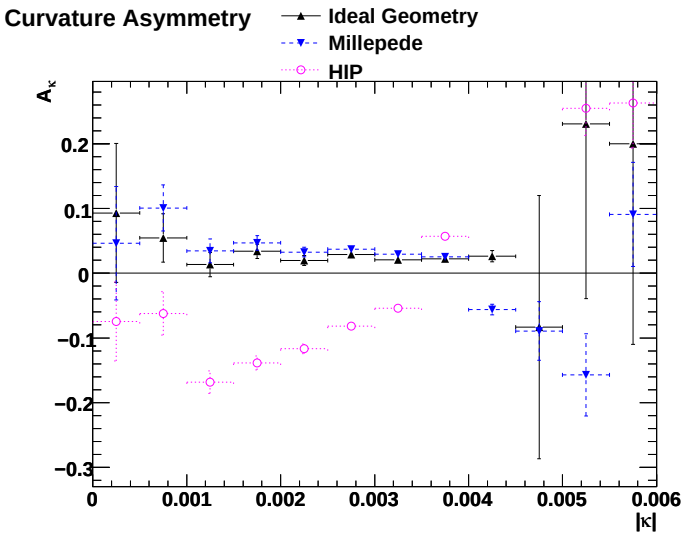

Figure 6.8: Curvature asymmetry for the ideal geometry, compared to two alignments performed with the HIP and Millepede algorithm, respectively.

In figure 6.8, an example distributon of the curvature asymmetry A_κ is shown. For the alignment results under study, a clear difference can be seen in the distribution. The asymmetry which is present for the ideal geometry is reproduced by the Millepede alignment result. The HIP object shows a very different asymmetry instead.

A systematic study with dedicated scenarios mimicking weak modes remains an open point of study.

Native Coordinates

A further improvement for the alignment validation which was already investigated in [74] comes from a different approach to certain residual distributions. The default configuration for the determination of residuals is simply the choice of local Cartesian coordinates with the x- and y-axis spanning the detector plane and the z-axis pointing upwards where upwards is defined as the direction of the strip implants in case of the strip modules and towards the readout electronics in case of the pixel modules. The orientation of the modules in the detector, however, changes due to spatial constraints. Due to this, modules are orientated differently in the detector (figure 6.9).

This occurs e.g. in the inner barrel where overlaps along the (CMS coordinate) z-direction between modules in the strings are achieved in this way. Due to this differences in the coordinate definition, correlated movements of modules in a string are not easily detectable when residuals are investigated in standard local coordinates. A shift of both modules in figure 6.9 will lead to a shift in the $+x$-direction for one module and $-x$-direction for the other modules. Hence the overall effect would likely be a broadening of the residual distribution. After the correction for the sign flip, a correlated effect can be expected. The same problem can occur for a sign flip of the y-axis. This is most relevant for stereo modules which are most sensitive to this coordinate. Furthermore, the choice of Cartesian

coordinates is not suitable for modules from the tracker inner disc and the tracker endcaps. Here, wedge-shaped modules are used with the strips pointing towards the beamline. These modules cover a certain region in $r\phi$. Therefore a more natural choice of measurement are polar or radial coordinates. Since the stereo modules are rotated by 100 mrad with respect to the global radial direction and the strips do not point to the beamline anymore, the transformation has to be done in the local frame.

This is illustrated in figure 6.10, where a wedge shaped module is sketched and the two choices of coordinate systems are indicated in the figure. Irrespective of the module geometry, the native coordinate in the precisely measured coordinate will be denoted as x' in the following. In figure 6.11, the effect of the transformation is illustrated. Both the residual and the normalized residual for all modules in the two TECs are shown in both coordinate definitions. It can be seen that there is a large difference for the non-normalized residual, which shows a very broad distribution in the standard case and a much more narrow and Gaussian distribution in the x'-case. For the normalized residuals it can be seen that for standard local Cartesian coordinates, the distribution is almost flat with sharp edges at two standard deviations. The x' distribution on the other hand follows a Gaussian as expected. These examples show that the native x'-coordinates lead to a much simpler statistical interpretation of residual measurements in the endcaps compared to the standard local Cartesian coordinates.

6.3.2 Alignment Validation on Data/Cosmic Run at Almost Four Tesla

An application of the alignment validation presented above will be shown in the following. For this, data taken during the so-called *Cosmic Run at Almost Four Tesla* (CRAFT) are used. The CRAFT was the first data taking with the fully assembled tracker and a magnetic field of 3.8 Tesla, which is decisive for the rejection of low momentum tracks which suffer from large multiple scattering. Two different tracker geometries are compared: the design geometry of the tracker and the best alignment object which was obtained using the data taken during the CRAFT. This object was obtained using the HIP alignment algorithm.

A preselected sample of 350,000 tracks reconstructed with the combinatorial track finder [75] is analyzed. Additionally, the following requirements have been imposed on the tracks:

- a momentum of more than 5 GeV,
- at least 10 hits have to constitute the track,
- at least two hits have to come from stereo modules, so that also the track coordinates along the strips are well defined.

A total of ∼125,000 (93,000) tracks are left after the selection and a refit with the HIP (design) geometry. The distribution of η, ϕ of the tracks is displayed in figure 6.12. It can be seen that the most tracks are reconstructed at central pseudorapidities. Furthermore it can be seen that tracks are almost exclusively reconstructed at negative ϕ values, which corresponds to downward propagating tracks.

In figure 6.13, the $\chi^2/ndof$ is displayed for the tracks from the sample described above. It can be seen that the HIP alignment provides a vast improvement of the χ^2 compared to the design geometry. For the aligned geometry, the distribution peaks at a value of around 1.2,

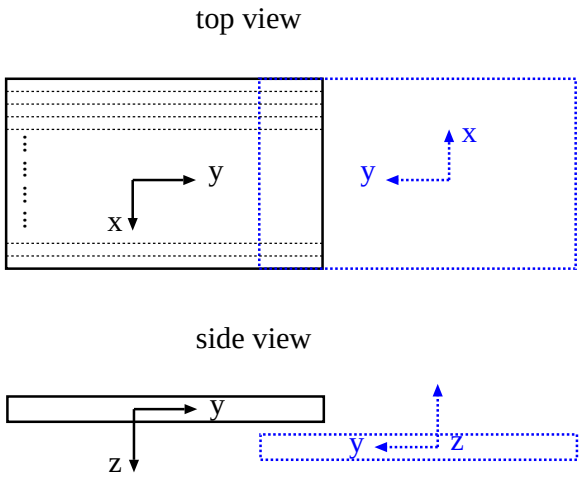

Figure 6.9: Illustration of possible differences in module orientation in the tracker.

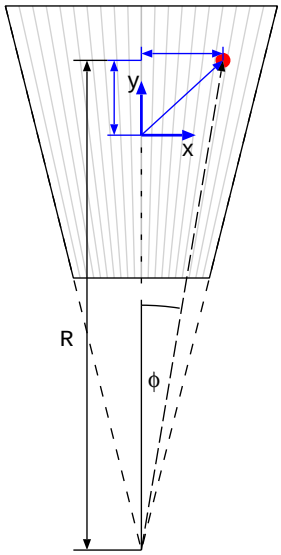

Figure 6.10: Illustration of the relation of local coordinate systems for wedge-shaped modules.

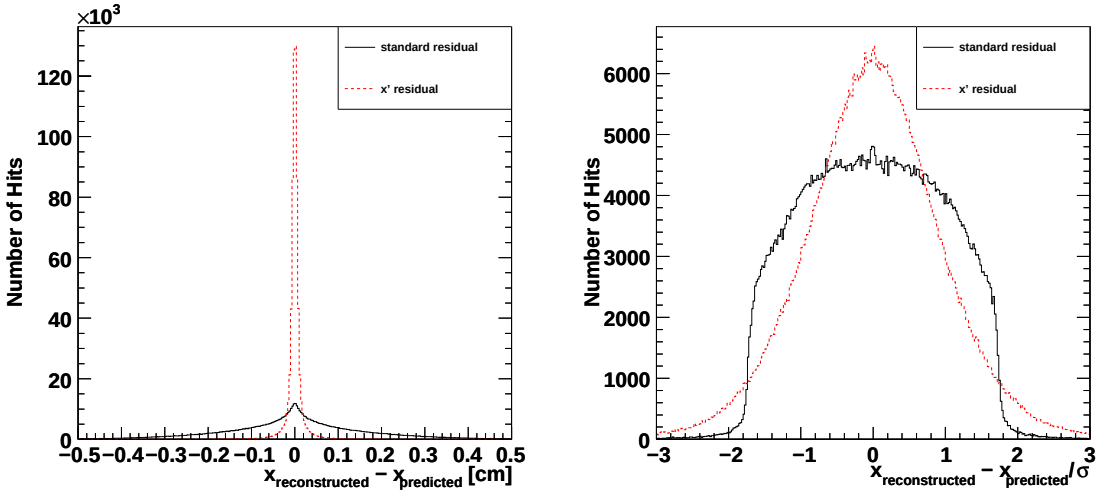

(a) (b)

Figure 6.11: Comparison of residuals (a) and normalized residuals (b) of hits in local Cartesian coordinates (solid) and native x' coordinates (dashed) for all modules in the tracker end caps.

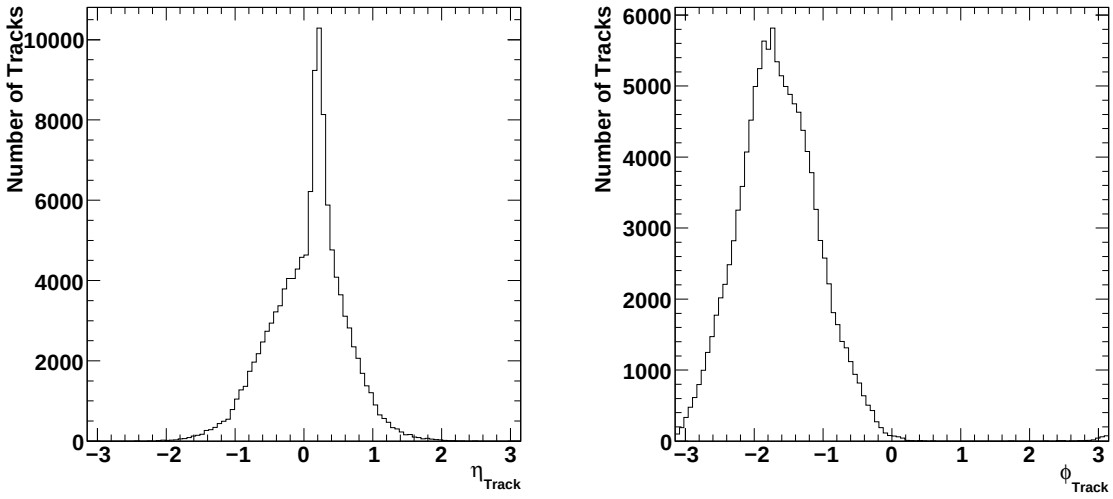

(a) (b)

Figure 6.12: η (a) and ϕ (b) of tracks reconstructed with the combinatorial track finder in the CRAFT.

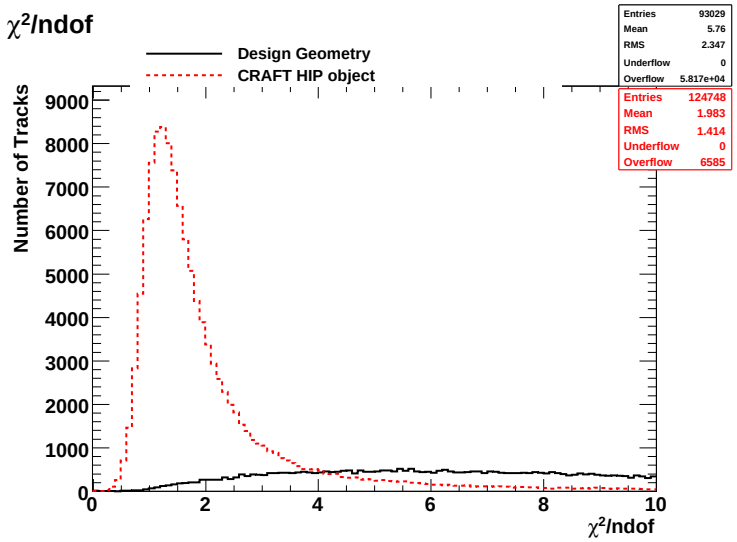

Figure 6.13: $\chi^2/ndof$ of track fits for the tracker design geometry compared to best HIP alignment of CRAFT data.

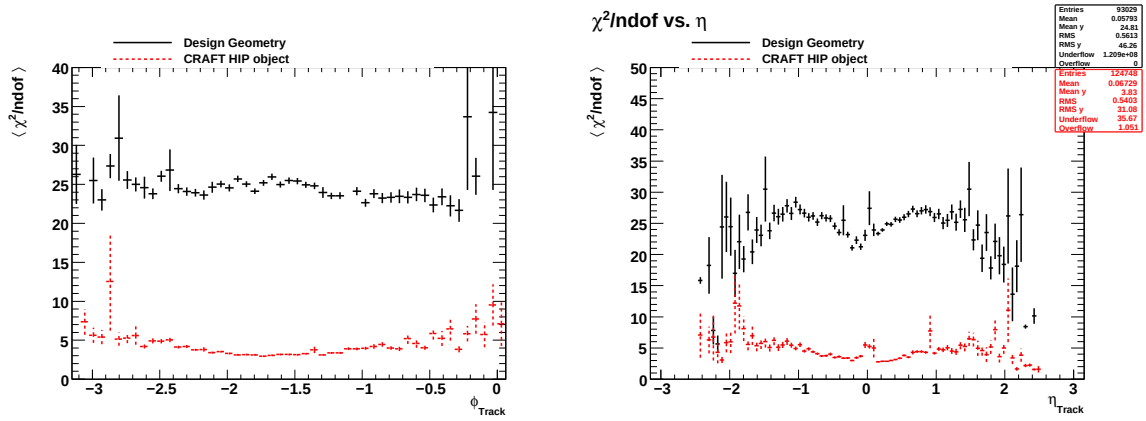

(a) (b)

Figure 6.14: Mean $\chi^2/ndof$ for track fits as a function of ϕ (a) and as a function of η (b) for the tracker design geometry compared to HIP alignment of CRAFT data.

which is already quite close to the expected values of 1. For the design geometry a peak value of around 5 can be estimated from the distribution. This large difference is also reflected in the differential distributions as function of ϕ and η in figure 6.14a and 6.14b. Only negative values of ϕ are considered due to the lack of statistics in the positive ϕ-region. It can be seen that also here a factor of about 5 between the two alignment results is observed. It should be noted that the absolute χ^2-value of around 5 for the HIP object and 25 for the design geometry comes from the averaging over a very large range of χ^2-values. This can be verified from the 2-dimensional distributions, which are displayed in figure 6.15 for the HIP alignment only. Here, the shape of the 1-dimensional distribution is reflected, with the bulk of the tracks at χ^2 values around 1.

The quality of the alignment can be further illustrated by looking at the residual distributions. In figure 6.16, the x' residuals are shown for the pixel and strip tracker, respectively. It should be noted that the statistics are generally very limited for the pixel tracker, due to the small geometric acceptance, which makes a precise alignment a more demanding task. Still it can be seen that the residuals are improved very much in the pixel tracker: An almost flat distribution is seen for the design geometry with many hits in the under- and overflow of the distribution, compared to a clear peak centered around zero and significantly reduced width after the alignment. In the strip tracker the difference is smaller, but again a clear improvement can be seen, although there are rather large tails. In figure 6.17, the corresponding normalized residuals are displayed. A clear improvement can be seen again, both in the pixel tracker and the strip tracker. The improvement for the individual subdetectors is shown in figure 6.20. Here, it can also be seen that despite the obvious improvement, some pathological problems seem to remain e.g. for the inner disc, where a large peak around zero with small width can be seen, whereas the rest of the distribution is much broader.

A further illustration of the effect of the alignment is displayed in figure 6.21, where the residual distributions of the different subdetectors are summarized for the pixel and strip tracker separately. The mean value and full width at half maximum of figures 6.18a and

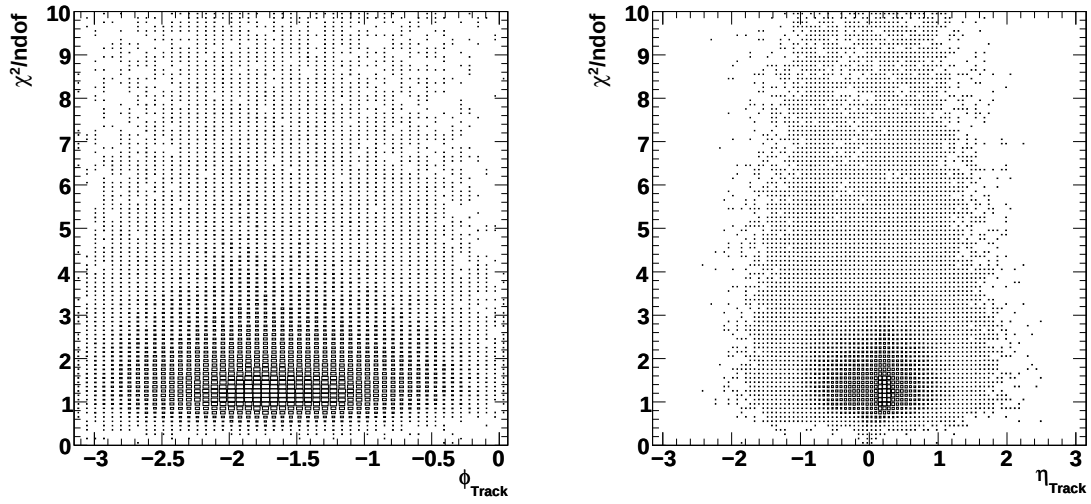

(a) (b)

Figure 6.15: $\chi^2/ndof$ as a function of ϕ (a) and as a function of η (b) for HIP alignment.

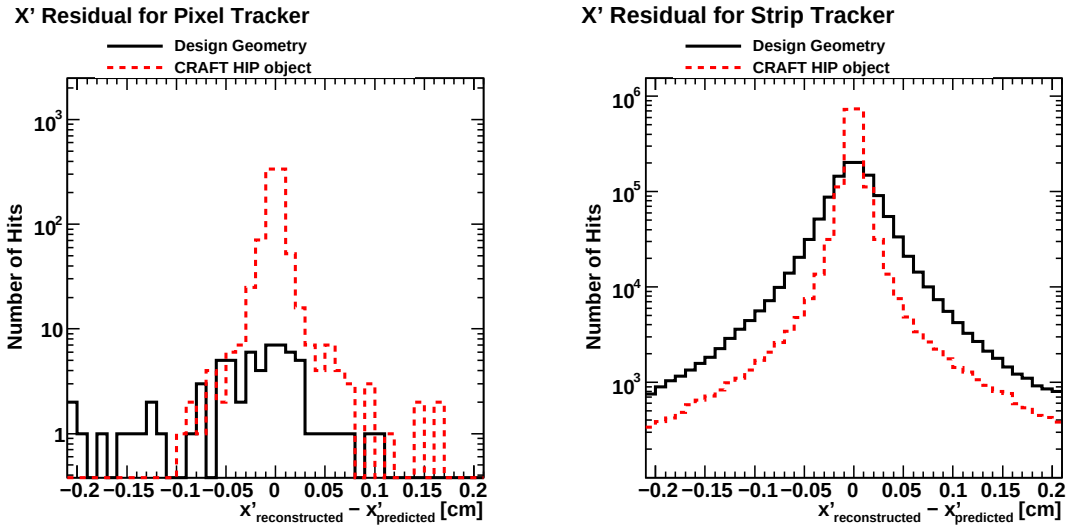

Figure 6.16: Residual distributions of hits in native coordinates for the pixel (left) and strip tracker (right) for the tracker design geometry compared to best CRAFT HIP alignment.

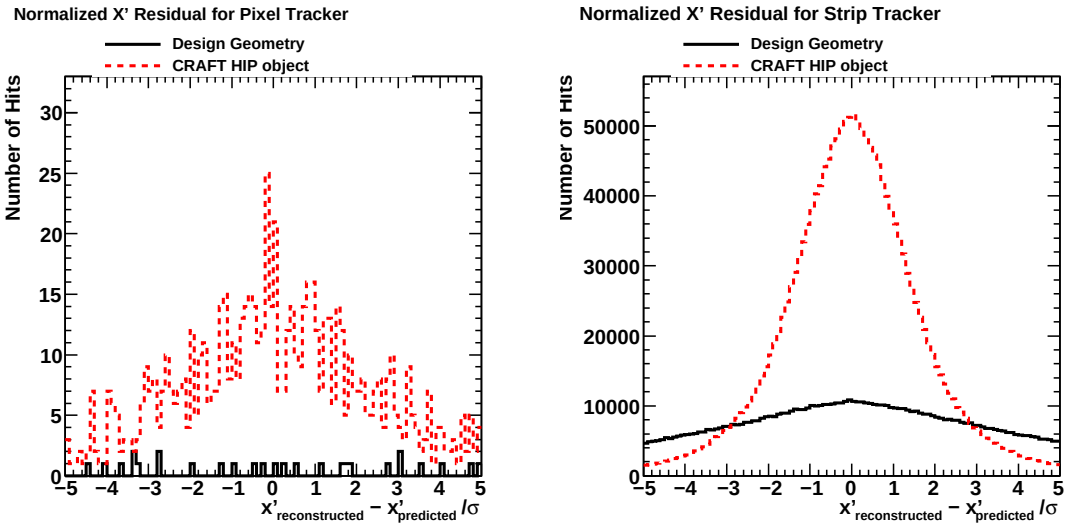

Figure 6.17: Normalized residuals for pixel (left) and strip tracker (right) for the tracker design geometry compared to best CRAFT HIP alignment.

6.19 are displayed for the pixel barrel and the two pixel endcaps in figure 6.21a and for the strip subdetectors in figure 6.21b. After the alignment, the mean values are better centered around zero and the width of the distributions is reduced in all cases. This behavior is also reflected within the subdetectors. This is illustrated by figure 6.22, where again the mean value and fwhm of the residual distributions are shown, this time for the two tracker endcaps. It can be seen that also for each individual disc, the mean value is improved with respect to the design. Hence it can be concluded that the given set of alignment parameters consistently improves the alignment of the detector also within the individual subdetectors.

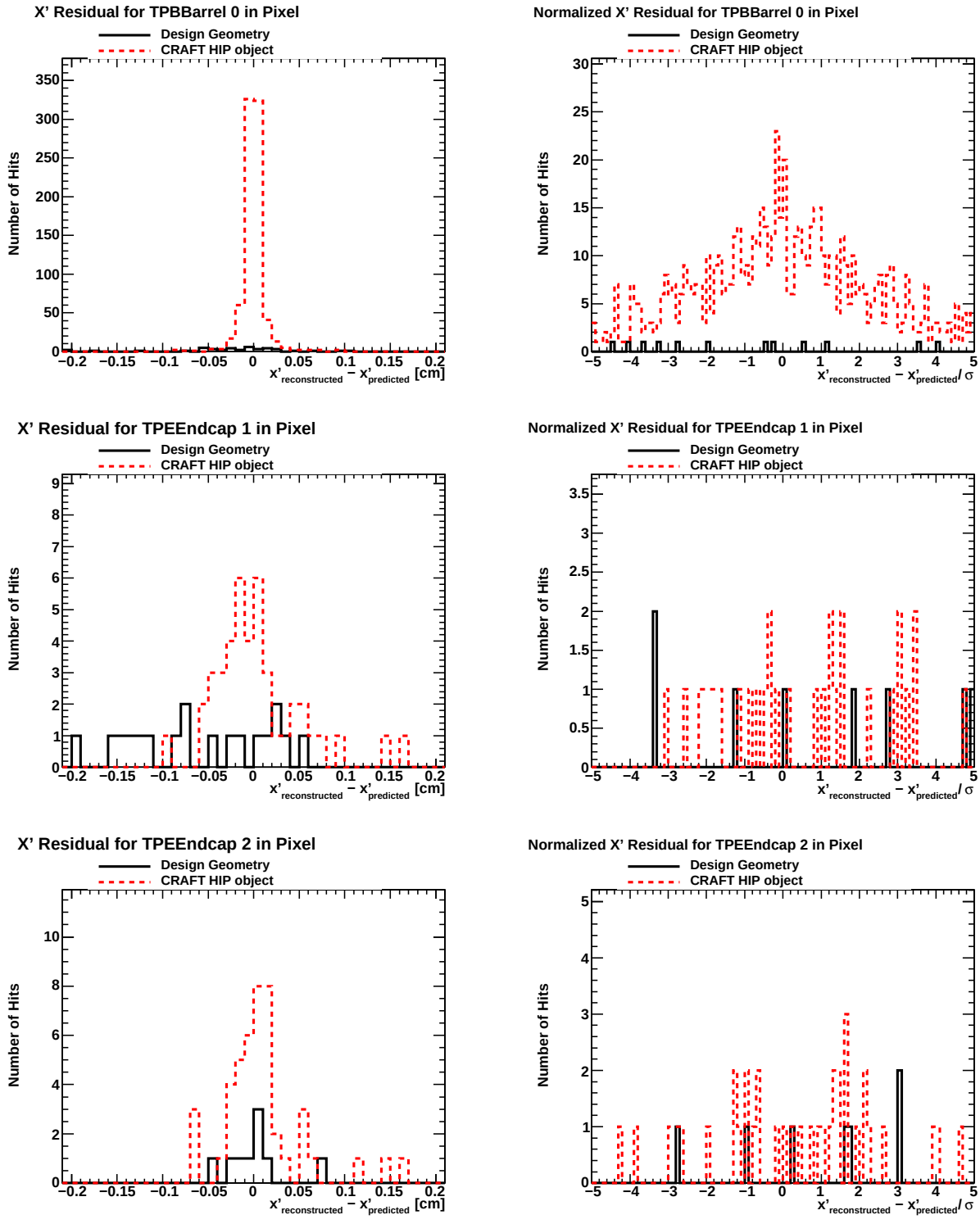

(a) (b)

Figure 6.18: Residuals (a) and normalized residuals (b) of hits for the pixel tracker subdetectors for the design geometry compared to HIP alignment of CRAFT data.

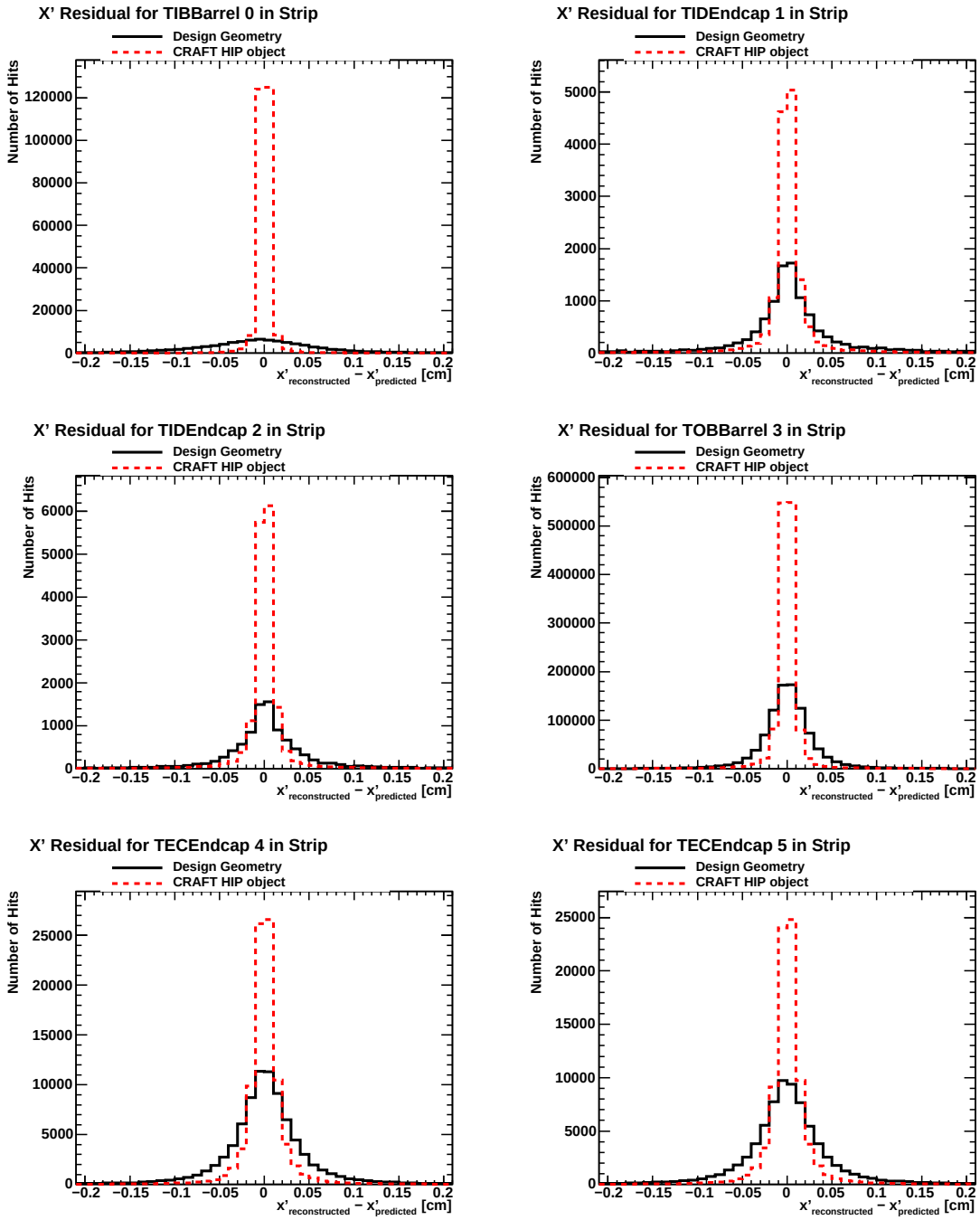

Figure 6.19: Residuals of hits for strip tracker subdetectors (TIB, TID1, TID2, TOB, TEC1, TEC2 from upper left to lower right) for the design geometry compared to HIP alignment of CRAFT data.

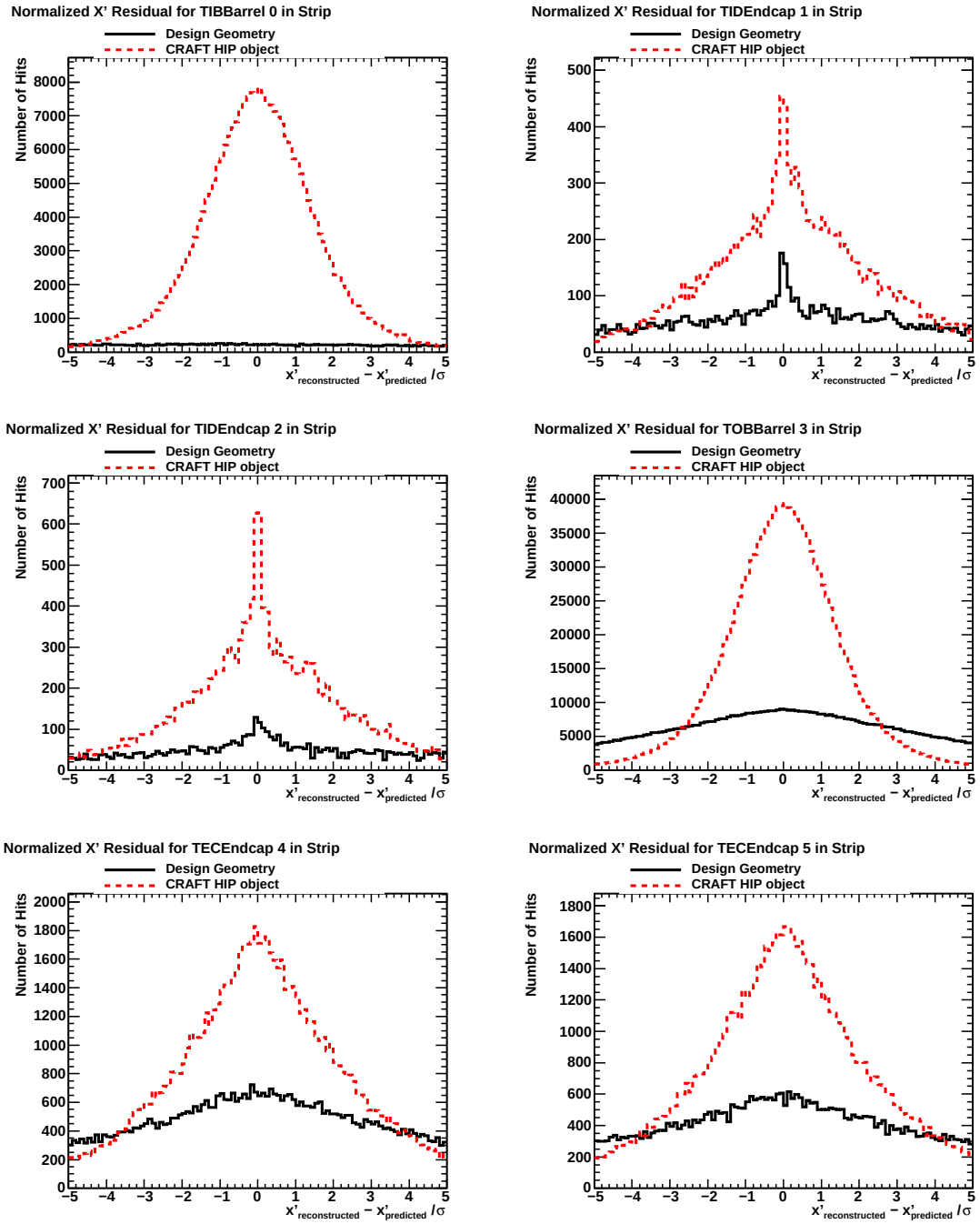

Figure 6.20: Normalized residuals for strip tracker subdetectors (TIB, TID1, TID2, TOB, TEC1, TEC2 from upper left to lower right) for the design geometry compared to HIP alignment of CRAFT data.

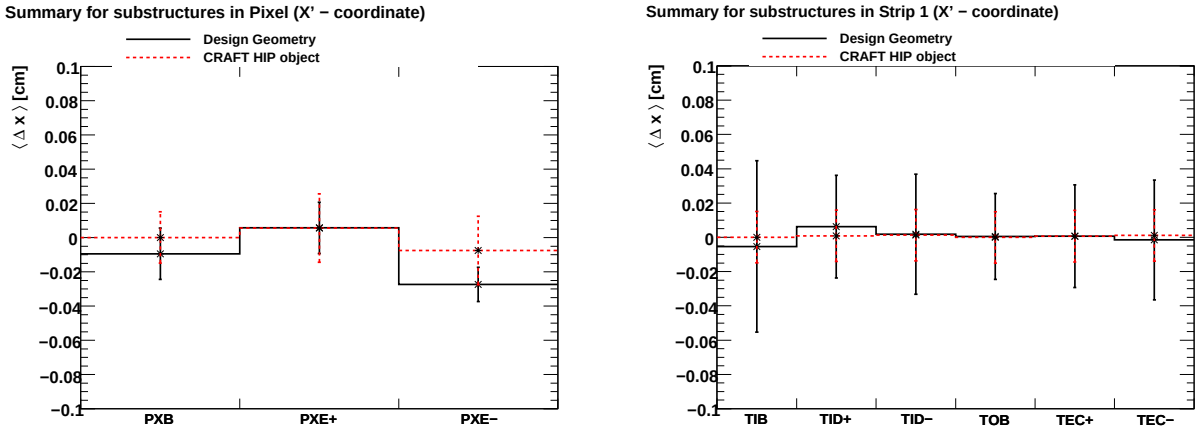

(a) (b)

Figure 6.21: Mean value and FWHM of the residuals in the pixel (a) and strip subdetectors (b) for the tracker design geometry compared to the HIP alignment of CRAFT data.

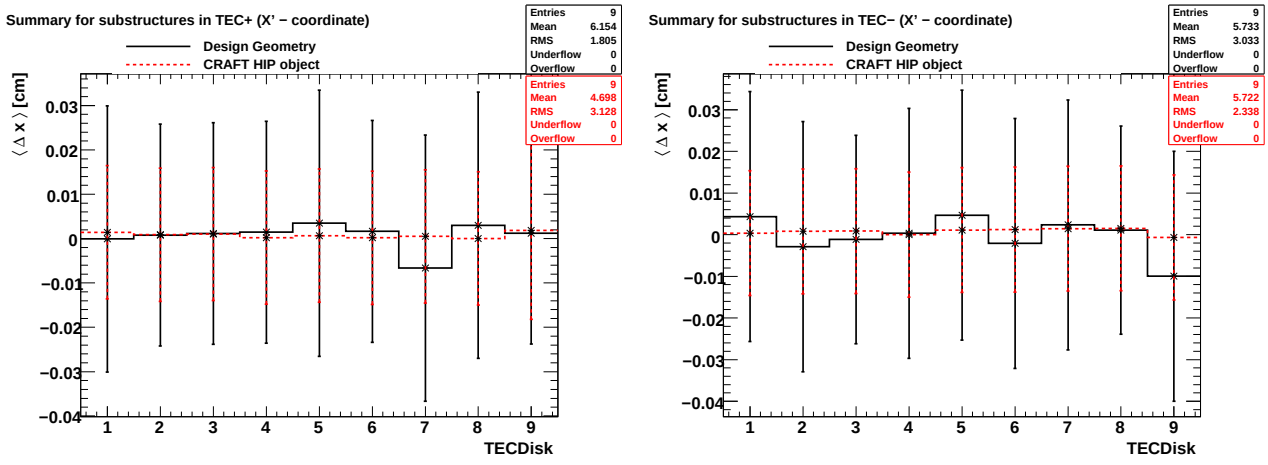

Figure 6.22: Mean value and fwhm for the indvidual discs within the two tracker endcaps for tracker design geometry compared to the HIP alignment of CRAFT data.

6.4 Summary of Alignment Validation

In this chapter, aspects of the alignment and validation of alignment results have been described. The CMS strategy for alignment employs different complementary sources of information such as assembly precision, a laser alignment system and track-based alignment. Possible strategies for the validation of alignment results have been discussed. A first step is to validate that the track χ^2 and the residuals in all subdetectors improve. As a first result, the validation of alignment constants from the HIP algorithm, prepared using data from the cosmic run at almost four tesla, has been presented. It can be clearly seen that after alignment, the track χ^2 decreases significantly and the residual distributions in all subdetectors are centered at zero and have smaller width. The peak value of the χ^2-distribution is close to one. Yet, the width of the residual distributions is much broader than the intrinsic detector resolution, at several hundred micron with tails to much larger values. While this result leave much room for improvement, it shows that the alignment of the detector can be improved with respect to the design geometry already with cosmics data alone. It can be expected that these results will be greatly improved when collision events become available. It should be noted that the investigation of residuals and the track χ^2 is only a statistical tool and does not give a handle on all possible detector movements. Especially weak modes remain an open point of investigation.

7 Summary and Outlook

This thesis dealt with the aspects of the calibration, alignment and long-term performance of the CMS silicon strip tracker. In the first part, measurements using an electron testbeam on irradiated and non-irradiated modules from the strip tracker were described. The setup was equipped with an external precision tracking, provided by three layers of silicon detectors (telescope). The datasets from the module under test and the telescope were merged offline to enable investigations using the external track reconstruction. The data were analyzed in several steps. After pedestal and noise determination and common-mode subtraction, different clustering algorithms were employed to reconstruct the impact position on the sensor. The signal-to-noise value of the strip tracker modules is typically 20 [55]. The spatial resolution was investigated for different clustering algorithms and as a function of different parameters. It has been found that the spatial resolution can be improved up to 35% with respect to the current default reconstruction scheme for inclination angles between 10° and 20° and above 40°. Furthermore it was shown that the spatial resolution is largely independent of irradiation. Charge sharing and crosstalk between individual strips were investigated using the precise prediction of the external reference. The crosstalk was found to be about 10% to the neighboring strips. Only a very slight increase of 1-2% was observed with increasing irradiation. It could be shown that the effect of the crosstalk can be corrected by using a finite impulse responds (FIR) method. For the future it remains to be investigated if the spatial resolution can be further improved by making use of the FIR correction to the signals. It is furthermore foreseen to use the testbeam data as input for simulations of radiation damage in silicon detectors.

After the testing of single modules, the performance of larger structures of the silicon strip tracker was investigated. The analyses were performed during the so-called tracker 'Slice Test' which took place from March to July 2007 at CERN. In this thesis, the performance of sectors of the tracker endcaps was investigated. The behavior of the operational parameters was monitored during various setup runs at different temperatures. The performance was found to be stable with time, and changes with other parameters were found to be in agreement with expectations. Various powering and readout schemes were tested and compared. Little sensititivity of the noise to these changes was observed; the noise was found to be stable within about 2%. The overall noise behavior was found to be well behaved and stable. Failures of components have been identified and monitored during the slice test. Known defects could be confirmed and some new defects could be identified. The amount of persistent defects is found to be about 0.7%.

The defects found during the course of the slice test can be used further to flag persistent defects early in the reconstruction process, in order to mitigate ineffiencies due to faulty detector components.

The alignment of the detector which will be of prime importance during all phases of its operation was discussed and a first validation of the vital tracker alignment during cosmic data taking with magnetic field was performed. A framework for the validation of alignment

results was set up, extending work from previous tests. Several possible observables were discussed and the working principle was shown. In the last part of the chapter, an application of the validation to data from the Cosmic Run at Almost Four Tesla (CRAFT) was shown as an example. The $\chi^2/ndof$ distribution for cosmic tracks shows a peak value which is already quite close to one, which is the expected value. Investigations of residual distributions showed that the alignment precision is improved with respect to the design geometry but still significantly worse than the intrinsic resolution of the modules. It can be expected that the alignment will improve significantly once collision data become available. The framework for the alignment validation is routinely used for the validation of alignment results and has already been extended to make best use of it.

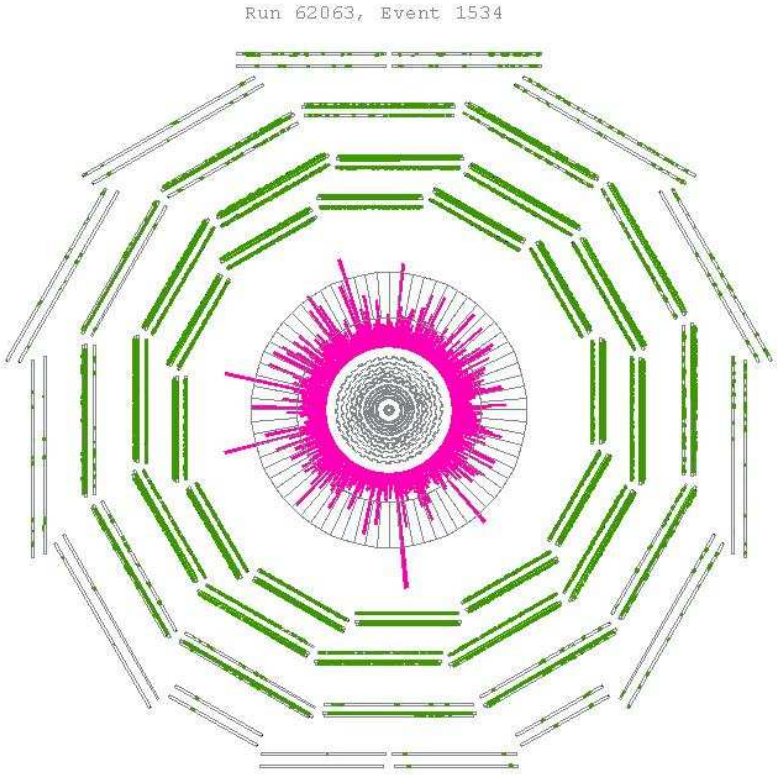

Figure 7.1: First beam through the detector: Image shows the debris, or "splash", of particles picked up in the detector's calorimeters and muon chambers after the beam was steered into the collimator (tungsten blocks) at Point 5.

Figure 7.1 shows a first beam-induced event in the CMS detector during the commissioning of the LHC ring in September 2008. The restart of the LHC is foreseen for the summer of 2009 and many interesting physics results can be expected in the course of its running.

A Constants

A set of silicon related constants is given in table A.1. Other fundamental constants used in this thesis are given in table A.2.

Table A.1: Silicon Related Constants

Constant	symbol	unit	value
Atomic weight		g/mol	28.0855(3)
Density (at RT)	ϱ_{Si}	g/cm^{-3}	2.3290
Mobility			
electrons	μ_e	cm^2/V	1450
holes	μ_h	cm^2/V	450
Crystal structure			fcc
Band gap	E_{gap}	eV	1.12
Intrinsic resistivity	ρ	kΩcm	235
Intrinsic charge carrier concentration		cm^{-3}	1.45×10^{10}

Table A.2: Fundamental constants

Constant	symbol	unit	value
Boltzmann's constant	k_B	J/K	$1.38658(12)\ \times10^{-23}$
		eV/K	$8.617358(73)\ \times10^{-5}$
Elementary charge	e	C	$1.602176487\times10^{-19}$
Planck's constant	h	Js	$6.62606896\ \times10^{-34}$
		eV s	4.13566733×10^{-15}
Speed of light (vacuum)	c	m/s	299 792 458
Electron rest mass	m_e	kg	$9.1093897(54)\times10^{-31}$
		MeV	0.510998910
Proton rest mass	m_p	kg	$1.6726231(10)\times10^{-27}$
		MeV	938.272013
Neutron rest mass	m_p	kg	$1.6726231(10)\times10^{-27}$
		MeV	938.272013
Atomic mass unit	u	kg	$1.6605402(10)\times10^{-27}$
		MeV	
Permitivity of the vacuum	ϵ_0	Fcm-1	$8.854187817\times10^{-14}$
Classical electron radius	r_e	m	$2.8179402894(58)\times10^{-15}$
Avogadro's number	N_A	mol^{-1}	$6.0221415(10)\times10^{23}$

B Details on Strip Tracker Modules

In the following, details of the dimensions of the different silicon modules in the strip tracker will be given.

Table B.1: Dimensions and muliplicities of sensors in the inner and outer barrel.

Type	Length [mm]	Height [mm]	Thickness [μm]	Pitch [μm]	Strips	Multiplicity
IB1	63.3	119.0	320	80	768	1536
IB2	63.3	119.0	320	120	512	1188
OB1	96.4	94.4	500	122	768	3360
OB2	96.4	94.4	500	183	512	7056

Table B.2: Dimensions and muliplicities of sensors in the inner disc and end caps.

Type	Length (short/long) [mm]	Height [mm]	Thickness [μm]	Pitch [μm]	Strips	Multiplicity
W1 TEC	64.6/87.9	87.2	320	81/112	768	288
W1 TID	63.6/93.8	112.9	320	80.5/119	768	288
W2	112.2/112.2	90.2	320	113/143	768	864
W3	64.9/83.0	112.7	320	123/158	512	880
W4	59.7/73.2	117.2	320	113/139	512	1008
W5a	98.9/112.3	84.0	500	126/142	768	1440
W5b	112.5/122.8	66.0	500	143/156	768	1440
W6a	86.1/97.4	99.0	500	163/185	512	1008
W6b	97.5/107.5	87.8	500	185/205	512	1008
W7a	74.0/82.9	109.8	500	140/156	512	1440
W7b	82.9/90.8	90.8	500	156/172	512	1440

C Finite Impulse Response Coefficients

The principle of the Finite Impulse Response (FIR) can in short be described as follows. Due to cross-talk and interstrip coupling, even a perfect signal (e.g. a test-pulse) injected into a single strip of the detector

$$y = \begin{pmatrix} 0 \\ 0 \\ 1 \\ 0 \\ 0 \end{pmatrix},$$

will be spread onto several strips, giving a non-zero charge on neighboring strips. The cross-talk can be parameterized as a matrix:

$$\begin{pmatrix} a & x_{r1} & x_{r2} & 0 & 0 \\ x_{l1} & a & x_{r1} & x_{r2} & 0 \\ x_{l2} & x_{l1} & a & x_{r1} & x_{r2} \\ 0 & x_{l2} & x_{l1} & a & x_{r1} \\ 0 & 0 & x_{l2} & x_{l1} & a \end{pmatrix}$$

where $x_{r/l\ i}$ is the cross-talk from the seed to i-th strip on the left and right, respectively and $a = 1 - x_{r1} - x_{l1} - x_{r2} - x_{l2}$. Multiplied to the vector y_δ it gives the responds, y_{resp}, of the detector:

$$\begin{pmatrix} a & x_{r1} & x_{r2} & 0 & 0 \\ x_{l1} & a & x_{r1} & x_{r2} & 0 \\ x_{l2} & x_{l1} & a & x_{r1} & x_{r2} \\ 0 & x_{l2} & x_{l1} & a & x_{r1} \\ 0 & 0 & x_{l2} & x_{l1} & a \end{pmatrix} \begin{pmatrix} 0 \\ 0 \\ 1 \\ 0 \\ 0 \end{pmatrix} = \begin{pmatrix} x_{r2} \\ x_{r1} \\ a \\ x_{l1} \\ x_{l2} \end{pmatrix} = y_{\text{resp}}$$

If the coefficients x_i are known, the effect of the cross-talk can be corrected with filter coefficients $F = (f_0, f_1, \ldots, f_n)^T$, where n is the order of the filter. The filter coefficients are the solution to the equation

$$AF = y_\delta$$

with

$$A = \begin{pmatrix} x_{l2} & x_{l1} & a & x_{r1} & x_{r2} & 0 & 0 & 0 & 0 \\ 0 & x_{l2} & x_{l1} & a & x_{r1} & x_{r2} & 0 & 0 & 0 \\ 0 & 0 & x_{l2} & x_{l1} & a & x_{r1} & x_{r2} & 0 & 0 \\ 0 & 0 & 0 & x_{l2} & x_{l1} & a & x_{r1} & x_{r2} & 0 \\ 0 & 0 & 0 & 0 & x_{l2} & x_{l1} & a & x_{r1} & x_{r2} \end{pmatrix}$$

This equation can be solved using a least square method (e.g. [76]):

$$F = (A^T A)^{-1} A^T y_\delta.$$

While this equation is exact, in practice it is limited by the number of neighboring channels which are taken into account. The signal of the i-th channel can approximately be restored by

$$w_{\mathrm{i}}^{\mathrm{FIR}} = \sum_{k=i-\frac{(n-1)}{2}}^{i+\frac{(n-1)}{2}} w_{\mathrm{k}}^{raw} f_k,$$

where k is the number of channels considered in the FIR correction, w_{k} is the pulse-height of the k-th channel and f_k is the k-coefficient. The effect of the smearing and the FIR correction are illustrated in figure C.1.

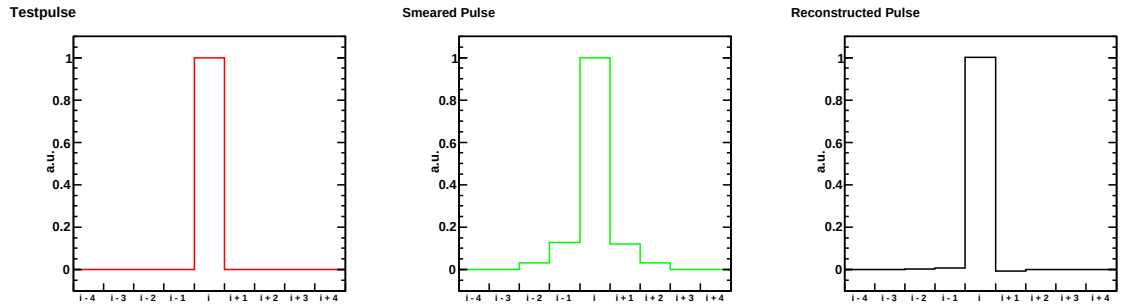

Figure C.1: Schematic representation of FIR crosstalk correction. The testpulse (left) is smeared by crosstalk and interstripcoupling (center). After the FIR correction (right), the original structure is restored within errors.

Bibliography

[1] S. L. Glashow. Partial Symmetries of Weak Interactions. *Nucl. Phys.*, 22:579–588, 1961. doi: 10.1016/0029-5582(61)90469-2.

[2] Steven Weinberg. A Model of Leptons. *Phys. Rev. Lett.*, 19:1264–1266, 1967. doi: 10.1103/PhysRevLett.19.1264.

[3] Abdus Salam. Weak and Electromagnetic Interactions. Originally printed in *Svartholm: Elementary Particle Theory, Proceedings Of The Nobel Symposium Held 1968 At Lerum, Sweden*, Stockholm 1968, 367-377.

[4] Gerard 't Hooft and M. J. G. Veltman. Regularization and Renormalization of Gauge Fields. *Nucl. Phys.*, B44:189–213, 1972. doi: 10.1016/0550-3213(72)90279-9.

[5] D. J. Gross and Frank Wilczek. Ultraviolet Behavior of non-abelian Gauge Theories. *Phys. Rev. Lett.*, 30:1343–1346, 1973. doi: 10.1103/PhysRevLett.30.1343.

[6] H. David Politzer. Reliable Perturbative Results for Strong Interactions? *Phys. Rev. Lett.*, 30:1346–1349, 1973. doi: 10.1103/PhysRevLett.30.1346.

[7] H. Fritzsch, Murray Gell-Mann, and H. Leutwyler. Advantages of the Color Octet Gluon Picture. *Phys. Lett.*, B47:365–368, 1973. doi: 10.1016/0370-2693(73)90625-4.

[8] J. Alcaraz et al. Precision Electroweak Measurements and Constraints on the Standard Model. 2007.

[9] R. Barate et al. Search for the standard model Higgs boson at LEP. *Phys. Lett.*, B565: 61–75, 2003. doi: 10.1016/S0370-2693(03)00614-2.

[10] Gregor Bernardi et al. Combined CDF and Dzero Upper Limits on Standard Model Higgs Boson Production at High Mass (155-200 GeV/c2) with 3 fb-1 of data. 2008.

[11] Peter W. Higgs. Broken Symmetries and the Masses of Gauge Bosons. *Phys. Rev. Lett.*, 13:508–509, 1964. doi: 10.1103/PhysRevLett.13.508.

[12] F. Englert and R. Brout. Broken symmetry and the mass of gauge vector mesons. *Phys. Rev. Lett.*, 13(9):321–323, Aug 1964. doi: 10.1103/PhysRevLett.13.321.

[13] G. S. Guralnik, C. R. Hagen, and T. W. B. Kibble. Global conservation laws and massless particles. *Phys. Rev. Lett.*, 13(20):585–587, Nov 1964. doi: 10.1103/PhysRevLett.13.585.

[14] D. N. Spergel et al. First Year Wilkinson Microwave Anisotropy Probe (WMAP) Observations: Determination of Cosmological Parameters. *Astrophys. J. Suppl.*, 148: 175, 2003. doi: 10.1086/377226.

[15] G. Hinshaw et al. Five-Year Wilkinson Microwave Anisotropy Probe (WMAP) Observations:Data Processing, Sky Maps, & Basic Results. 2008.

[16] Robert A. Knop et al. New Constraints on Ω_M, Ω_Λ, and w from an Independent Set of Eleven High-Redshift Supernovae Observed with HST. *Astrophys. J.*, 598:102, 2003. doi: 10.1086/378560.

[17] J. Wess and B. Zumino. Supergauge Transformations in Four-Dimensions. *Nucl. Phys.*, B70:39–50, 1974. doi: 10.1016/0550-3213(74)90355-1.

[18] Lisa Randall and Raman Sundrum. Large mass hierarchy from a small extra dimension. *Phys. Rev. Lett.*, 83(17):3370–3373, Oct 1999. doi: 10.1103/PhysRevLett.83.3370.

[19] Steven Weinberg. Implications of Dynamical Symmetry Breaking: An Addendum. *Phys. Rev.*, D19:1277–1280, 1979. doi: 10.1103/PhysRevD.19.1277.

[20] Edward Farhi and Leonard Susskind. Technicolor. *Phys. Rept.*, 74:277, 1981. doi: 10.1016/0370-1573(81)90173-3.

[21] C. Amsler et al. Review of particle physics. *Phys. Lett.*, B667:1, 2008. doi: 10.1016/j.physletb.2008.07.018.

[22] Savas Dimopoulos and Leonard Susskind. Mass Without Scalars. *Nucl. Phys.*, B155: 237–252, 1979. doi: 10.1016/0550-3213(79)90364-X.

[23] Estia Eichten and Kenneth D. Lane. Dynamical Breaking of Weak Interaction Symmetries. *Phys. Lett.*, B90:125–130, 1980. doi: 10.1016/0370-2693(80)90065-9.

[24] Thomas Appelquist and Robert Shrock. Neutrino masses in theories with dynamical electroweak symmetry breaking. *Phys. Lett.*, B548:204–214, 2002. doi: 10.1016/S0370-2693(02)02854-X.

[25] G. L. Bayatian et al. CMS physics: Technical design report. CERN-LHCC-2006-001.

[26] L. P. Bouckaert, R. Smoluchowski, and E. Wigner. Theory of brillouin zones and symmetry properties of wave functions in crystals. *Phys. Rev.*, 50(1):58–67, Jul 1936. doi: 10.1103/PhysRev.50.58.

[27] Chelikowsky, J.R. and Cohen, M.L . Electronic structure of silicon. *Phys.Rev. B*, 10: 5095–5107, 1974.

[28] L. Landau. On the energy loss of fast particles by ionization. *J. Phys. (USSR)*, 8: 201–205, 1944.

[29] Markus Friedl. *The CMS Silicon Strip Tracker and its Electronic Readout*. PhD thesis, Vienna University of Technology, 2001. http://cern.ch/friedl.

[30] Michael Moll. Radiation damage in silicon particle detectors: Microscopic defects and macroscopic properties. DESY-THESIS-1999-040.

[31] Lyndon Evans (ed.) and Philip Bryant (ed.). LHC Machine. *JINST*, 3:S08001, 2008. doi: 10.1088/1748-0221/3/08/S08001.

[32] M. Della Negra et al. CMS: The Compact Muon Solenoid: Letter of intent for a general purpose detector at the LHC. CERN-LHCC-92-03.

[33] Dragoslav Lazic. The CMS Magnet Test and Cosmic Challenge (MTCC): Operational experience and lessons learnt. *Nucl. Phys. Proc. Suppl.*, 172:3–7, 2007. doi: 10.1016/j.nuclphysbps.2007.07.021.

[34] W. Adam et al. The CMS tracker operation and performance at the Magnet Test and Cosmic Challenge. *JINST*, 3:P07006, 2008. doi: 10.1088/1748-0221/3/07/P07006.

[35] CMS, tracker technical design report. . CERN-LHCC-98-06.

[36] Addendum to the CMS tracker TDR. . CERN-LHCC-2000-016.

[37] R. Adolphi et al. The CMS experiment at the CERN LHC. *JINST*, 3:S08004, 2008. doi: 10.1088/1748-0221/3/08/S08004.

[38] A. Dorokhov et al. Tests of silicon sensors for the CMS pixel detector. *Nucl. Instrum. Meth.*, A530:71–76, 2004. doi: 10.1016/j.nima.2004.05.050.

[39] S. Braibant et al. Investigation of design parameters for radiation hard silicon microstrip detectors. *Nucl. Instrum. Meth.*, A485:343–361, 2002. doi: 10.1016/S0168-9002(01)02120-9.

[40] L. L. Jones et al. The APV25 deep submicron readout chip for CMS detectors. Prepared for 5th Workshop on Electronics for the LHC Experiments (LEB 99), Snowmass, Colorado, 20-24 Sep 1999.

[41] Vasey F. Bauer, Th. A model for the cms tracker analog optical link. *CERN-CMS-NOTE-2000-056*, 2000.

[42] Bruno Wittmer. *The Laser Alignment System for the CMS Silicon Microstrip Tracker*. PhD thesis, RWTH Aachen, 2002.

[43] G. Acquistapace et al. CMS, the magnet project: Technical design report. CERN-LHCC-97-10.

[44] *The CMS muon project: Technical Design Report*. Technical Design Report CMS. CERN, Geneva, 1997. CERN-LHCC-97-032.

[45] P. Sphicas (ed.). CMS: The TriDAS project. Technical design report, Vol. 2: Data acquisition and high-level trigger. CERN-LHCC-2002-026.

[46] Additional information about the Desy testbeams can be found at. http://adweb.desy.de/~testbeam/.

[47] Alexander Furgeri. Quality assurance and irradiation studies on CMS silicon strip sensors. IEKP-KA-2005-1.

[48] E. Focardi A. Macciolo L. Borello, A. Messineo. Sensor design for the CMS Silicon Strip Tracker. CERN-CMS-NOTE-2003-020.

[49] M. Axer et al. A Test Setup for Quality Assurance of Frontend Hybrids. CERN-CMS-NOTE-2001-046.

[50] Devis Contarato. Silicon detectors for particle tracking at future high- energy physics experiments. DESY-THESIS-2005-044.

[51] R. Turchetta. Spatial resolution of silicon microstrip detectors. *Nucl. Instrum. Meth.*, A335:44–58, 1993. doi: 10.1016/0168-9002(93)90255-G.

[52] T. Kawasaki et al. Measurement of the spatial resolution of wide-pitch silicon strip detectors with large incident angle. *IEEE Trans. Nucl. Sci.*, 44:708–712, 1997. doi: 10.1109/23.603738.

[53] E. Belau et al. The Charge Collection in Silicon Strip Detectors. *Nucl. Instr. Meth.*, 214:253, 1983. doi: 10.1016/0167-5087(83)90591-4.

[54] Christoph Bloch. Studies for the commissioning of the CERN CMS silicon strip tracker. CERN-THESIS-2008-004.

[55] Markus Stoye. Calibration and alignment of the CMS silicon tracking detector. DESY-THESIS-2007-026.

[56] Lindström, G. and others. 2nd RD48 Status Report: R&D on silicon for future experiments. Technical Report CERN-LHCC-98-039, CERN, Geneva, Oct 1998.

[57] W. de Boer et al. The performance of irradiated CMS silicon mirco-strip detector modules. CERN-CMS-NOTE-2006-049.

[58] W. Adam et al. Silicon Strip Tracker Detector Performance with Cosmic Ray Data at the Tracker Integration Facility. (in preparation). CERN-CMS-NOTE.

[59] W. Adam et al. Track Reconstruction with Cosmic Ray Data at the Tracker Integration Facility. (in preparation). CERN-CMS-NOTE.

[60] W. Adam et al. CMS Tracker Alignment at the Integration Facility. (in preparation). CERN-CMS-NOTE.

[61] Robert Bainbridge et al. Commissioning and calibration of the CMS Silicon Strip Tracker. Prepared for 12th Workshop on Electronics for LHC and Future Experiments (LECC 2006), Valencia, Spain, 25-29 Sep 2006.

[62] Stefanos Dris, Karl Gill, Jan Troska, Francois Vasey. Predicting the Gain Spread of the CMS Tracker Analog Readout Optical Links. *CERN-CMS-NOTE*, 2006.

[63] R. Brauer et al. Design and test beam performance of substructures of the CMS tracker end caps. CERN-CMS-NOTE-2005-025.

[64] Gordon Kaußen. *Silicon strip detector qualification for the CMS experiment.* PhD thesis, RWTH Aachen, 2008.

[65] Richard Bremer. *Integration of the end cap TEC+ of the CMS silicon strip tracker.* PhD thesis, RWTH Aachen, 2008.

[66] G. Flucke, P. Schleper, G. Steinbruck, and M. Stoye. A study of full scale CMS tracker alignment using high momentum muons and cosmics. CERN-CMS-NOTE-2008-008.

[67] S. Blusk (ed.) et al. Proceedings of the first LHC Detector Alignment Workshop, CERN, Geneva, Switzerland, 4-6 September 2006. 1st LHC Detection Alignment Workshop 4-6 Sep 2006, Geneva, Switzerland.

[68] V. Karimaki, A. Heikkinen, T. Lampen, and T. Linden. Sensor alignment by tracks. 2003.

[69] E. Widl, R. Fruhwirth, and W. Adam. A Kalman filter for track-based alignment. CERN-CMS-NOTE-2006-022.

[70] R. E. Kalman. A new approach to linear filtering and prediction problems. *Journal of Basic Engineering*, 82:35–45, 1960.

[71] V. Blobel. Software alignment for tracking detectors. *Nucl. Instrum. Meth.*, A566:5–13, 2006. doi: 10.1016/j.nima.2006.05.157.

[72] Lae, Chung Khim and Miglioranzi, Silvia . private communication.

[73] Stephan Wynhoff. FAMOS: A dynamically configurable system for fast simulation and reconstruction for CMS. 2003.

[74] Johannes Hauk. Validierung von Alignmentkonstanten des CMS-Spurdetektors mit kosmischen Myonen. 2008. Diploma Thesis.

[75] Adam, W and others. Track reconstruction in the CMS tracker. *CERN-CMS-NOTE*, 2006.

[76] Volker Blobel and Erich Lohrmann. *Statistische und numerische Methoden der Datenanalyse*. Teubner, 1998.

[77] Jula Draeger and Gero Flucke. private communication.

[78] J. L. Agram et al. The silicon sensors for the Compact Muon Solenoid tracker: Design and qualification procedure. *Nucl. Instrum. Meth.*, A517:77–93, 2004. doi: 10.1016/j.nima.2003.08.175.

[79] O. Blunck and S. Leisegang. Zum energieverlust schneller elektronen in dünnen schichten. *Zeitschrift für Physik A Hadrons and Nuclei*, 128(4):500–505, Aug 1950. doi: 10.1007/BF01330032. URL `http://dx.doi.org/10.1007/BF01330032`.

[80] P. Schleper, G. Steinbruck, and M. Stoye. Software alignment of the CMS tracker using MILLEPEDE II. CERN-CMS-NOTE-2006-011.

[81] B. Wittmer. Alignment with infrared laser beams and silicon microstrip detectors. Prepared for International Europhysics Conference on High- Energy Physics (HEP 2001), Budapest, Hungary, 12-18 Jul 2001.

[82] E. Butz et al. Performance of irradiated Modules of the CMS Tracker. *(in preparation)*. CMS-NOTE.

Acknowledgements

An dieser Stelle wird es Zeit, Danke zu sagen:

Prof. Dr. Schleper für die Möglichkeit diese Arbeit in dieser Gruppe anfertigen zu können, sowie für seine stete Begeisterung für die Physik im Allgemeinen und die Teilchenphysik im Besonderen.
Prof. Dr. Mnich danke ich für die Erstellung des zweiten Gutachtens.
Prof. Dr. Klanner für unschätzbar viel Wissen über Silizium-Detektoren und die trotz seiner knappen Zeit stete Bereitschaft auch die trivialsten Sachverhalte zu erläutern.
Dr. Georg Steinbrück für viel Geduld in der täglichen Arbeit und viel Unterstützung bei der Erstellung dieser Arbeit.
Dr. Gero Flucke für viele nützliche Informationen zu C++ im Allgemeinen und zu CMSSW und ROOT im Besonderen, für die Wohnung in Genf, sowie manch harsche Fahrrad-Tour und Bergwanderung.
Dr. Katja Klein für die sehr gute Betreuung und Anleitung während der Arbeit am CERN sowie viel Detailwissen rund um den Tracker und seine End-Kappen.
Dr. Doris Eckstein für viele aufmunternde Worte und große Hilfe beim Auffinden subtiler Probleme.
Dr. Marc-Henning Zöller für die gute Zusammenarbeit, viele nützliche Tipps zur Analyse der Tracker Daten sowie viel Spaß am CERN.
Meinen gesammelten Büro-Kollegen für die nette Gemeinschaft und stets gute Atmosphäre.
Den Aachener und Wiener Kollegen am CERN für die nette Zusammenarbeit.
Uwe Pein für viel Hilfe bei Reisekosten und anderen Katastrophen.
Meinen Freunden, Bekannten und Kommilitonen, mit denen ich über die letzten Jahre viel Spaß haben durfte. Besonders:
Dipl.-Phys. Daniel Bick, für mehrere sehr schöne Radtouren durch verschiedene Teile der Republik, lecker Tee, sowie für die stete Ermahnung, dass es noch τ-send andere interessante Themen in der Physik gibt.
Dipl.-Phys. Björn Opitz für immer wieder interessanten Lesestoff, viel Kaffee und die Ermahnung, dass es noch tausend interessante Themen außerhalb der Physik gibt.
Gero, Roger, Georg, Daniel, Björn sowie meinem Vater für das Korrekturlesen.
Meinen Eltern, für die Unterstützung über all die Jahre.

Irina, für die stete Unterstützung und Ermunterung, für das Auf-den-Boden-Zurückholen bei Abhebgefahr, und für die vielen schönen Stunden die wir trotz der häufig großen Entfernung hatten und von denen hoffentlich noch viele auf uns warten.

Danke!

List of Figures

List of Tables